UNIVERSITÀ DEGLI STUDI DI TRIESTE

XXX CICLO DEL DOTTORATO DI RICERCA IN

NANOTECNOLOGIE

FUNCTIONAL HETEROSTRUCTURES BASED ON COLLOIDAL NANOCRYSTALS

Settore scientifico-disciplinare: **ING-IND/22**

DOTTORANDO
EMANUELE ALBERTO SLEJKO

COORDINATORE
PROF. LUCIA PASQUATO

SUPERVISORE DI TESI
PROF. VANNI LUGHI

ANNO ACCADEMICO 2016/2017

to the readers, may they be resilient

to Liliana

Preface

Pushing human-knowledge behind its limits is one of the most rewarding jobs we can perform. Technology is the tool we possess to make life easier: live our life better, longer, being (hopefully) happier. The first time I spoke to my supervisor about this project, almost 10 years ago, I remember I was thrilled about it: increasing the conversion efficiency of solar cells by absorption of below band-gap photons seemed, at that time for a 23 years old student, one of the most advanced and powerful miracles human could dream about. It drove most of my professional choices during the following years, up to this point. Being resilient, probably one of the most important characteristics for people in this world, is almost easy and natural when you have commitment, when you have got passion.

This document represents the final thesis of my PhD, focused on the development of intermediate band material by means of solution-based processing and on the chemical and physical aspects behind its realisation. It is intended for an audience already familiar to the nanoscience and nanotechnology fields, as many basic concepts will not be explained in detail throughout the text, but references will be provided (small up-scripted numbers).

If you have an interest on the surface chemistry, electronic properties, colloidal processing of II-IV semiconductor nanocrystals, why and how they can be used in electronic devices, this text could represent a valuable source of information. The topics of upconversion processes and photovoltaic conversion are extremely close when discussing intermediate band materials, meaning that in the text the readers will find, many times, references about the first while considering the second and vice versa, but they represent two different phenomena, so please don't get confused. Indeed, solar cells based on intermediate band material can be seen as a benchmark for the benefits of upconversion layers in several applications.

October 2017,

EAS

Abstract Italiano

I materiali nanostrutturati ricoprono un ruolo di estrema prominenza nel panorama delle tecnologie avanzate grazie alle loro proprietà funzionali, le quali dipendono fortemente dalla dimensione dei cristalli. Ne consegue che l'ingegnerizzazione di tali materiali sia un argomento di primario interesse, al fine di poter ottenere nuovi dispositivi dalle proprietà superiori. Combinando diverse tipologie di materiali, quali ad esempio materiali metallici e/o materiali semiconduttori, è possibile concepire nuovi dispositivi per applicazioni biomediche, sensoristica ambientale e applicazioni energetiche, tra le varie.

Le nanoparticelle di materiale semiconduttore sono ottenute in diversi modi; in questo lavoro verrà presentata la sintesi colloidale poiché è una tecnica economica, facile da configurare, ecologica e può portare a risultati molto interessanti in termini di affidabilità e ripetibilità. La cinetica è uno dei principali fattori a dover essere pienamente compreso per controllare il processo, avendo come obiettivo il raggiungimento di una specifica dimensione e distribuzione dei nuclei. Lo studio della cinetica di sintesi è il motivo per cui è stato investigata l'influenza del rapporto delle concentrazioni dei precursori: si è ottenuta evidenza che una maggiore concentrazione di acido oleico, molecola che si lega agli atomi di cadmio per stabilizzarli, provoca una velocità di crescita delle nanoparticelle più lenta. Queste informazioni permettono di controllare la cinetica della sintesi di CdSe e di ottenere particelle della dimensione di 1,75-2,5 nm, un obiettivo molto difficile da raggiungere a causa della velocità di crescita estremamente alta in condizioni stechiometriche, anche a basse temperature. Basandosi sui dati cinetici della sintesi di CdSe, è stata sviluppata una modifica della Teoria Classica della Nucleazione omogenea (CNT) nella quale si consideri il consumo di monomero durante la crescita di cristalli. Con questa modifica, nella classica curva di equilibrio il cui massimo rappresenta il raggio critico di nucleazione, appare un nuovo minimo assoluto, il quale rappresenterebbe la dimensione di equilibrio tra fase solida e fase liquida (dovuto al limite di solubilità). A conferma del modello di equilibrio di reazione proposto, risulta che gli andamenti sperimentali del raggio medio delle particelle a fine crescita corrispondono con quelli simulati tramite la modifica della CNT. Oltre a fornire nuovi elementi per la comprensione dei meccanismi di crescita colloidale delle nanoparticelle, il modello proposto può contribuire efficacemente al controllo ed all'ottimizzazione della sintesi di nanocristalli di varia natura, grazie alla sua validità

generale, aprendo nuovi orizzonti di sintesi in condizioni “estreme” nello spettro di concentrazione di precursori ed agenti stabilizzanti, dove fino a questo momento la ricerca non si era ancora spinta.

Dopo la sintesi, le nanoparticelle sono ricoperte dall’acido oleico o altre molecole organiche a catena lunga; questa non è una buona configurazione in quanto le molecole a catena lunga, le quali stabilizzano efficacemente le nanoparticelle grazie all'effetto sterico, mantengono i centri funzionali (quantum-dots) troppo distanti gli uni dagli altri durante il successivo processo di assemblaggio. Ecco perché è necessario eseguire uno scambio nelle molecole di capping e sostituire quelle a catena lunga con nuove molecole a catena corta (possibilmente inorganiche). I tioli sono stati la prima scelta, tuttavia il trasferimento di fase mediante tioli non assicurava la completa preservazione delle proprietà optoelettroniche e ci si è quindi concentrati su altre soluzioni.

Una strategia efficace per ottenere strutture complesse core-shell si basa sull’estensione della validità della tecnica colloidale Atomic Layer Deposition (c-ALD), proposta da Ithurria e Talapin ma studiata soltanto per sistemi a base di CdSe-CdS. Sono stati investigati il processo e la sua applicabilità a sistemi metallici (nello specifico core di Au, per il suo alto contrasto al TEM con la shell di CdS) e a base di semiconduttore, ma inserendo nuove configurazioni nella shell (molteplici combinazioni di CdS e ZnS). In base a quanto investigato per la c-ALD, un trasferimento di fase di nanocristalli da soluzione apolare a polare è stato sviluppato. Una volta ottenuta una soluzione stabile che presenti buona fotoluminescenza, i NCs sono stati depositati su substrati di silice e lasciati essiccare in camera a vuoto. Deposizioni in aria o tramite spin coating non hanno fornito i risultati sperati, in quanto la prima soluzione richiede tempi troppo lunghi per raggiungere una rimozione completa del solvente, la seconda invece richiede quantitativi di materiale eccessivi non ancora disponibili in fase di sintesi colloidale. I film sono stati poi sigillati all’interno di tubi in silice nei quali è stato insufflato azoto, in maniera tale da evitare possibili ossidazioni durante l’invecchiamento dei campioni. È stato svolto uno studio cinetico delle trasformazioni che avvengono durante l’invecchiamento dei campioni in funzione della temperatura e del tempo, monitorando l’evoluzione del picco di fotoluminescenza della struttura. Tuttavia, il risultato più eclatante lo si è osservato eccitando la struttura con un laser a lunghezza d’onda inferiore rispetto l’energia richiesta dal band-gap del materiale barriera (E_{CdS}=2.4 eV). Utilizzando il laser a 633 nm (E=1.96 eV), si è osservato un picco a 520 nm (E=2.38 eV). Sono state eseguite le opportune

verifiche, scartando l'ipotesi che si tratti di un picco Raman (non era presente il relativo picco Stokes a 3400 cm^{-1}) e nemmeno fotoluminescenza anti-Stokes, in quanto quest'ultima richiede una dipendenza non lineare con la potenza del laser, mentre il picco osservato ha dipendenza lineare. Queste considerazioni indicano che:

- il picco è dovuto a interazioni di elettroni con singoli fotoni (one-photon photoluminescence);
- l'emissione a 520 nm è molto probabilmente l'emissione band-edge del CdS;
- gli elettroni eccitati provenivano da un livello intermedio (a 1.96 eV dalla banda di conduzione) presente nel band-gap del CdS: molto probabilmente si tratta della banda di valenza dei core CdSe, i quali hanno un gap proprio di 2 eV.

La presenza del picco a 520 nm sotto eccitazione a 633 nm dimostra la capacità della nanostruttura sintetizzata di eseguire upconversion (UC), ovvero di emettere fotoni più energetici venendo eccitata con fotoni meno energetici.

English Abstract

Nanostructured materials are of upmost importance among advanced technologies thanks to their unique properties, which depends strongly on crystal size. Being able to tailor and engineer such materials, so that new devices with superior properties can be obtained, is a hot topic at the present. Functional nanocomposites are a brand new class of materials which possess features that traditional materials can't present; such features, for example opto-electronic properties, strongly depend on the nanoscale dimension of the system. Mixing different types of materials, i.e. creating a nanocomposite based on metallic and/or semiconductor nanocrystals, open the path to develop new devices for biomedics, energy application and environmental sensors, among others.

Semiconductor nanoparticles (NPs) are obtained in several ways; we focused on the colloidal synthesis since it is a cheap, easy to set-up, environment-friendly technique that can lead to valuable results in terms of reliability and repeatability. The kinetics was one of the main factors to be fully understood to be able to control the process, aiming at reaching a certain NPs final dimension and distribution. A first study focused indicated how a higher concentration of oleic acid, the ligands for Cd atoms, causes a slower NPs growth rate, due to the increase of system viscosity. This information allowed to control the kinetics of CdSe NPs synthesis and obtain particles in the range of 1.75-2.5 nm, a very difficult task due to the extremely fast growth rate in stoichiometric condition, even at low temperature. A modification of the classical homogeneous nucleation theory (CNT) has been developed to take in consideration the decrease of monomer concentration during crystal formation and growth. The new free energy curve, now, shows not only the typical maximum associated to nuclei critical size, but also an absolute minimum relative to the mean crystal size at equilibrium between solidus and liquidus (due to the solubility of the system). The trends of crystal size as function of OA concentration estimated using the modified CNT are in perfect agreement with experimental data. The model (embodied in a simulation software) not only represents a valuable tool for the study of colloidal crystal growth providing new insight on the physics and chemistry behind the process, but it also allows to explore new limits in terms of current typical concentration ranges, aiming to the optimization of the synthesis for every single case at hand.

As-synthesized nanoparticles are capped by oleic acid or other long chain organic molecules; thiols have been exploited to phase transfer nanocrystals, but they failed preserving functional properties of the system after the transfer.

A novel strategy aimed to the extension of the validity of a recently proposed technique to create core-shell structure has been investigated: the colloidal atomic layer deposition. The goal was to apply such technique, applied only to CdSe-CdS core-shell structures, to metallic systems and investigate different shell compositions and crystal shapes. Based on the results of c-ALD, NCs phase transfer was performed changing the organic solvent (hexane) with a polar one (n-methylformamide) and stabilizing the nanoparticles with a surface layer of sodium sulfide. Once NCs are completely stripped out of organic ligands, but keep preserving stability and their emission properties, the solution has been drop casted on 0.2x0.2 mm^2 microscope glass substrate and sealed in a vacuum chamber overnight for the evaporation of the solvent. To avoid possible oxidation of the films during next annealing step, samples have been inserted in glass tubes and sealed within under nitrogen flow. A kinetic study has been performed on the films, investigating the effect of annealing time and temperature on the photoluminescence spectrum of samples.

When excited with a wavelength (633 nm) larger than the gap of the barrier material (CdS, E_{gap}=2.4 eV), annealed films presented a weak emission peak at 520 nm, associated to the band-edge emission of the shell. We proved that the peak at 520 nm is not a Raman peak, since there is no evidence of its Stokes counterpart located at 3400 cm^{-1}, and it is no anti-Stokes PL. In this latter case, a multi-photon absorption would be requested, and the emission intensity shall present a non-linear dependence with the laser power. In our samples, on the contrary, a linear behavior is observed, indicating the absorption of one single photon per transition. All these results indicate that:

- the PL peak is located exactly where the band-edge emission from CdS barrier material is expected;
- the PL peak is caused by the absorbance of single photons, no multi-photon effects;
- the light at 633 nm (1.96 eV) excites electrons located in an “intermediate state” within the CdS band gap. This is the most likely explanation for the detected emission. The intermediate states could be the CdSe core valence band, which is fully filled by electrons, and its energy value is 2 eV behind the system conduction band.

The low efficiency of the upconversion process could be due to the extremely thin film produced (which causes a reduced portion of photon absorbed): new investigations will be performed in this sense.

Table of Contents

Preface 5
Abstract Italiano 6
English Abstract 9
List of Figures 14
Introduction 17
Fundamentals 20
  Physical chemistry of nanocrystals 20
    Quantum confinement effect and properties of NCs 20
    Surface science of nanocrystals 23
  Intermediate band materials 25
    State of the art 27
  Upconversion effect 29
Experimental methods 32
  Materials 32
  Requirements for the intermediate band architecture 32
  Colloidal Synthesis 35
    Nucleation and Growth 36
  Core-shell development and surface passivation 42
    SILAR 42
    Colloidal-Atomic Layer Deposition 43
  Phase transfer of nanocrystals to polar or nonpolar media 46
  Deposition of colloidal solution 47
  Thermal treatment and sintering of nanostructure 48
  Characterization Techniques 48
Results and Discussion 49
  CdSe core synthesis 49
    Kinetics of synthesis 50
    Thermodynamic model 54
  Core-shell systems 61
    Silar technique 61

Semiconductor-semiconductor systems by c-ALD 61
Metal-semiconductor systems by c-ALD 70
Phase-Transferred NCs 73
Half-monolayer transfer by sodium sulphide 74
Thin Films 75
As-deposited films 75
Sintered films 76
Further considerations 82
Cost of nanofabrication 82
Safety at the nanoscale 84
Conclusion 86
Future perspectives 86
References 88
Acknowledgements 99
Appendix A 100
Appendix B 102

List of Figures

Figure 1 – trend of publications containing the keyword “nanotechnology” in the timespan 1980-2020. Reference: Scopus database. 18

Figure 2 – schematic representation of the first electronic transitions for a generic nanocrystal and their contribution in terms of absorption spectrum. 22

Figure 3 – schematic representation of sterically and electrostatically stabilized crystal and a core-shell NCs with a sectioned shell portion to visualize the inner core 24

Figure 4 – scheme of a quantum dots heterostructure with its electronic structure. 27

Figure 5 – schematic representation of the QD-IBSC as designed by University of Glasgow/IES-Universidad Politecnica de Madrid 29

Figure 6 – upconversion process. 30

Figure 7 – valence band and conduction band energy level for common bulk II-VI semiconductor materials 33

Figure 8 – experimental setup concept and actual instrumentation for the synthesis of colloidal NCs. 36

Figure 9 – Gibbs free energy curve. 38

Figure 10 – La Mer plot. 38

Figure 11 – modified free energy curve for a closed system. 41

Figure 12 –additions of shell layers on cores. 44

Figure 13 – time evolution of particle size and particle dispersion for a representative synthesis ([Cd]:[OA]=1:10, T=235°C). 49

Figure 14 – evolution of the FWHM over time for the representative case of the synthesis at 270°C and variable [Cd]:[OA] ratio. FWHM of the PL spectrum at the end of the growth stage, as a function of temperature and [Cd]:[OA] concentration ratio. 50

Figure 15 – kinetic parameter, *k*, as a function of the cadmium-to-OA ratio 51

Figure 16 – size at the end of the nucleation stage, d_0, as a function of the [Cd]:[OA] ratio and "equilibrium size map". 52

Figure 17 – comparison of experimental and simulated growth values for our dataset. . . .56

Figure 18 – crystal mean size as a function of oleic acid amount during synthesis. 57

Figure 19 – experimental and simulated values for the growth of CdSe nanocrystals in organic media using TMPPA or OA as ligand. 58

Figure 20 – experimental data as found in ref [49,55,101] for crystal concentration, temperature, monomer concentration and growth temperature. 60

Figure 21 – absorption and photoluminescence spectra for CdSe cores and for CdSe/CdS core-shells. Transmission electronic microscopy images for core and core-shell systems in hexane. 61

Figure 22 – scheme of the investigated shell combinations with corresponding energy band diagrams of CdSe, CdS and ZnS. 63

Figure 23 – evolution of the absorption and the PL spectra as well as values of the Stokes shift of CdSe NCs during their alternate shelling with CdS and ZnS forming the CdSe/CdS/ZnS/CdS/ZnS structure. PL spectra of the initial CdSe and the final multishell NC structure. 65

Figure 24 – TEM images taken at different magnifications of the initial 3.8 nm core CdSe NCs and the resulting CdSe/ZnS/CdS3 core/shell NCs. 66

Figure 25 – powder XRD patterns measured for CdSe core and CdSe/CdS3/ZnS heterostructure NCs. 67

Figure 26 – evolution of the $1S_e$–$1S_h$ transition energy for different shell configurations with CdS. 69

Figure 27 – evolution of the $1S_e$–$1S_h$ transition for different shell configurations with ZnS. 69

Figure 28 – diagram representing the value of the $1S_e$–$1S_h$ transition (in eV) for seven different shell combinations. 70

Figure 29 – TEM images of the Au cores and the Au/CdS7 core/shell NCs. 72

Figure 30 – absorbance spectra of the initial Au core (with diameter of ~4 nm) and core/shell Au/CdS NCs with varied shell thickness functionalized with oleylamine and dissolved in toluene. Powder XRD patterns of the Au core, Au/CdS3 and Au/CdS7 core/shell NCs. 73

Figure 31 – absorption and PL intensity spectra for core-shell QDs in hexane and after the transfer to water. 74

Figure 32 – optical spectra before and after phase-transfer by sodium sulfide. 75

Figure 33 – absorption and emission spectra for one characteristic sample and XRD. 76

Figure 34 – gaussian fitting of the PL spectrum for one exemplificative sample. 77

Figure 35 – maps showing evolution of PL wavelength during sintering. 78

Figure 36 – PL wavelength shift during sintering at different temperatures. 79

Figure 37 – upconversion peak with gaussian fitting. 81

Figure 38 – band-edge emission intensity at 520 nm of sintered CdS film as a function of excitation power. 81

Introduction

Nanotechnology is the branch of science which deals with objects at the nanoscale, where one nanometre (nm) is one billionth of a metre, to get a feeling about such scale, we can imagine take a hair and subdivide its diameter 200 thousand times; one of that parts is roughly the size of one nanometre. At this scale, material properties depart strongly from what we are accustomated about, de facto representing the bridge between bulk material and its atomic realm. Crystals at the nanoscale are characterised by a high surface-to-volume ratio, due to their reduced size, and thus surface effects are dominant. Bulk solids present only a tiny percentage of surface atoms in their structure: dandling chemical bonds and other surface effects negligibly contribute to the material properties. Surface-to-volume ratio scales inversely with linear dimensions, and become dominant at the nanoscale. The surface represents the interface between crystal and external environment and strongly regulates how these two entities interact with each other. At the nanoscale, surface can easily modify the material properties (like melting temperature[1], solubility and luminescence[2]) and generate new ones (like surface-enhanced plasmon resonance[3]).

Nanotechnology is quite a modern field of science, as it was first conceptually introduced by Richard P. Feynman in its speech "There is plenty of room at the bottom" in 1959. Nevertheless, the term "nanotechnology" was used for the first time only 27 years later, in the book "Engines of creation: the coming era of nanotechnology" by K. Eric Drexler (1986). Since then, documents containing the keyword "nanotechnology" has grown sensibly in the 2000-2010 decade, reaching a maximum of almost 12 thousand in 2013 (Figure 1). In the last few years the trend seems to have slowed down a little, but its fast expansion has been impressive. The advent of nanotechnology, anyway, had arisen several concerns in the early 2000s, and some debates are still in progress. In 2003, the Royal Society and the Royal Academy of Engineering compiled an independent report* focused on the already established fields of application of nanotechnology, the future trends and new opportunities, and the challenges in the domain of safety and health. At that time, there was no clue about the impact on safety and environment, and about the ethical and political implications the development of nanotechnology could produce. The goal of the

* the complete report is available at the website: http://www.nanotec.org.uk/finalReport.htm

Royal Society was to "provide an overview of current and potential future developments in nanoscience and nanotechnologies against which the health, safety, environmental, social and ethical implications can be considered", reasonably proposing regulations where and when needed. In the meanwhile, commercialisation of the first nanotechnology products emerged, in some cases with large investments and fund promotions by governments. We have witnessed several innovations introduced during the intensive research at the nanoscale performed so far in the field of energy storage[4,5], drug-delivery[6] and disease treatment[7], water purification[8], sensors and transistors[9]; and yet, so much could still be achieved in the next future.

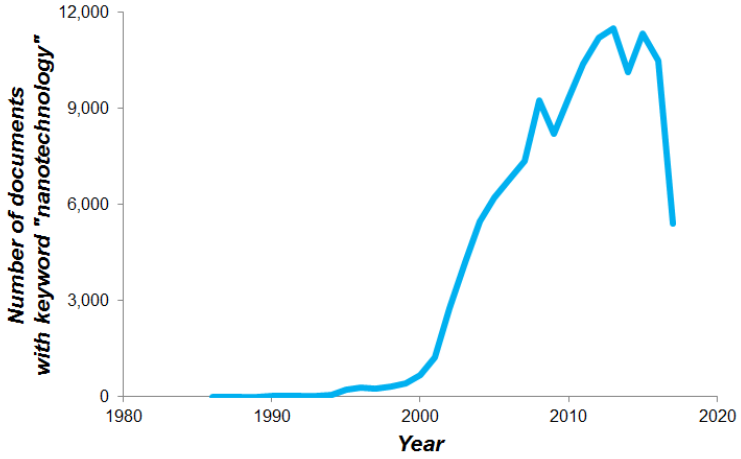

Figure 1 *–trend of publications containing the keyword "nanotechnology" in the timespan 1980-2020. Reference: Scopus© database.*

Nanocrystals (NCs), the building-blocks of nanotechnology, usually present sizes in the range of 2 to 50 nm. At this scale, the quantum overlapping of thousands of atomic states is sufficient for the development of energy bands of metal and semiconductor materials. In this regime, the electronic structure can be tailored simply controlling the physical size of the crystal, giving access to nanoscopic control of material properties and leading to novel phenomena like superparamagnetism[10] or semiconductor band-gap size-dependency[2]. Unfortunately, up to now, cheap and simple processes to control the inorganic semiconductor chemistry at the nanoscale have not been developed yet, even if solution-based processing would present enormous benefits for the production of large square-metre nanocrystal-based devices, first of all the cost reduction for the manufacture

of electronic and optoelectronic nanoscale components. There are two main approaches to develop nanostructures: top-down and bottom-up. While the first permits the processing of larger volume, it depends on long, complex techniques and expensive instrumentations, precluding mass-production advent; on the other hand, bottom-up synthesis are easily scalable-up, very often simple and cheap, and the size tuning has improved dramatically in the last years. What prevented, so far, the industrialisation of nanocrystal-based systems is indeed their intrinsic limitation to produce monodisperse material with high throughput, at the present technological state. Microfluidic reactors, for example, have been proposed to obtain a continuous production of nanocrystals[11,12], thus overtaking the limitations related to complex, time-consuming and small-amount batch reactions.

In this context, the aim of this research project is to provide a valuable contribution to the current scientific knowledge of the surface chemistry and property-tunability of nanomaterials and propose a solution-based, fully-colloidal route to produce functional nanoheterostructure in a cheap, environment friendly, easy to set-up way.

Fundamentals

In this chapter, the fundamental concepts related to physical-chemistry, nanocrystals, colloidal stability, electronic transitions will be presented. Physical chemistry of nanocrystals is still an evolving science: novel concepts about material electronic structure, colloidal stability, interactions matter-light and many others need to be introduced to successfully address and understand the complex phenomena at the nanoscale. This chapter is intended to provide a general overview on the state of the art of these topics. Since the main project is focused on the synthesis and development of quasi-spherical structures, limited emphasis will be placed on other shapes (nanorods, branched nanocrystals, nanoplatelets, etc.), even if they represent an extremely prosperous research field nowadays.

Physical chemistry of nanocrystals

The term "quantum dot" indicates a particular type of nanocrystals (prefix "nano" means we are dealing with nanoscale objects, i.e. object with size around 10^{-9} metre) composed of semiconductor materials. When their size is in the range of the Bohr radius, i.e. the size of an exciton, the transition from bulk material properties to molecular ones occurs. At this scale, functional properties are easily tailorable by controlling the crystal size and composition.

Quantum confinement effect and properties of NCs

The spatial confinement of excitons (electron-hole pairs) in semiconductor nanomaterials lead to the phenomena known as quantum confinement, which strongly

influences the electronic structure of the material. For a comprehensive and extensive discussion about the quantum confinement effect, readers are invited to look at to the book "Nanoparticles" edited by de Mello-Donegà[13] or other references[14,15]; in this text we will provide only a short but essential analysis.

Solid crystals can be thought of as periodic potential for charge carriers like electrons. The wave function representing the distribution of the electron in solid crystals are expressed by the Bloch theorem, which describe any wave-like phenomena in a periodic medium[16]. The Bloch wave functions describing the bulk properties of semiconductors are still valid at the nanoscale, but the addition of an envelope function, which takes into account the spatial confinement of charge carriers, is required. The envelope function represents the Schrödinger solution of the particle-in-a-box problem, with same confinement in every direction and thus a spherical box potential (quantum dot, QD). In the situation of strong confinement regime, which holds when the NC radius is smaller than the Bohr radius of the exciton, the kinetic energy of the charge carriers is much larger than the Coulomb interactions between them, and therefore electrons and holes are no longer correlated and can be treated separately. The effect of the quantum confinement is usually no longer evident once the NC radius in larger than 2-3 times the exciton Bohr radius. In the weak confinement regime, the electron-hole pair cannot be treated separately and the exciton is taken in consideration. Two main consequences of the quantum confinement effect are striking:

1. The band gap of semiconductor material become larger with decreasing crystal size;
2. Discrete energy levels appear at the band-edges of both the conduction and valence band of the material.

These consequences mean that the optical and electronic properties of semiconductor, mainly correlated to their band-gap, can be easily tuned by simply controlling the size of the NCs. We can get evidence of the quantum confinement effect looking at the absorption and photoluminescence (PL) spectra of different size NCs. For the absorption, discrete energy levels in quantum dots are separated by hundreds of meV, meaning that these transitions are well resolved in optical absorption spectra (Figure 2). The PL is associated to the band-edge radiative recombination of excitons; PL spectra present one single peak, and the position of the peak provides thus indication about the size of the NCs, as in the

absorption spectrum. It should be noted that the emission transition is the reverse of the first absorption transition.

Radiative recombination is not the only way electrons and holes can relax from excited states. There are several other non-radiative pathways for excitons. When the absorbed photon energy is large enough, the electron is promoted in the further levels within the conduction band. From here, it can relax down to the band-edge by means of a cascade of intraband non-radiative relaxation steps, dissipating its energy as heat. Non-radiative recombination is usually mediated by defects or impurities. Localization of charge carriers on traps, mainly surface states caused by dandling bonds on NCs, induces a limited overlapping of the electron and hole wave functions, resulting in a less likely radiative recombination process and quenching of photoluminescence, thus promoting relaxation with local vibrations (coupling with phonons). In some cases, radiative emission is still possible even from trap states, but in this case the PL energy is lower compared to the band-edge emission. Reduction of dandling bonds on the surface of nanocrystals is therefore of upmost importance, and several strategies have been developed to address this issue.

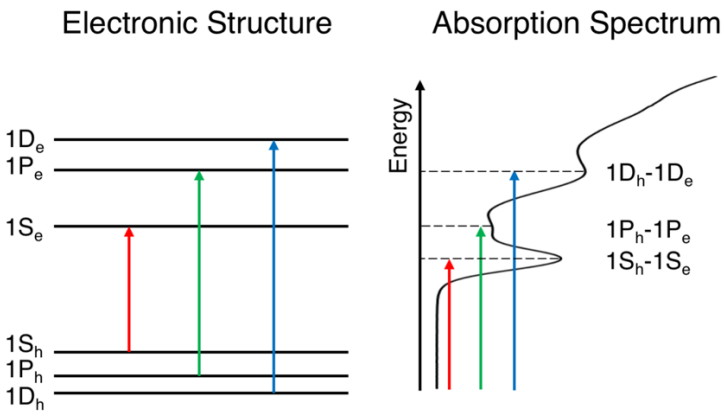

Figure 2 *– schematic representation of the first electronic transitions for a generic nanocrystal and their contribution in terms of absorption spectrum.*

Surface science of nanocrystals

Due to their reduced size, nanocrystals present an extremely high surface-to-volume ratio, meaning that their surface plays an important role in the definition of their properties. Defects on the surface, impurities, dandling bonds are detrimental for the functional properties of the assemblies, that's why specific passivation processes are required to preserve optical and electronic properties of the crystals[17,18]. Controlling surface chemistry is also a necessary approach to stabilize NCs in different media, both sterically and electrostatically, and in some cases facilitate the self-assembly at the nanoscale to obtain opto-electronic devices. The most common passivation agent for NCs are organic long-chain molecules; they provide a long-lasting stability in nonpolar solvent (like hexane, 1-octadecene, toluene, etc.) and since the solution-based processing of nanostructure in organic media is largely used to synthesize NCs, this type of surface ligands is the natural choice. As it will be illustrated in the next sections, organic ligands play an important role on the growth rates and kinetics of colloidal synthesis in general: mixtures of ligands are responsible to the development of complex and inhomogeneous structures like rods[19], platelets[20], tetrapods[21] and octapods[22]. While ligands are fundamentals for the stabilisation of NCs in solution, there are two different approaches to reach this condition:

1. Steric stabilisation – long chain organic molecules form a continuous layer around the crystals, keeping them far away one from each other, and in the case of good solvent hindering any type of aggregation. This is due to the fact that the interactions between surface ligands and solvent molecules are promoted by the decrease of free energy. When immersed in a non-solvent, instead, the interactions ligand-ligand are favoured compared to the ligand-solvent ones, and this cause the shrinkage of capping layer and aggregation of crystals.
2. Electrostatic stabilisation – in this case, charged species are absorbed on the surface of NCs and neutrality is guaranteed by the presence of oppositely charged counterions in the diffuse layer around the particles. Good solvents for electrostatically stabilised systems are the one with high dielectric constant.

Ligands at the nanoscale fall in one of three categories, depending on the interaction mode and number of electrons taking part in the metal-ligand bound[18]: L-type, X-type and Z-type molecules. The first ones are neutral two-electron donors, with the electron pair

datively coordinating surface metal atoms; in this group we can find amines and phosphines. X-type ligands, instead, present an odd number of valence electrons. This means that they need one more electron from the NCs surface atoms to form a covalent bond; very often, the metal-ligand bond is cleaved forming ionic specimen. Examples of this group of molecules are carboxylates and thiolates. These two types of electron rich molecules bound on the electrophilic (electron-deficient) surface sites of NCs. The last category, Z-type ligands, are two-electrons acceptors, meaning that they bound on electron rich surface sites. Depending on the nanocrystal facets exposed (which can be polar or non-polar) L-type or X-type ligands dominate the capping shell composition. It is important to consider also the polarity of the solvent: NCs ought be neutral in non-polar solvent like hexane or toluene, adding one more constraint for the capping shell composition. These considerations are fundamentals when a ligand-exchange process has to be performed: crystal neutrality in non-polar solvent favours the fast dynamic bonding-unbonding for L-type and Z-type ligands, but not for X-type ones (which would leave a charged crystal when removed from the surface). The use of polar solvents lifts the requirement for an electrically neutral surface, permitting more ligand exchange pathways.

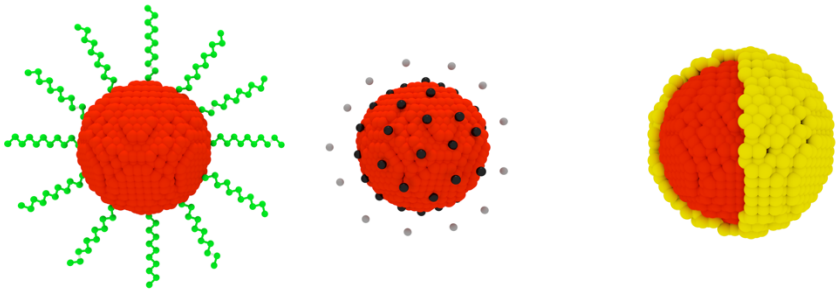

Figure 3 *– schematic representation of sterically and electrostatically stabilized crystal (left and middle). On the right side, a core-shell NCs with a sectioned shell portion to visualize the inner core.*

Another way to passivate the surface of NCs is based on the deposition of a wider band-gap material on top of the core particle, thus producing hybrid structures[23,24]. This heterostructure configuration is widely used since it provides an extremely effective localisation of the charge carriers inside the inner component of the system, with little displacement of the electron and hole wave functions in the outer component; in this way it is very unlikely that a charge carrier could interact with surface traps, and the NCs properties are preserved. There are three possible configurations for these core-shell

systems, depending on the relative position of the energy bands. In the Type-I configuration, a wider band gap material composes the shell, and excitons are confined within the core structure. Classic examples of this systems are CdSe/ZnS and CdS/ZnS coupling. In the Type-II regime, instead, the alignment of energy levels leads to the spatial separation of electron and hole, i.e. their wave functions are no longer overlapped, resulting in longer lifetime for charge carriers. Examples of this type of configuration are CdTe/CdSe and ZnSe/CdS. The last type is an intermediate configuration between the two already discussed: in quasi-Type-II regime the delocalisation happens for only one charge carriers, while the other remains confined in a specific part of the heterostructure. For example, CdSe/CdS hybrid system presents the alignment of the conduction band but a large offset for the valence band; the reverse configuration can be found for example in ZnSe/CdSe system. Not all material combinations are possible when trying to obtain a core-shell heterostructure: lattice mismatch is responsible of the occurrence of strain at the interface between core and shell, leading to possible cracks on the structure. In this sense, the realisation of hybrid compositional nanomaterials (coupling metals and semiconductors) have always represented a goal not easily achievable due to their large lattice mismatch, even if pairing exciton and plasmon characteristics could originate novel functional properties[25,26].

Intermediate band materials

The concept behind the intermediate band structure is quite simple: intermediate states are levels localized inside the forbidden band gap of the material, playing an important role in the electronic transitions. This states shouldn't be traps in the common sense, since they must provide very low recombination rates, at least lower than the generation ones[27]. There are two main category of charge carrier recombination, as seen in §1: the first one is radiative, and it is the unavoidable counterpart of the generation of free charge carriers by light absorption; the second one is associated with energy transfer to phonons or to other excitons (Auger), resulting in non-radiative recombination. Multi phonon emission (MPE) is the most likely mechanism for non-radiative recombination to compensate the balance between the high energy of a photon and the low energy amount of a single phonon; it is responsible for the well-known Shockley, Read and Hall (SRH)

recombination. Intermediate states, thus, have to provide a pathway for exciton generation, but not for their recombination. Suppressing recombination from these levels is not easy, but as Luque at al.[27] pointed out, an high density of traps introducing deep levels could substantially suppress non-radiative recombination, thanks to the delocalisation of the trapped electrons charge density. In fact, when an electron is trapped on a defect, it induces a displacement of the trap due to the charge localization, and consequently MPE recombination. But when the density of trap is high enough, this process is suppressed. Estimation of the required density of impurities in the material is 10^{21} #/cm^3. Such intermediate band material could be exploited as active part of a light-harvesting device and solar cell, since electromagnetic radiation might be collected in a more efficient way (even below bang-gap photons are absorbed, as long as they have enough energy for the intermediate band transitions). Solar cells could benefit greatly from this configuration, since a maximum conversion efficiency of 63.1%[28] could be achieved instead of the Shockley and Queisser (SQ) model limit[29] for conventional solar cells (33.7%). The optimal conditions to reach such high efficiency are, mainly, a barrier band-gap of 1.95 eV and an IB level located 0.71 eV below the conduction band, with its states half-filled and operating at maximum sun concentration. The Fermi level, which represents the statistical distribution of charge carriers within the energy states, should be in the middle of the IB, granting rooms for electrons from the Valence Band and at the same time containing electrons to be promoted to the Conduction Band.

To fabricate a structure presenting controlled intermediate levels, one way is to create a crystal where the defects (providing the trap states) are located with a precise spatial periodicity; this would suppress several vibrational states for the traps and reduce sensibly non-radiative recombination, as explained before. The idea of embed semiconductor NCs (quantum dots, QDs) as "defects" providing the intermediate levels within a wider band-gap semiconductor (host or barrier material) was introduced by Luque and Martì in 1997[28]. To fabricate a quantum dot intermediate band solar cell (QD-IBSC), the QDs-array has to be sandwiched between a n-emitter and a p-emitter; this condition is not required in this work, since the aim of this project is not the development of a fully-operational solar cell: emitters are necessary only when charge carriers have to be separated, i.e. for a solar cell to work properly. Instead, this work in focused on the development of a solution-based processing to fabricate intermediate materials, irrespectively if the photoactive film will be introduced in a solar cell, a light emitter or

whatever else. The electronic structure of a QD-IBSC is represented in Figure 4. Most of the IBSCs fabricated so far are made of InAs as QDs and GaAs as barrier material[30–32]: when the InAs is epitaxially deposited on GaAs, QDs are spontaneously formed due to the large lattice mismatch between the two materials, following a Stranski-Krastanov mode[33]. The InAs/GaAs combination is not the best, since the barrier band-gap and the intermediate band energy level cannot provide the optimum conditions to obtain the 63.1% efficiency, evaluated for an ideal model, but the already developed knowledge about its fabrication was the main motivation for its choice.

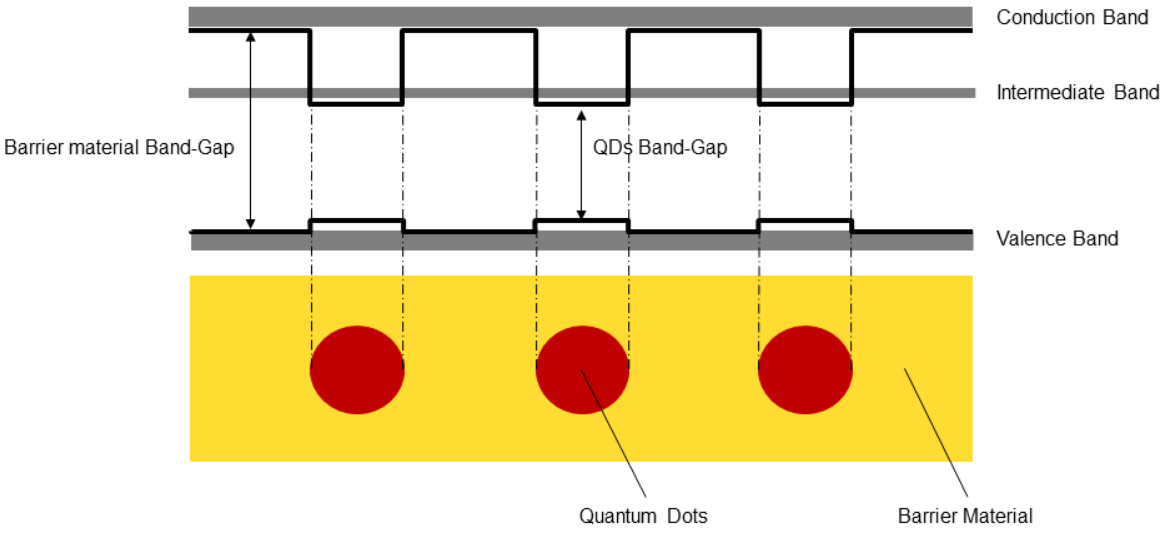

Figure 4 *– scheme of a quantum dots heterostructure with its electronic structure. The yellow continuous phase represents the barrier material, red spheres are quantum dots. On top, electronic configuration is presented for the optimal IB material, with IB formed by the quantum dots energy levels.*

State of the art

Semiconductor quantum dots IB materials have been developed for one single application so far: solar cells. There is so many benefits this type of structure can bring that it is extremely reductive to focus only on the development of solar cells, but for technological reasons any other application has not been investigated yet, if not only theoretically. Luminescent materials presenting intermediate states are one class of materials used for upconversion processes and they are mainly based on lanthanide compounds and organic dyes (see next section), but they represent another field of

application for semiconductor-based IB structures. The first intermediate band solar cell appeared to the world in 1997[28], and it represents the first example of material designed to exploit below energy-gap photons. Many others have been fabricated with time[34–36], with stacks of several layers (usually no more than 10) of QDs array between the two emitters. To avoid electron tunnel and voltage losses, thin conventional p-layer and n-layer (so-called Field Damping Layers) are placed between the QDs array and the n-emitter or p-emitter, respectively[37]. The spacers between QDs layers have variable thickness, from 10 nm up to 80 nm[38]; the thicker spacer option has the benefit of lower stresses due to lattice mismatch between QDs layers. Other techniques for stress compensation have been proposed, based on the deposition of different materials, but they might interfere with the electronic structure and cause other performance losses. This type of QD-IBSC reached an efficiency of 10%, roughly. A schematic representation of the QD-IBSC structure is presented in Figure 5. This stacked structure was developed using Molecular Beam Epitaxy (MBE), performed at high vacuum condition and with very low deposition rates (less than 3 μm per hour). Once the deposited material reaches the critical height, the stresses are so intense that the film breaks into island, elastically relaxing the structure. This process is sometimes referred to as self-assembly of quantum dots. In this text, anyway, we will use the term self-assembly of NCs as the surface chemistry coordinated process by which nanocrystals arrange themselves spatially on a substrate; we will discuss it in detail in the next chapters.

It is clear that such complex structure and long, precise processing are not the optimal elements to promote large-scale diffusion of IB materials, main limitation of the slow progress occurred in the last decade. Even if the extremely high structural control can guarantee the fabrication of high performance QD-IBSC, it would be impossible to scale-up this technique at the present technological state. Given for granted the possibility for IB materials to contribute to a leap forward in terms of energy harvesting and optical/electronic devices technology, a reliable, simple and scalable processing is requested to promote research and innovation in the field.

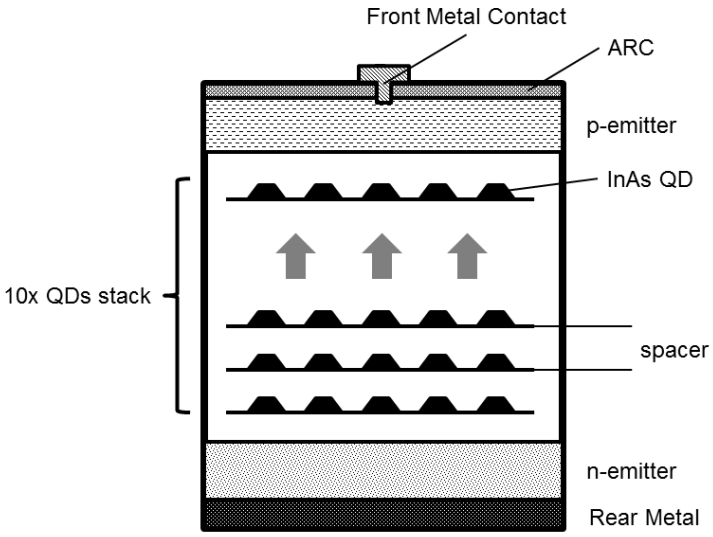

Figure 5 *– schematic representation of the QD-IBSC as designed by University of Glasgow/IES-Universidad Politecnica de Madrid, with 10 QDs layer separated by thin spacers. FDL are not represented here.*

Upconversion effect

Upconversion is the process by which low energy photons are converted to high energy photons by means of electronic transition via intermediate states. Such type of materials con find application in several fields, from luminescent devices, to theranostics to photovoltaics. There are two different big families of upconversion materials: they are usually composed of either doped lanthanides or organic dyes[39,40]. Trivalent lanthanide ions have an electronic structure which presents numerous energy levels in the partially filled 4f shell, allowing multiple radiative transitions. The outer electron filled shells (5s and 5p) shield the ions from the environment, preserving the transition of the 4f shell which are only marginally affected by the surrounding, meaning their emission is stable and constant. Organic upconverter are based on a multiple steps process, based on absorption, energy transfer, excitation of higher energy states and emission in the so called triplet-triplet annihilation mechanism[40]. It requires the simultaneous presence of at least two different molecules: the sensitizer and the emitter (or activator); each of them is responsible of different steps of the process. Efficiency values for these types of upconverter

are, in the best scenario, lower than 15%. Nanocrystal upconverters have not been a diffuse option, since they are typically a factor of 1000 to 150000 less efficient than their bulky counterpart[39]. The lower efficiency has been related to the surface quenching occurring at the nanoscale, due to the high surface-to-volume ratio characterising NCs. The few examples of nanocrystal upconverters reported were all made up of rare earth elements phosphors[40]. The fine control of size, shape and composition of NCs during synthesis indicates that large room for improvement are available in terms of upconversion quantum yield for these systems. In this context, one big issue about NCs upconverter is related to the estimation of their internal upconversion quantum yield, since it is very challenging to measure precisely the amount of photons absorbed by the crystal, putting aside absorption from capping layer and other impurities.

The two main figures-of-merit for the upconversion process are the internal upconversion quantum yield (iUCQY) and the external upconversion quantum yield (eUCQY). As for solar cells, they are the ratio of flux emitted of upconverted photons to the flux absorbed by the sample or the incident flux on the sample, respectively. These two figures are very important, as they evaluate the performance of the upconversion device. Typical values are below 15% for the iUCQY and below 10% for eUCQY[39].

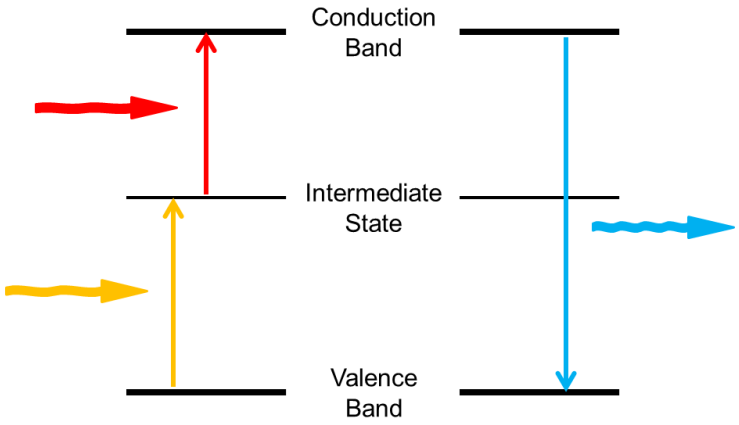

Figure 6 *– Upconversion process: two low energy photons are absorbed through an intermediate state (left); one high energy photon is emitted due to radiative recombination (right).*

The main reasons a single junction solar cell cannot overcome the SQ 33.7% efficiency limit are: above band-gap photons will thermalize and lose part of their energy (hot electrons), below band-gap photons won't be absorbed; these two mechanisms alone

amount for the loss of about half the incident radiation energy. New concepts have been introduced to overcome the SQ limit, from multiple exciton generation, where one high energy photon creates a pair of excitons, to multi-junction solar cells based on III-V semiconductor technology, demonstrating conversion efficiency up to 46%[41,42]. Anyway, complex processing and precise control over the fabrication parameters prevent these technologies to become cost-effective and open their diffusion up. Upconversion is another process to modify the solar spectrum and improve conversion efficiency. Conceptually, upconverter are devices which take two or more low-energy photons, excite an electron to high-energy states and from here it could radiative recombine and emit one high-energy photon. Combining an upconverter with a solar cell means that below band-gap photons of solar radiation, not absorbed by the solar cell in the first moment, are converted to high-energy light by the converter and directed again to the solar cell to be harvested. Right now, all existing upconversion materials have three main limitations: only a narrow band of incident photons can be absorbed, much of the energy is converted to heat, the upconversion probability is usually very low[43].

Experimental methods

In this chapter each processing step for the development of quantum dot-based semiconductor films is described. After the list of materials used for the experiments and the requirements to produce a working intermediate band material, details are provided for each single experimental procedure.

Materials

All chemicals have been used as received, without any modification or further purification. Cadmium oxide (CdO, 99.5%), oleic acid (90%), 1-octadecene (ODE, 90%), selenium powder (99.999%), sulfur powder (99.98%), cadmium acetate dihydrate ($Cd(OAc)_2 \cdot 2H_2O$, 99.99%), zinc acetate dihydrate ($Zn(OAc)_2 \cdot 2H_2O$, 99%), *n*-methylformamide (MFA, 99%), sodium sulfide (Na_2S, 97%), tetrachloroauric acid trihydrate ($H[AuCl_4] \cdot 3H_2O$, 99.9%), tert-butylamine-borane complex (97%), tetraline (95–98%), oleylamine (OLA, C18 content 80–90%) and tri-*n*-octylphosphine oxide (TOPO, technical grade) were purchased from Sigma-Aldrich. Tri-*n*-octylphosphine (TOP, 97%) was purchased from ABCR. Octadecylphosphonic acid (ODPA, 97%) was purchased from PlasmaChem.

Requirements for the intermediate band architecture

There are several strict constrains for the intermediate band to work properly, and not represent just a defective structure[44]. Beside the main trade-offs required for the common solar cells, here below the main parameters involved in the design of a semiconductor quantum dots IB material are listed. These considerations have been made for an QD-IBSC, but they have general validity even for our configuration, removing only the constraints related to the electrical current production, which will not be mentioned in

the list. All the features listed below have been taken in consideration during the design and development of our experimental intermediate band material.

Material choice – material pairing is necessary between barrier and quantum dots in terms of optimal electronic structure. The optimum host band-gap was estimated to be 1.95 eV, with an intermediate level placed 1.24 eV above the valence band (and 0.71 eV below the conduction band)[28]. This pairing would provide, under maximum sun-concentration, the top efficiency of 63.1%. While Luque and Marti suggest the alignment for barrier and quantum dots valence bands, we opted for the opposite configuration, for operational reasons explained later in this chapter. CdS was selected as barrier material, with a bang-gap of 2.4 eV, and CdSe as quantum dots. The offset of the bulk Conduction Bands is tiny, only 0.1 eV. Controlling the QDs size during colloidal synthesis, a maximum efficiency around 60% would be expected for such barrier band-gap with an intermediate level at 0.9 eV[28]. Zn compounds are extremely sensitive to oxidation, main reason they have not been chosen, while Te-based crystals presented complex surface chemistry which required a long investigation before application. The CdSe-CdS system was selected thanks to our previous experiences, as it represents a fair trade-off between model ideality and well-known processing.

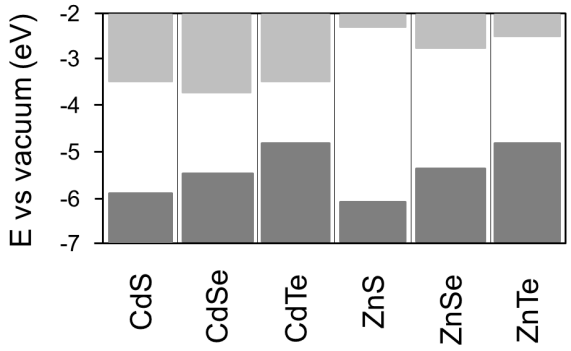

Figure 7 *– Valence Band and Conduction Band energy level for common bulk II-VI semiconductor materials.*

Dot size – as mentioned in the previous chapter, the quantum confinement effect guarantees the fine-tuning of NCs electronic structure as a function of crystal size. Controlling the colloidal synthesis is a way to obtain the desired energy band configuration. There is an upper limit for the intermediate energy level, since it cannot exceed the valence band-edge of bulk CdSe, the quantum dots material. In this work, we

obtained an IB located 0.5 eV above the valence band. For practical reasons, dot size should not exceed the value related to the appearance of secondary energy levels within the barrier band-gap.

Dot spacing – density of QDs is an important parameter for two reasons: the NCs have to be close enough to allow overlapping of electron wave functions among dots, constituting a continuous band and not just localised separate levels, and secondly it should be high enough to suppress non-radiative recombination[27,44]. Reduced dot spacing will promote, also, the absorption of incident radiation. One side effect of limited dot spacing is the increase of IB bandwidth, due to the splitting of energy levels[45], but it not represents a real issues for the CdSe/CdS system. In our experiments, we deposited a concentration of NCs two orders of magnitude larger than the recommended value of 10^{21} #/cm^3. In terms of solution-based processing, controlling dot spacing means to define precisely the shell thickness for core-shell nanocrystals.

Dot regularity – monodispersed nanocrystals are a requisite for intermediate band materials: polydisperse QDs would cause an increase of bandwidth and the localisation of wave functions, promoting non-radiative recombination. A dispersion in the order of 10% is sufficient to avoid this drawbacks[44]. In our experiments, we were able to synthesize CdSe NCs with a dispersion of 15%.

Doping – for a IBSC to work properly, the intermediate band have to be half-filled of electrons, so that electrons can be promoted from intermediate band to conduction band and from valence band to intermediate band[44–46]. In our case, instead, such configuration is not required, since we were not focused on the operational of a solar cell but only on the demonstration of an upconversion effect. This was the reason we opted for an alignment of the conduction band and so a completely filled intermediate band: with below band-gap excitation we promoted electrons to the conduction band, and observed their radiative recombination as proof-of-concept. Some preliminary experiments with doped films have been performed, but this line was abandoned early.

Sintering temperature – the thermal treatment is the last step to create the IB material architecture. During the process, NCs sinter together to form a continuous matrix composed of the shell semiconductor. Interdiffusion between core and shell material has to be avoided, since alloying would cause a substantial modification of the electronic structure. Sintering temperature for bulk compounds usually is 2/3 of their melting

temperature; at the nanoscale, this figure varies a lot with size, thus it is not easy to fix a sintering temperature. Multiple experiments have been performed in the range 300°C to 550°C, getting evidence of interdiffusion for small crystals[47]. Bigger NCs treated at the same conditions didn't present the formation of alloying.

Colloidal Synthesis

For applications in optical and electronic devices, size and size uniformity are extremely important. This leads to the need of a reliable control over the evolution of size and size distribution, as well as over the composition and the surface ligands chemistry during the synthesis. Two main routes have been proposed so far for fabricating nanocrystals: a top-down approach based on reducing crystal's size by physical methods, and a bottom-up approach relying on colloidal chemistry. While the first has the benefit to enable production of monodisperse and finely controlled crystals, the scale-up of these techniques is not achievable at the present moment. On the other hand, colloidal approaches are scalable, but the precise control is still lacking. Furthermore, the colloidal synthesis is an environment friendly, easy-to-setup and cheap process and it is expected to play a key role in the next future industrial production of nanocrystals. Despite the large number of publications about the nucleation and growth of colloidal nanocrystals presenting experimental data and proposing models[48–53], a lot remains to be done to achieve a comprehensive understanding of the kinetics and of the parameters that control the size and size distribution, especially at the end of the synthesis (i.e. at maximum reaction yield)[54,55].

The cadmium precursors were obtained by mixing cadmium oxide powder 99% and technical oleic acid 90% in 1-octadecene (ODE) technical grade. Because the aim was to study the influence of the oleic acid (OA) and temperature on the synthesis, [Cd]:[OA] ratios from 1:19 to 1:5 were used; the $Cd(OA)_2$ concentrations ranged from 9.5 to 9.9 mM. It is worth noting that an excess of free OA was always present as the stoichiometric ratio is 1:2. The selenium precursor was obtained by the reaction between selenium powder 99.99% and trioctylphospine in 1-octadecene; the selenium concentration was equal to 0.07 M.

The growth temperatures were: 210°C, 235°C, 255°C and 270°C; the last one represents the synthesis upper limit, because beyond this temperature ODE starts to

degrade. The hot injection method[2] was used for the synthesis of CdSe nanoparticles: 10 ml of cadmium precursor were poured into a threeneck flask and heated until the solution temperature reached 225°C under controlled atmosphere. Then, 1 ml of selenium precursor at room temperature was fast injected into the solution and the synthesis started. Other techniques are available for the synthesis of semiconductor nanocrystals (for example the one-pot method), but hot-injection is extremely reliable and provides the ideal conditions to separate nucleation and growth events, a feature for the modelling of the growth mechanism discussed in the following sections. The instrumental setup was the one commonly used for this kind of synthesis under inert atmosphere, Figure 8: the necks of the threeneck flask were occupied by the thermocouple for the temperature control, the in-out argon flux, while the last neck was kept free for the selenium precursor injection and for extracting aliquots of the suspension to monitor the synthesis evolution.

After 60 seconds the first aliquot was extracted: 1 ml of solution was taken with a graduated pipette and poured into a PMMA cuvette containing 2 ml of ODE at room temperature. This operation stops the nanocrystals growth; moreover, the resulting solution has the appropriate concentration for immediate measurement by absorption spectrometry. For each synthesis, aliquots were extracted at 60, 300, 900, 1800, 3000 and 4200 seconds.

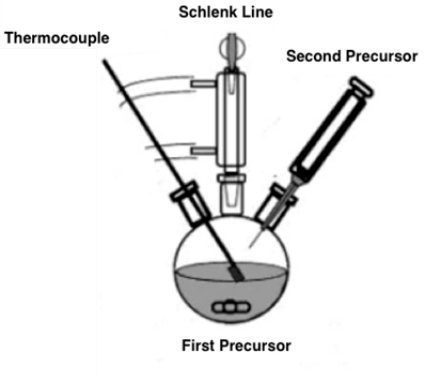

Figure 8 *– experimental setup concept for the synthesis of colloidal NCs.*

Nucleation and Growth

Formation of crystals from a supersaturated solution is an event that can occur only by means of nucleation. The system is not stable in the supersaturated configuration, and

a new solid phase is formed from the solution. The stability of the system is estimated recurring to the Gibbs equation; comparing the energy contribution of two different configurations it is possible to determine the most stable one: the lower the energy, the more stable the configuration will be. In the following sections we will discuss the classical model describing the chemical and physical processes happening during nucleation and growth. Several new ones based on novel approaches have been proposed throughout the years[50,56] to address the complex mechanism of nucleation, but classical nucleation theory (CNT) remains the most common theoretical model to understand the formation of a new phase and it has been confirmed by computer simulations as a perfectly reasonable approximation, for example, for simple hard spherical models[57].

Classic nucleation theory and growth mechanism

For the colloidal synthesis performed in this work, no seeds have been added to the solution (a standard routine for some types of synthesis, especially to obtain complex morphologies and heterostructures[58–61]), thus we will discuss of homogeneous nucleation and not of heterogeneous nucleation. It is worth mentioning that homogeneous nucleation is quite a rare event for natural processes, anyway. The process of homogeneous nuclei formation can be addressed thermodynamically considering the total free energy of the system as sum of the volumetric and the surface terms. The known formulation of Gibbs free energy is the follow

$$G = 4\pi r^2\gamma + \frac{4}{3}\pi r^3\mu$$

Here, G represents the energy required to create a crystal of radius r. γ and μ are, respectively, the surface tension and the specific volume energy contribution of the new phase. This classical formulation provides the change of Gibbs free energy as a function of crystal size, and it establishes a local maximum of the curve known as critical size, r^*, Figure 9. Crystals larger than this value are stable and will grow further, while crystal smaller than the critical size will dissolve. The nucleation activation energy is associated to the critical radius, i.e. $G(r^*)$ or simply G^*. The higher the activation energy, the harder will be for the nucleation process to proceed. The volume term, μ, is usually defined as

$$\mu = \frac{-k_b T ln S}{\upsilon}$$

Where k_b is the Boltzmann constant, T represents the temperature of the system, S is the supersaturation and usually it is interpreted as a fixed value equals to the ratio of initial free monomers concentration and its solubility, υ represents the molar volume. Once defined the starting condition of the system, in terms of concentration and temperature, one can plot the variation of Gibbs free energy as a function of the crystal radius, Figure 9.

The benefit of the hot-injection technique is that the burst addition of precursor promotes crystal fast nucleation. Once stable nuclei are formed, the supersaturation is not high enough to be the driving force for further nucleation, and only the growth process occurs. This assumptions are well represented by La Mer plots[62], Figure 10. Monomers present in solution have to diffuse towards crystal surface, and there they will be adsorbed, contributing to the particles growth[63]. The growth rate can be controlled by one of these two mechanisms: we will refer to either a diffusion-limited growth or a reaction-limited growth[64]. The limiting mechanism influences strongly the final size distribution of the NCs ensemble. In fact, growth rates are different for diffusion-limited and reaction-limited growth, meaning that only the first one provides a focusing effect on the size distribution[63].

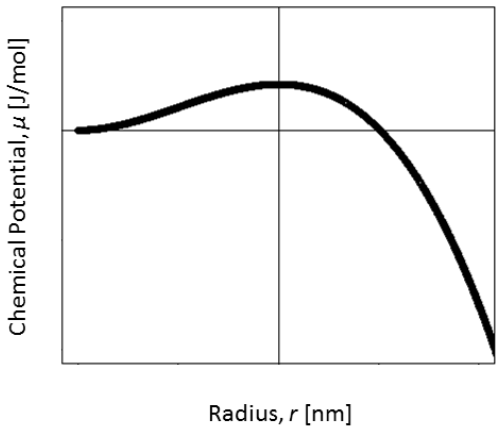

Figure 9 *– Gibbs free energy curve. The critical radius is indicated by the solid vertical line. It represents the minimum nuclei size at nucleation.*

CNT has two main limitations, which are responsible for the development of other theoretical models[65–68] for nucleation. The first one is related to the assumption that

microscopic and nanoscopic nuclei manifest precisely defined properties like their bulky counterpart (e.g. surface tension). It is well known how, at the nanoscale, several material properties diverge strongly from their bulk values; in this sense, it is not clear how surface tension would behave, and, since it represents an important parameter in the determination of the critical radius and nucleation rates, how the quantities estimated by CNT would be affected. The second limitation is related to the concept of equilibrium properties in general: since nucleation is, by definition, a process not at thermodynamic equilibrium, it is not clear how its rates could be defined using equilibrium properties. These two limitations are valid also for the modified thermodynamic model presented in the next section. La Mer model, instead, is based on the separation of the nucleation and growth events. This assumption derives from the nucleation rates, which decreases order of magnitude when the supersaturation is reduced below a certain threshold. The complete stop of nucleation is, actually, impractical, but the approximation of zero nucleation rate has proved valid for several systems.

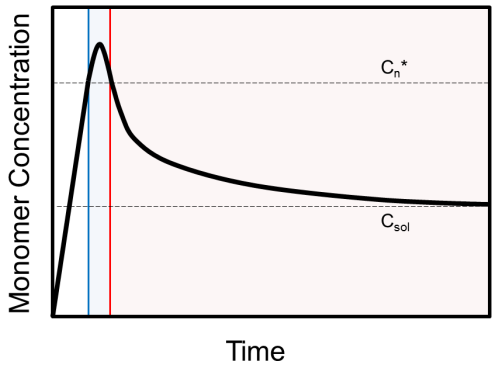

Figure 10 *– La Mer plot. Three region are indicated, each one representing a different regime. In the white region monomers start to form from the mixture of two precursors. As long as the monomer 's concentration stay above a certain critical threshold, C_n^*, nucleation occurs (blue area). Once the concentration drops below the critical value, nucleation will stop and crystal will grow up to solubility concentration C_{sol} (red area).*

Modified thermodynamic model

Gibbs equation, as seen at the beginning of this section, might be a useful tool to theoretically forecast the thermodynamics behind the synthesis of colloidal nanoparticles, in terms of size at equilibrium. However, Gibbs equation, as it was formulated, does not

take into account the change of boundary conditions that occur during the nucleation and growth of crystals. New phase is formed compared to the initial conditions, and freshly-formed interfaces alter the energy balance of the equation. Here we propose a simple modification, expressed as a decrease in the supersaturation term due to the formation of the new phase, which will provide insights on the size of the crystal at the end of the growth step, i.e. when thermodynamic equilibrium is reached. Being able to estimate the final crystal size is a feature of upmost importance since it allows to set-up synthesis conditions aiming to the desired outcome in terms of crystal concentration and size, without relying on previous experimental data, and maximizing the yield of the process. Several kinetic models have been proposed so far, but none has been able to address thoroughly the physics behind nucleation and growth processes, failing to provide general validity. The effort made so far to understand the kinetic and thermodynamic of nucleation and growth processes has provided some notable advancement, but yet none has been able to describe the physics behind these processes. Here, a thermodynamic model, able to evaluate the most stable configuration in terms of crystal mean size of a system where a homogeneous nucleation event occurred, is presented.

As one can easily observed, the Gibbs free energy value keeps decreasing once that the critical radius has been reached, meaning that crystal will growth indefinitely. This is an unlikely scenario for real life nucleation and growth processes. While the new phase is forming, the supersaturation value is modified due to the consumption of free monomers. As each crystal grows, the driving force for the growth of the new phase is diminished, since the solution supersaturation is lowered, up to the point at which the volume contribution is equal to the interface energetic term. For any size larger than this value of equilibrium, the total free energy of the system will increase, indicating a less stable configuration. Graphically, the Gibbs free energy curve present a local maximum related to critical radius for stable nuclei, and an absolute minimum representing the stable crystal maximum size, Figure 11.

To evaluate the change of supersaturation in the solution, we introduce the following equation

$$S(r) = S_0 - \left(\frac{4}{3}\pi r^3\right)\frac{C_{np}}{v_0 C_s}$$

Where $S(r)$ is the actual value of supersaturation for a defined crystal mean radius, S_0 represents the initial supersaturation, C_{np} is the crystal concentration of the new phase, v_0 is the molar volume of the new phase and C_s is the solubility. With this equation, one can see that, increasing crystal radius, the supersaturation value decreases and thus the driving force for further crystal growth is lowered, as theoretically explained before. Combining all these consideration, one can obtain the explicit equation for the modified free energy curve:

$$G = 4\pi r^2\gamma + \frac{4}{3}\pi r^3\left[RTln\left(S_0 - \left(\frac{4}{3}\pi r^3\right)\frac{C_{np}}{v_0 C_s}\right)\right] \qquad (1)$$

This model does not take in consideration the growth mechanism, since it is based on a thermodynamic approach. The point here is that we are able to estimate the final crystal radius at equilibrium, but no consideration about the kinetics (time requested) to reach such size are provided. A similar kind of approach to describe the thermodynamics of crystal formation has been provided by Wasai et al.[67,68]; even if developed in a different way, the two models present similar conceptual considerations and simulated results, supporting the suitability and worthiness of this approach.

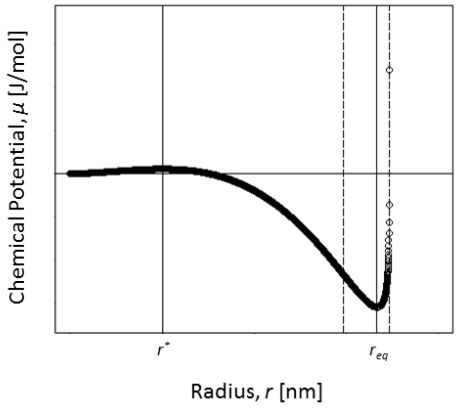

Figure 11 *– modified free energy curve for a closed system. The curve shows a local maximum, associated to the nuclei initial size, and a minimum related to the equilibrium final crystal size. Solid vertical line on the left identifies the critical radius, r^*, while the one on the right indicates the equilibrium size, r_{eq}. Dashed lines intercepts the curve at the inflection point and at asymptotes (left to right).*

Core-shell development and surface passivation

Semiconductor nanocrystals are potential candidates for application in the field of luminescent materials (displays and LEDs) and bio-labelling, and in general as optoelectronic materials, thanks to their tunable properties and their excellent colour purity[69,70]. Due to their intrinsic high surface-to-volume ratio, nanocrystals are extremely reactive to the environment, and several strategies have been developed to improve their photo-chemical stability. One among them relies on the formation of core-shell heterostructure which confines charge carriers within the crystal core; furthermore, overcoating core surface passivates recombination sites, increasing optoelectronic properties[71]. The two best options in terms of materials choice for the development of such structure are CdSe for the core and ZnS for the shell; the first being the prototypical system in the field of semiconductor quantum dots, the second providing a large bandgap, chemically stable protection against the external environment[72]. Yet, lattice mismatch between CdSe and ZnS is large enough to introduce strain and defects on the quantum dots surface[71], decreasing the yield of the emission process and causing crystal distribution broadening while growing ZnS on monodisperse CdSe cores.

SILAR

One of the most common and effective method to growth semiconductor shell on top of semiconductor cores is the successive layer adsorption and reaction (SILAR) technique. It was first developed in 1985 for thin films[73], and later applied for nanoscopic systems[74], as its simplicity and reliability are important advantages compared to other high-temperature and high-pressure techniques. For NCs, the processing is based on successive additions of ionic solutions to the batch. After each addition, half monolayer of shell material is deposited on the surface of NCs; the reaction has to go to completion, otherwise the remaining ionic specimen in solution would react with the oppositely charged ions added during the next step, preventing the formation of a uniform shell and promoting, instead, homogeneous nucleation of pure shell material NCs. Thus, precise estimations of the amount of shell ions to inject are required to avoid incomplete reaction; this represents the main limitation for this technique, since it is not really simple to evaluate the size and the concentration of NCs in solution.

In our experiments, $Cd(OA)_2$ and TOPS precursors have been prepared separately in ODE. Usually, 0.25 μmol of NCs in hexane were poured inside the threeneck flask with 10 ml ODE, kept at 250°C under nitrogen flux. The calculated[24] amount of TOPS precursor was added to the batch drop-by-drop, leaving the system react for 10 minutes after the completed injection. After this time, the Cd precursor has been added with the same procedure. We performed SILAR growth up to 3 complete CdS monolayers on top of CdSe NCs. After the deposition, the samples have been washed with methanol and acetone, precipitated and dispersed in fresh hexane.

Colloidal-Atomic Layer Deposition†

The standard solution-based technique to create core-shell structures is based on successive ion layer absorption and reaction method[74]; it is a well-established process, developed for thin films, already performed on semiconductor quantum-dots systems based on CdSe-CdS[74], CdSe-CdS-ZnS[75], CdS-ZnS[76], and others. In the last decade, other routes have been proposed, but all rely on high temperature processing[19,77]. Colloidal Atomic Layer Deposition (c-ALD) is a new technique to create colloidal heterostructures by self-limiting reactions on the surface. It was first introduced by Ithurria and Talapin[78], and it has been already applied, for example, to the development of Mn^{2+}-doped CdSs/CdS core/multishell quantum wells[79] or high performance PbSe crystals[80]. The technique is based on half-reactions of a binary compound via phase transfer and it was performed so far mainly on CdSe cores to grow CdS multilayer shell. It has several advantages compared to the standard high temperature SILAR technique, first of all the benefit of not requiring precise calculation over the amount of precursor to inject: large amount can be used during c-ALD since after each half-reaction the solution in washed and the precursor excess removed. Secondly, c-ALD is performed at room temperature and in air, making the process easy to automate and control. At last, c-ALD provides a precise control over the crystal surface composition, a strict requirement to obtain high photoluminescence efficiencies[81,82]. Even with such convincing benefits, c-ALD validity has not been investigated thoroughly: so far, usually combinations of CdSe and CdS have been reported[78,83], with few execptions[80,84]. We have decided to investigate possible alternative combinations of materials to improve the control of surface chemistry at the nanoscale,

† This section is largely based on our work in ref [102]

introducing ZnS as shelling material and investigating the potential of c-ALD on metal core systems, using Au-CdS as prototypical example. The development of complex core-shell structure has no immediate relation with the main objectives of the intermediate band material project proposed in this thesis, but it is a research line we followed since its study can provide useful insight about the surface chemistry of colloidal nanocrystals for all applications.

Semiconductor quantum dots doping is a common but, at the nanoscale, not yet well-established procedure to enhance their functional properties. Impurity doping, in which atoms are added to the bulky material, have been extensively investigated only in the case of isovalent atoms, like Co and Mn[85], or in the heavy doping regime[86]; a lack of knowledge is still present if we consider nanocrystals with additional carriers in the light doping limit, meaning only few metal atoms per quantum dot. The aim of impurity doping is to provide charge carriers to the host material, improving optoelectronic properties of an intrinsically not conductive material. However beneficial for their properties, it is not easy to finely control light impurity doping at the nanoscale, dealing with few dopants per nanocrystal. In our particular case, we introduced a doping step during c-ALD processing, based on what reported by Sahu et al.[87] for Ag doping on CdSe nanocrystals. This investigation will be useful considering the constrains required for an intermediate band material development, main goal of the project.

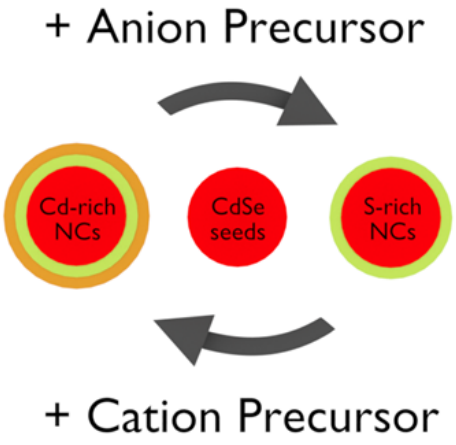

Figure 12 *– a conceptual representation of the sequential addition of shell half monolayer process, in the specific case with cadmium and sulphur.*

CdSe cores have been synthesized by hot injection process in organic media: 90 mg CdO, 0.5 ml oleic acid and 8.5 ml ODE are mixed together in a 25 ml threeneck flask at 150°C for 1h and then temperature is increased to 250°C; once stable, 1 ml TOPSe 1.6M solution is injected. Crystals are allowed to grow for 60 seconds, then solution is quenched. These QDs (3.3 nm diameter) have been used for the development of CdSe-CdS(4ML) and CdSe-CdS(1ML)-ZnS(1ML)-CdS(1ML)-ZnS(1ML) systems. An alternative route used to synthesize CdSe seeds was taken from Carbone[19], recurring to cadmium oxide, octadecylphosphonic acid (ODPA), hexylphosphonic acid (HPA) and trioctylphosphine oxide (TOPO) for the first precursor. Once solution is ready, a mixture of tricotylphosphine (TOP) and selenium powder is injected at 330°C; crystals are allowed to grow for 10 minutes (3.1 nm crystal mean size). These cores have been applied for CdSe-ZnS(4ML), CdSe-ZnS(1ML)-CdS(3ML), CdSe-CdS(3ML)-ZnS(1ML), CdSe-CdS(2ML)-ZnS(1ML)-CdS(1ML). After both syntheses, solutions were washed twice with methanol and acetone and dispersed in toluene.

CdSe quantum dots have been used as seeds to develop dots in rods structures, based on Carbone's recipe[19], where 0.06 g CdO, 0.29 g ODPA, 0.08 g HPA and 3 g TOPO are mixed together at 150°C for 1h and then heated up to 350°C. First 1.8 ml TOP and then a solution of 1.8 ml TOP, 0.12 s sulphur powder and 200 µl CdSe seeds solution (size=3.3 nm, concentration=400 µM) are injected. Solution is quenched after 8 minutes since final injection, and resulting rods have 19x5 nm size.

Colloidal atomic-layer-deposition procedure follows the one proposed by Talapin[78]. Cd, Zn and S precursors (all 0.5M) have been prepared mixing Cd-acetate, Zn-acetate and Na_2S in n-methylformamide (MFA) solution. Quantum dots in organic media are mixed with a fixed amount of sulphur precursor inside a 1.5 ml plastic tube. After few seconds phase transfer occurs and NCs become stable in the polar solvent; S^{2-} terminated particles show no emission under UV excitation. Solution was washed twice with hexane and acetone, centrifuged and dispersed in new MFA. Then, cation precursor solution is added and solution is vigorously shacked for 1 min to let surface reaction occur. Once precursor has reacted with particles, the solution is washed again, centrifuged and crystals are dispersed in new MFA. After these two steps, one full monolayer of CdS or ZnS has grown on top of quantum dots seeds. This procedure can be repeated as long as needed. Doping

process is based on the paper by Sahu[87] with some modifications: it has been performed simply adding the Ag-nitrate ethanolic solution to the cadmium precursor in MFA during the first monolayer growth via c-ALD. After the doping, one undoped monolayer is added so that silver atoms are shallowed beneath the crystal surface.

Phase transfer of nanocrystals to polar or nonpolar media

After the shell growth by SILAR, hydrocarbon long-chain molecules are bounded on NCs surface, which stabilize them in organic media. This capping layer would represent an obstacle for the successive self-assembly of the crystals, especially in terms of functional properties. Organic compound shells hinder the electron transfer from one NCs toward the neighbours, suppressing any electric conduction properties the structure may possess. Several routes are available to get rid of this issue, but all of them are based on the ligand-exchange process. The idea at the basis of ligand-exchange is to substitute insulating long-chain ligands with either conductive inorganic[88,89] or short organic ones[90,91]. In the first case, electron transfer is promoted as ligands are preferential paths able to dislocate charge on their molecular structure, in the second option the spatial separation from one crystal to the others is sensibly reduced, so electrons can hop from one NCs to another. After a first implementation of mercaptopropionic acid (MPA) as new ligand to stabilize NCs in water, a strategy already investigated by Cozzarini[47], new stabilization routes have been studied. The most promising system consists on the ligand-exchange by means of sodium sulphide, chosen on the experience of colloidal Atomic Layer Deposition described previously. It is worth mentioning that, even changing long-chain organic compounds with new conductive or short ligands, during the self-assembly process these molecules would remain attached on the surface of NCs, representing impurities for the assembled film and preferential centres for non-radiative recombination. Pyrolysis of these compounds would produce new defects with unspecified composition, increasing the degree of uncertainty related to the structure. These considerations are at the basis of our decision to stabilize NCs in polar media using ligands that can be embedded within the shell structure. In fact, sulphur ions on the crystal surface represent one additional half monolayer of CdS shell,

maintaining compositional coherency, and the sodium counterions in solution can act as p-type dopants of the barrier material once the shell has been sintered.

Aliquots of core-shell NCs in hexane have been mixed with large excess of sodium sulphide (1000x times the amount of surface sites) in methylformamide. The transfer from non-polar to polar media happened within few seconds. Crystals have been, then, centrifuged and precipitated using hexane and acetone, and finally redispersed in fresh MFA. This protocol is exactly the same used to deposit half monolayer during c-ALD from previous section.

Deposition of colloidal solution

The stable NCs solution was deposited on glass substrate in order to obtain thin films. Among the several deposition methods available, drop casting has been selected over spin-coating for two main reasons: the amount of wasted material during spinning would have been a serious issues since the synthesized NCs solution volume was limited, and there was no strict requirement for uniformity of deposited film. N-methylformamide is a high boiling point solvent, and its complete spontaneous evaporation could require long time. To address this limitation, substrates with drop-casted solution have been placed inside a vacuum chamber in order to promote fast controlled evaporation. No heating has been applied to avoid any possible event of annealing or sintering, which would have reduced sensibly the repeatability of the process.

Microscope glass have been cleaned with acetone and isopropanol during sonication. Slides have been cut in small rectangular substrates with size 0.5x0.2 cm^2. Two drops of 4.9 μM NCs in MFA solution have been deposited on the substrates, then samples have been placed inside the vacuum chamber connected with a water pump. Evaporation occurred during the following two days. Once films were completely dried, they have been inserted inside glass tubes. Before sealing, nitrogen flux flowed inside the tubes to remove oxygen and avoid oxidation during the following thermal treatment.

Thermal treatment and sintering of nanostructure

The deposition of core-shell NCs on substrates and their subsequent self-assembly is not enough to provide the morphological homogeneity needed for an intermediate material to work properly. A continuous CdS matrix is required to provide the necessary carriers mobility within the structure. One way to address this task is to sinter the shell material with a thermal treatment. Films inside glass tubes have been annealed at different temperatures: the treatment lasted from 2 up to 128 minutes, and temperature ranged from 300°C to 550°C. Higher temperature are not favourable due to softening of the glass tube walls with potential crack and leakage of the inert gas, resulting in contamination. Once reached the treatment time, samples have been removed from the oven and let cool down in air.

Characterization Techniques

Absorption spectra of NCs in solution (core and core-shell) and of as-deposited films have been collected by UV/VIS Perkin Elmer Lambda Bio 20 spectrophotometer. We also obtained the emission spectra using an Ocean Optics® SpectraSuite spectrometer and a UV LED excitation source at 310 nm. Crystal size has been evaluated with the formula by Jasieniak[92]. Quantum Yield (QY) measurements have been performed by comparison with Rhodamine101 e Rhodamine6G. Films have been characterised morphologically by XRD using a Bruker-AXS D5005 diffractometer with a 2.2 kW Cu source. Raman spectroscopy (fluorescence mode) was performed to evaluate photoluminescence of sintered films, while a source laser at 633 nm was used for below-band gap photoexcitation.

Results and Discussion

CdSe core synthesis

The particle mean size has been calculated according to the method first proposed by Yu[93] and later modified by Jasieniak[92], based on the position of the first absorption peak; the full width at half maximum (hereafter FWHM) of the PL emission peak has been considered here as a measure of the particle size dispersion. In Figure 13 the time evolution of size and size distribution is shown for a representative case. The general trend is in good agreement with previous findings reported in the literature[49]: as for the particle size, we observe a continuous growth, initially very rapid and then smoothly slowing down; as for the size distribution, we observe a very rapid decrease of the FWHM, i.e. a sharp focussing, followed by a plateaux – in agreement with Peng[94].

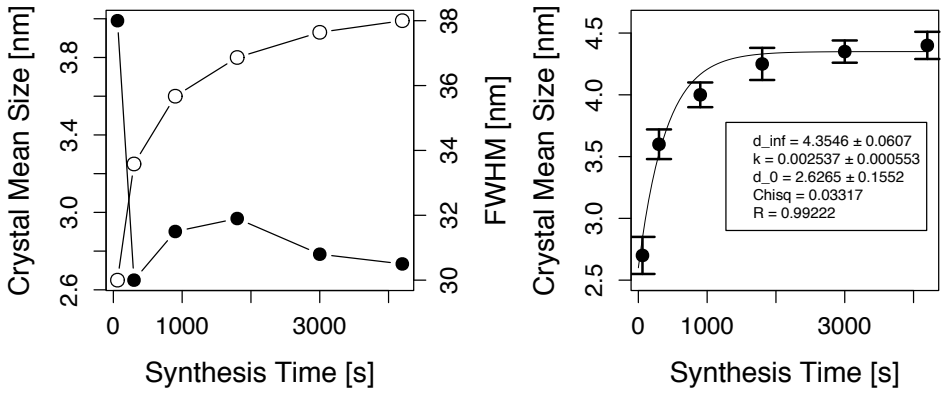

Figure 13 *– (left) time evolution of particle size and particle dispersion for a representative synthesis ([Cd]:[OA]=1:10, T=235°C). (right) fitting of crystal size evolution. The solid line is the best fit according to Equation 2, with parameters indicated in the box.*

Kinetics of synthesis

Evolution of size distribution

Under most synthesis conditions, as shown in Figure 14 for a growth temperature of 270°C, the size dispersion increases after about 3000 seconds, suggesting the onset of Ostwald ripening – whereby the larger particles grow at the expense of smaller ones. In view of most applications, it is desirable to avoid size distribution broadening in order to maintain a sharp size distribution. Therefore, in this contribution we focus our attention on the synthesis characteristics before the onset of Ostwald ripening – e.g. on the data obtained up to 3000 s for all the syntheses conducted at 270°C.

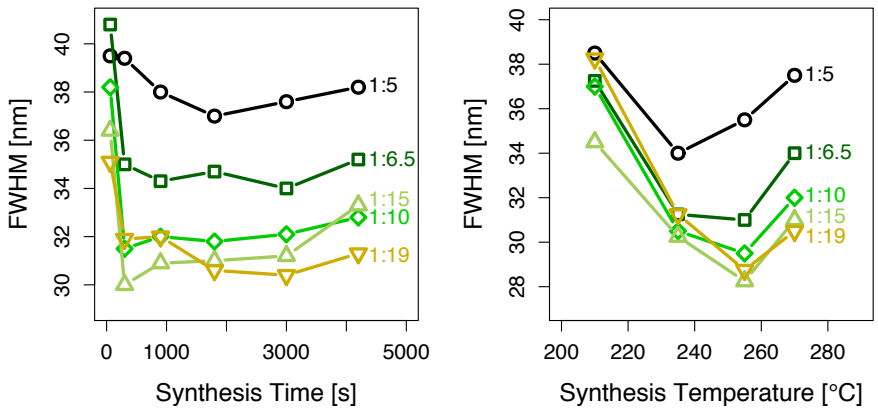

Figure 14 *– evolution of the FWHM over time for the representative case of the synthesis at 270°C and variable [Cd]:[OA] ratio. FWHM of the PL spectrum at the end of the growth stage, as a function of temperature and [Cd]:[OA] concentration ratio.*

Figure 14 also shows a clear trend for the size dispersion as a function of the [Cd]:[OA] ratio: the higher the ratio, the higher the dispersion. This can be explained considering that OA acts as capping agent for the nanocrystals, and influences the surface energy. More OA better passivates the particles, lowering the surface tension of the solid phase. As expected based on the modelling carried out by van Embden et al.[64], a reduction of the surface tension is expected to lead to an improvement of the crystal size uniformity, consistent with our observations. The influence of the OA is well revealed in Figure 14, where the size dispersion at the end of the growth stage (before the onset of the Ostwald

ripening) is represented as a function of temperature and [Cd]:[OA] ratio. The FWHM shows a non-monotonic trend, with a minimum at around 250°C. While a temperature increase is indeed expected to contribute to a smaller size dispersion[64], no explanation can be given at this time for the opposite trend observed at higher temperatures.

Evolution of size

Several models have been proposed to explain the colloidal synthesis of semiconductor nanoparticles from a physicochemical standpoint[49,53,95]. In this text, however, we mainly focus on the description of the growth kinetics rather than on the underlying physical and chemical mechanisms, and therefore we adopt a rather general functional form for fitting the particle size data, d, obtained for the growth stage kinetics, as exemplified in Figure 13:

$$d(t) = d_\infty \left[1 - \frac{d_\infty - d_0}{d_\infty} exp(-kt)\right] \qquad (2)$$

The parameters d_0, d_∞ and k represent the key features of the growth stage: d_0 represents the initial size of the nanoparticles at the early stages of growth (rigorously, from the equation, when $t = 0$); d_∞ is the size of nanoparticles at the end of the growth stage, before the onset of the Ostwald ripening; k is the growth rate, describing how fast the nanoparticle size approaches the final size d_∞; t is the time.

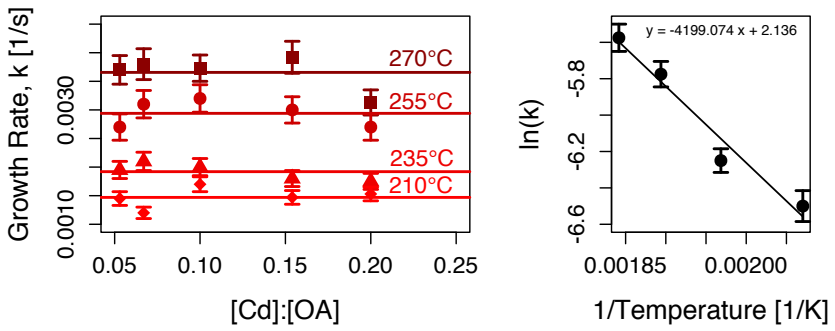

Figure 15 *– (left) kinetic parameter, k, as a function of the cadmium-to-OA ratio. (right) Arrhenius plot with equation of the linear fitting.*

A similarity with the classic Avrami-Johnson-Mehl-Kolmogorov (AJMK) equation can be noted: in fact, although initially derived for describing transformation in solids[96,97], the AJMK has a rather general validity in describing kinetic and statistical phenomena and has previously been used to study solid-state nucleation processes[48]. The AJMK function was modified here in order to account for the essentially instantaneous nucleation occurring in the QD synthesis, reflecting the assumption that the size of the nanoparticles, at the beginning of the growth stage, is finite – i.e. larger than zero[63,98].

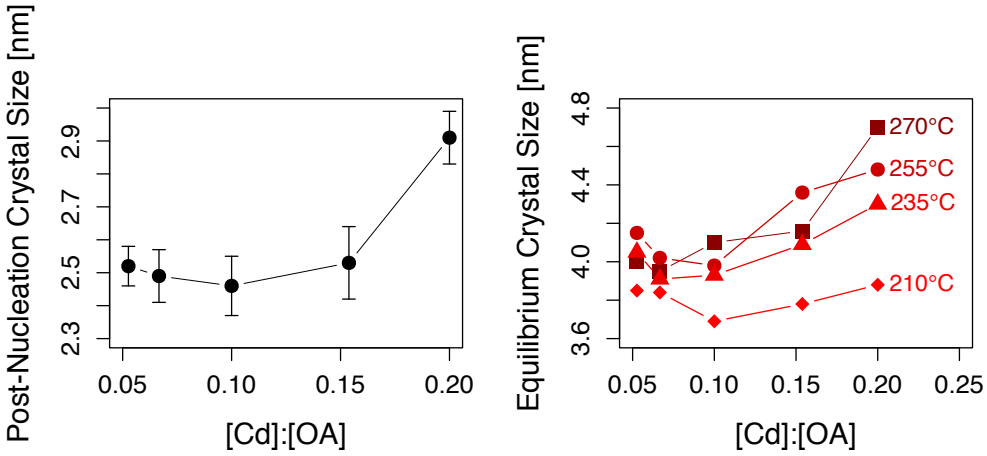

Figure 16 *– left: size at the end of the nucleation stage, d_0, as a function of the [Cd]:[OA] ratio. The mean values for each ratio at different temperature are taken since no dependence on the growth temperature is expected, as the nucleation temperature was set equal for all syntheses. Right: "equilibrium size map", nanoparticle size at the end of the growth stage, d_∞, as a function of temperature and [Cd]:[OA] ratio.*

The analysis of the particle size evolution over time through the use of Equation 2 reveals some interesting aspects of the growth kinetics. As shown in Figure 15, the growth rate, k, shows essentially no dependence on the [Cd]:[OA] ratio. On the other hand, k strongly depends on temperature. The temperature dependence of k follows the typical Arrhenius law for thermally activated mechanisms, with activation energy of about 0.43 eV/molecule – a value in agreement with the estimations of Dickerson et al.[99] in the case of CdSe organometallic syntheses.

In Figure 16 we report the value of d_0, i.e. the size of nanoparticles at the early stages of growth. Since it is extremely difficult to perform experimental measurements of post-nucleation crystals size due to very fast kinetics of II-VI semiconductor colloidal synthesis in its first stages, one option is to introduce an analytical model which estimates such

figures, as we did recurring to Equation (2). While there is no meaningful influence of the [Cd]:[OA] ratio on d_0 for values up to about 0.15, larger values lead to a marked increase of d_0. A possible explanation for this observation can be given in light of the CdSe solubility: an increase of the OA concentration induces a higher solubility of monomers, corresponding to an inhibition of the crystal growth, which starts at the very early stages of the synthesis, thus affecting both concentration and size of the nuclei[49].

The final particle size before the onset of Ostwald ripening, d_∞, is reported in Figure 16. Higher growth temperatures lead to a larger final size, as expected for a thermally activated process. At the lowest temperature of 210°C there is essentially no dependence on the OA concentration, while at higher temperatures d_∞ is observed to increase for [Cd]:[OA] ratios larger than 0.1. This is expected, as the OA hinders particle growth – as previously noted and in accordance with the findings on similar systems[100], where high contents of OA are shown to cause fast termination of the growth stage, thus keeping the particles small. The similarity of the trends for d_0 and d_∞ is remarkable, supporting the idea that nucleation has a fundamental influence, in terms of final crystal size, in hot-injection synthesis of II-VI semiconductor materials[64]. The yield of the synthesis can be evaluated using crystal final size and crystal concentration: in our experiments, yield was always above 85%. In some cases, the evaluation of the converted CdSe amount exceeded the total precursor amount, indicating that a precise value of the yield cannot be estimated due to the errors associated in the evaluation of crystal concentration and mean size. Anyway, this quick analysis suggests that the colloidal synthesis of CdSe nanocrystals presents very high conversion values.

Remarkably, while on the one hand we find that the growth rate does not depend on the OA concentration, in agreement with the work of Abe et al.[54], on the other hand we observe a trend for the dependence of the equilibrium size on the OA concentration that is less marked and opposite to that reported by these Authors.

To understand this, we first note that in all these experiments a large excess of OA is used, with the consequence that the [Cd]:[OA] ratio can be considered as an indication of the concentration of free OA, rather that the OA bonded to the nanoparticles. Then, we observe that Abe and coworkers' syntheses were run with a large excess of selenium, i.e. with cadmium as the limiting reagent. As the concentration of OA strongly affects the concentration of the cadmium precursor, and the latter, in turn, favours a larger final particle size, a strong and positive correlation between OA concentration and final particle size is expected.

Conversely, in this work, the limiting reagent is selenium. However, the selenium precursor's concentration is hardly affected by the OA concentration, so no or little correlation would be expected in our case between the latter and the final particle size. Indeed, we observe a rather mild dependence, which is most likely dominated by the size of the particles at the initial growth stage, d_0.

Thermodynamic model

The modified free energy equation (1) has been implemented inside a R-script and run within the RStudio® software environment. The full code can be found at the end of this document, in Appendix A. The simulations are confronted in three different case studies to assess the quality of the proposed model. The first case is based on the kinetic parameters discussed in the previous section, and developed in our facilites. The second and the third cases, instead, are based on experimental observations of high-impact papers. The proposed model present a good agreement with the experimental and literature data, indicating the consistency of the concept and underlining the importance of crystal concentration (and, again, of the nucleation stage), most likely the most important parameter which actually influences and determines the final crystal size.

Radius at full yield (in-house data)

We collected a series of kinetic data about semiconductor quantum dots colloidal synthesis to compare the experimental final size with the model forecast. The modified free energy equation does not present any bias regarding our experimental data, since it has been developed independently. The only parameter needed from experimental data was the crystal concentration, since, there is no established kinetic model capable to evaluate a priori the total amount of crystal formed during synthesis, yet. Crystal concentration has been evaluated by means of absorption peak intensity and peak FWHM, recurring to the formula proposed by Jasieniak[92]. The colloidal synthesis of quantum dots presents an extremely fast growth during the first stage of the reaction, followed by a slow approaching to the equilibrium final size (Figure 13); experimental points represent crystal sizes close to the kinetic plateaux, when the free monomers in solution have reacted almost completely and before the occurrence of other aging or coalescence processes. Figure 17

summarizes the results for the four temperature series we performed, indicating a general good agreement between experimental and simulated values. All simulations have been performed with parameters reported in Table 1, where surface tension and solubility have been found in Abe[55].

Table 1 *– parameters used for simulation with Equation (1). Three main groups are presented, related to the case studies. In each group, series are labelled with the ratios between cadmium-to-ligand concentrations (mainly oleic acid, only for van Embden TMPPA). The NCs concentration, Cnp, has been estimated from absorption spectra for our data, and from published work for Abe[54,55] and van Embden[101] cases. Surface tension and solubility are reported as found in literature. Temperature is referred to growth temperature, while C0 indicates the initial monomer concentration. Last two columns present simulated and experimental crystal size values, respectively.*

Case	*System ID*	*Cnp [μM]*	*C0 [mM]*	*Csol [nM]*	*Surface Tension [N/m]*	*Temperature [K]*	*R_sim [nm]*	*R_exp [nm]*
Our data	OA19	9.1	6.3	0.02	0.2	483	2.04	2.03
	OA15	9.3	6.3	0.02	0.2	483	2.03	1.955
	OA10	13	6.3	0.02	0.2	483	1.81	1.875
	OA6.5	11	6.3	0.02	0.2	483	1.92	1.94
	OA5	8.9	6.3	0.02	0.2	483	2.06	1.975
	OA19	8	6.3	0.02	0.2	508	2.13	2.055
	OA15	10.4	6.3	0.02	0.2	508	1.95	1.99
	OA10	8.2	6.3	0.02	0.2	508	2.11	2
	OA6.5	6.3	6.3	0.02	0.2	508	2.31	2.09
	OA5	---	6.3	0.02	0.2	508	---	---
	OA19	9.9	6.3	0.02	0.2	528	1.98	2.09
	OA15	8.1	6.3	0.02	0.2	528	2.12	2.04
	OA10	8	6.3	0.02	0.2	528	2.13	2.01
	OA6.5	5	6.3	0.02	0.2	528	2.49	2.22
	OA5	5.7	6.3	0.02	0.2	528	2.39	2.275
	OA19	7.7	6.3	0.02	0.2	543	2.16	2.03
	OA15	9.9	6.3	0.02	0.2	543	1.98	2.005
	OA10	7	6.3	0.02	0.2	543	2.23	2.08
	OA6.5	6.8	6.3	0.02	0.2	543	2.25	2.115
	OA5	5.5	6.3	0.02	0.2	543	2.42	2.365
Abe	OA64	12.5	17	0.02	0.2	503	2.56	2.55
	OA32	26	17	0.02	0.2	503	2.01	2
	OA16	39	17	0.02	0.2	503	1.75	1.85
	OA8	47.5	17	0.02	0.2	503	1.64	1.65

	OA4	57.5	17	0.02	0.2	503	1.54	1.55
van Embden	OA20	32	16	0.02	0.2	503	1.83	1.865
	OA14	47	16	0.02	0.2	503	1.61	1.685
	OA11	53	16	0.02	0.2	503	1.55	1.61
	OA8.5	56	16	0.02	0.2	503	1.52	1.55
	OA5.5	58	16	0.02	0.2	503	1.5	1.5
	TMPPA3.5	49	26	0.02	0.2	503	1.87	1.85
	TMPPA2	36	27	0.02	0.2	503	2.1	2
	TMPPA1.5	25	29	0.02	0.2	503	2.43	2.25
	TMPPA0	15	31	0.02	0.2	503	2.96	2.8

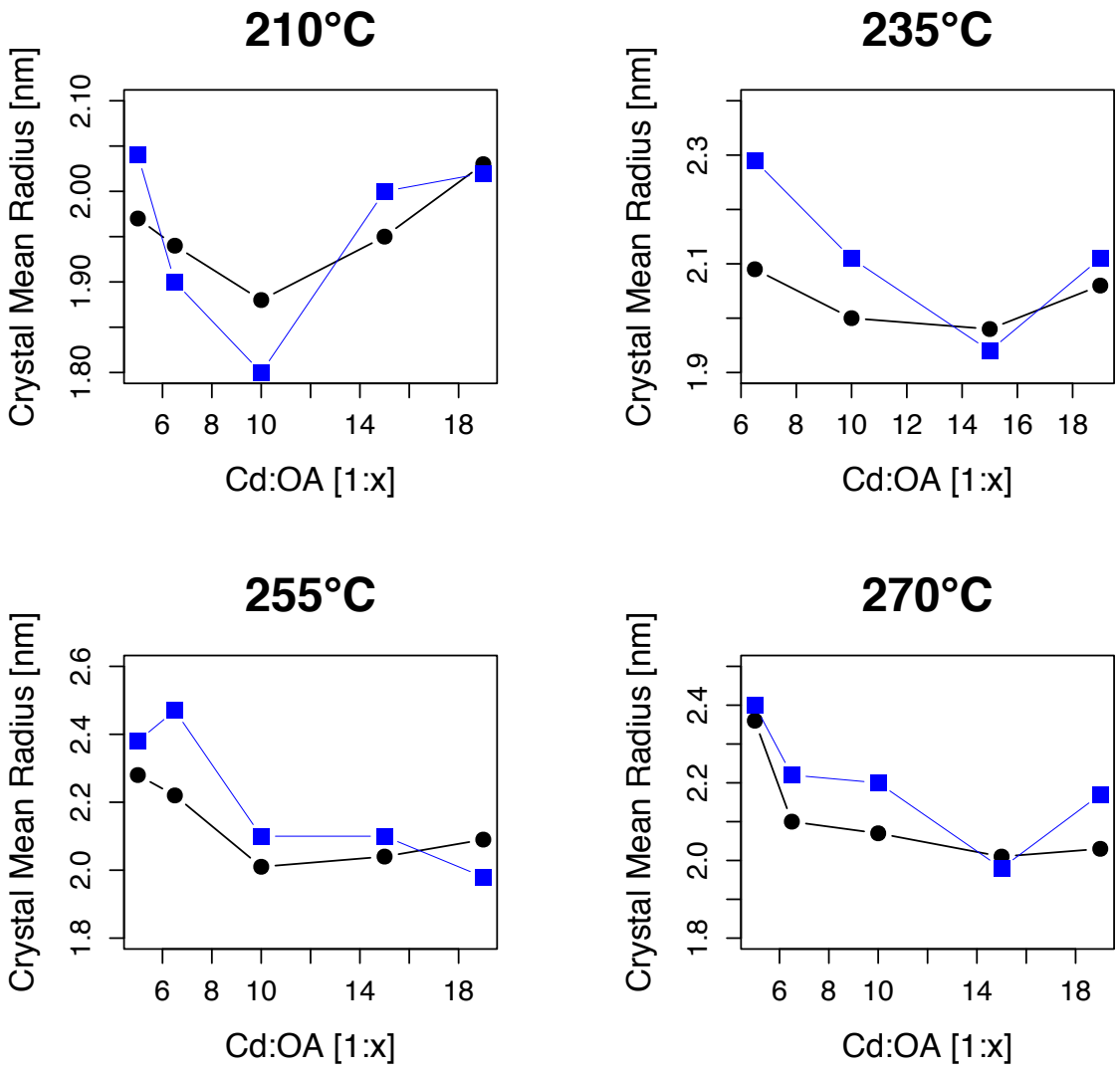

Figure 17 *– comparison of experimental (black dots) and simulated (blue squares) growth values for our dataset. The maximum mismatch, as observed in the series 255°C, is 12%.*

Radius at full yield (Abe's data)

There are just few examples of quantum dots synthesis carried out at the maximum yield condition, one of the most prominent example is Abe et al. work[54,55], in which they studied the influence that oleic acid, a stabilizer for the crystals, has on crystal final size. Literature data can be used as input for our model, exactly the same way we used our experimental data: crystal concentration, temperature and initial monomer concentration are the parameters to define to obtain a forecast of the crystal equilibrium radius. The results are reported in Figure 18.

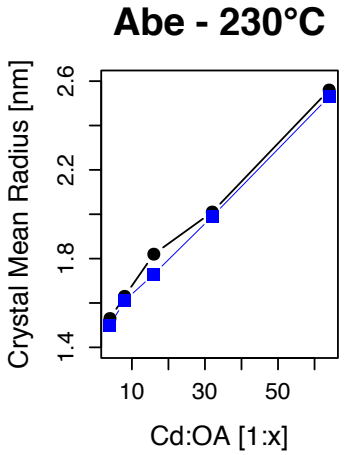

Figure 18 *– crystal mean size as a function of oleic acid amount during synthesis. Black dots are experimental point from Abe et al., blue squares are simulated value. The agreement for this series is extremely good, with one exception at the x-value 16.*

Radius at full yield (Mulvaney's data)

We performed another case study with experimental data from van Embden and Mulvaney[101]. In their contribution, they reported kinetic parameters for two different synthesized systems: one with bis-(2,2,4-trimethylpentyl)phosphinic acid (TMPPA) and one with oleic acid. For the OA synthesis, as indicated by their results, over 1000 seconds growth time the NCs size curve switch concavity, indicating the onset of Ostwald ripening. We thus took as input for our analysis the first value before 1000 seconds synthesis time.

Limitations of the study

The mismatching between experimental and simulated values can be interpreted in several ways. First of all, for the reason that the model estimates the equilibrium size, it is not certain that the experimental samples have been collected exactly at that point, since it is very hard to control the growth kinetic during the synthesis. A too long synthesis would produce coalesced and polydisperse NCs, as Ostwald ripening and other aging mechanisms would set in. Stopping the synthesis too early may produce crystals not at equilibrium, i.e. with a large amount of monomers not yet reacted. These considerations indicate clearly that it is not easy to control the synthesis kinetic and quench the solution when the equilibrium size is reached, because there is not explicit evidence about such condition. Furthermore, crystal mean size has been measured indirectly, by means of spectroscopy – a well-established characterisation technique for semiconductor nanocrystals. An error is associated to the calibration curve which relates absorbance spectra and mean size; of course its magnitude is not enough to compensate large mismatches, but it is a factor to take in consideration. Related to this point, crystal concentration is measured from absorbance intensity; again, the uncertainties associated to this method are quite important. Crystal shape could be a further issue: while most of the standard syntheses of semiconductor quantum dots produce spherical crystals, this could not be valid for other systems. A scaling factor should be introduced in the model to take into account different morphologies.

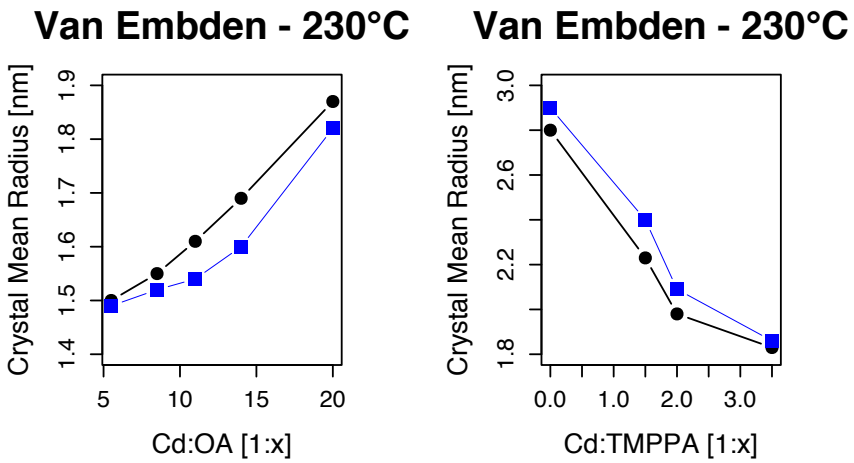

Figure 19 *– experimental and simulated values (black dots and blue squares respectively) for the growth of CdSe nanocrystals in organic media using TMPPA or OA as ligand.*

Future development

The model does not consider, yet, some concept being significant at the nanoscale. The Gibbs-Thomson equation, which relates vapour pressure with crystal curvature. Practically, it indicates a variation of the chemical potential across a curved surface. This physical contribution has been taken into consideration by Wasai[67,68], for example, in his derivation for the modification of the Gibbs energy curve.

One further limitation of the proposed model is that it makes use of specific parameters for the system considered (in our case cadmium selenide nanocrystals). Such values are not always available or precise for bulk materials, so the applicability and the accuracy at the nanoscale, where these values can change even by order of magnitude, is limited. Nonetheless, the main limitation of the model as proposed here is that it relies on the crystal concentration as input for the estimation of the equilibrium size. This value was obtained by experimental data, but to unleash the forecast power of the model, a way to estimate the crystal concentration a priori is requested.

To address the limitation of crystal concentration as input parameter of the model, we analysed published experimental data[49,55,101] in order to figure out a potential correlation with the amount of oleic acid for the synthesis of CdSe in organic media. Values of crystal concentration has been normalized on the initial precursor concentration to deal with different synthesis conditions, with the hypothesis that increasing monomer concentration would increase the number of nuclei but not their final size, keeping constant the other conditions. Results are reported in Figure 20, where data have been represented as a function of the oleic acid-to-Cd ratio and each series have a different temperature. The nucleation rate equation is expressed by an exponential function, where A is the pre-exponential factor, γ represents the surface energy, v_0 the molar volume, k_b Boltzmann constant, T is temperature and S supersaturation.

$$J_{nc} = A\ exp\left(\frac{16\pi\gamma^3 v_0^2}{3k_b^3 T^3 (lnS)^2}\right)$$

Nucleation rate and time determine the total number of nuclei formed during nucleation; it is expected that the same trend with oleic acid-to-cadmium is common to both nucleation rate and total nuclei concentration. The largest effect on rate comes from supersaturation and surface energy; we can suppose it keeps valid for the total number of

nuclei[50]. While surface energy is not largely affected since its variation is caused by different surfactants, supersaturation is the most important factor. Oleic acid and temperature decrease supersaturation, because they increase the solubility concentration, and therefore a decrease in the total number of crystal is expected, as shown in Figure 20. Temperature and oleic acid concentration influence the exponential argument, increasing its numerical value. With this fitting it is clear that, to obtain the maximum nuclei concentration attainable, one should work at low contents of oleic acid, and, in first approximation, at high temperature. The theoretical formulation of the exponential argument can be subdivided into three different contributions, as following:

$$\frac{16\pi\gamma^3 v_0^2}{3k_b^3 T^3 (lnS)^2} \rightarrow f(OA)\ g(T)\ h(C_0)$$

From here, we can analyse how series fits in the theoretical model and how the system behaves with variation of parameters. The initial monomer concentration affects the supersaturation, and increasing it would produce a decrease in the exponential argument, resulting in a slower nucleation rate and less final nuclei formed. Temperature is the second factor affecting the argument: based on experimental data, it has the effect of reducing nucleation rate. Finally, oleic acid promotes a smaller number of crystals. While the mechanisms behind nucleation step are still under discussion, this analysis can provide a first approximated estimation on the amount of crystal formed in the first stages of II-IV semiconductor hot-injection synthesis.

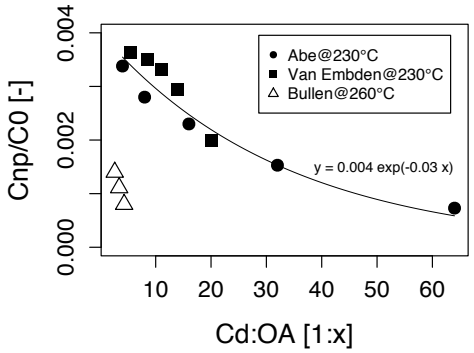

Figure 20 *– Experimental data as found in ref [49,55,101] for crystal concentration, temperature, monomer concentration and growth temperature. Abe and van Embden series, presenting the same synthesis temperature, also show a good agreement in terms of nuclei concentration-to-monomer concentration ratio. Temperature has the effect of lowering the amount of crystal formed, as oleic acid does.*

Core-shell systems

Silar technique

Nanocrystals after CdS shell deposition nanocrystals have been characterised optically and morphologically. UV-Vis absorption and emission spectra indicate the redshift of the first transition peak due to delocalisation of the electron in the structure. Absorption spectrum presents a less defined peak (almost impossible to estimate the centre without recurring to derivative analysis) and, below 500 nm, an intense absorption related to the CdS shell. From optical spectra, core size was estimated to be 3.3 nm, while with TEM image analysis mean size was estimated to be 3.52 nm and standard deviation 1.18. Intensity of PL peak increased after the shelling process, as suggested from the reduced signal-to-noise ratio in Figure 21 (normalized data is shown), preserving the integrity and the properties of NCs.

Semiconductor-semiconductor systems by c-ALD‡

CdSe NCs with sizes of 3.3 nm and 3.8 nm were used as starting cores to synthesize core-shell heterostructured materials with a variable alternation of CdS and ZnS layers having a total shell thicknesses of 4 MLs (Figure 22). Particularly, CdSe/CdS4, CdSe/CdS2/ZnS2 and CdSe/CdS/ZnS/CdS/ZnS structures were synthesized from 3.3 nm sized CdSe NCs, while larger 3.8 nm CdSe cores were used to deposit shell layers with the formulations of CdSe/CdS3/ZnS, CdSe/ZnS/CdS3, CdSe/ZnS4 and CdSe/CdS2/ZnS/CdS. As follows from the band energy diagrams presented in Figure 22, by combining in one shell CdS and ZnS layers one can play with the band-gap alignment within the resulting core/multishell heterostructures. Thus, by covering CdSe core with either CdS or ZnS shells, the Type I heterostrucure will be formed, where the band gap of the core is locked within the band gap of the shell semiconductor, confining the charge carriers inside the core. Furthermore, we can control the extent of quantum confinement by choosing a proper

‡ This section and the following one are largely based on our work in ref [102]

pair of semiconductors, i.e. compounds with the desired band alignment. For example, in the case of CdSe/CdS structure, hole is expected to be localized mainly in the core, whereas the electron wave function can be extended to the shell (partly delocalized) owing to a small energetic threshold between conduction bands of CdSe and CdS. Unlike in this configuration, in CdSe/ZnS heterostructure both charge carriers should be mainly confined in the core due to relatively large energy barriers imposed by ZnS shell depending on its thickness. Moreover, introduction of the CdS layers between ZnS ones can yield quantum well structure in which the larger band-gap semiconductor forms energy barriers around the smaller band gap semiconductor leading to additional confinement effects. While this type of quantum-dot/quantum-well configuration does not provide any benefit regarding the electronic structure for the development of our intermediate band material, it proves the fine property tuning we can obtain using wet-chemistry techniques when dealing with semiconductor quantum-dots, especially for light emitting devices based on NCs.

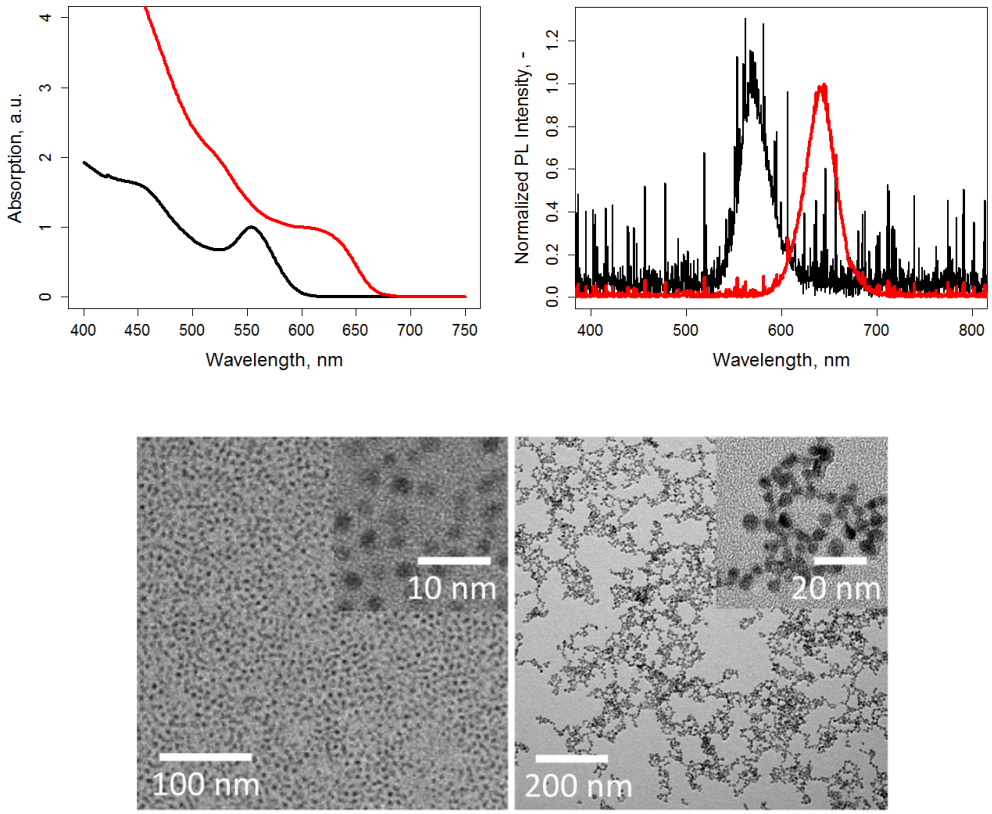

Figure 21 *– absorption and photoluminescence spectra for CdSe cores (solid black) and for CdSe/CdS core-shells (red). Transmission electronic microscopy images for core and core-shell systems in hexane, respectively left and right.*

Absorption and PL spectra of the core and core-shell NCs are presented in Figure 23. As seen in Figure 23a, after the addition of the first half-ML, $CdSe/S^{2-}$, the first electron transition peak in absorption spectrum broadens and shifts to shorter wavelengths most probably due to a partial surface etching of the CdSe core (Figure 23a). Although addition of the Cd^{2+} layer leads to a remarkable red shift of the peak, its maximum is still blue-shifted relative to that of parent CdSe NCs. Only after adding the second ML (ZnS) one can see a small shift of the absorption maximum to longer wavelengths continued by depositing the third and the fourth shell layers. Despite these unpredictable changes in absorption spectra during deposition of the first ML, the PL behaves as expected, i.e. the spectral maxima continuously move to longer wavelengths after each step including the first half-ML (Figure 23b). Growth of the last fourth layer does not lead to prominent changes either in absorption of the NCs or in their PL, positions of both maxima are quite close to those of CdSe/CdS/ZnS/CdS NCs. Apparently, the main changes in absorption spectra, and namely in their shape and positions of the first and the second electron transitions, occur upon addition of the first two S^{2-} layers, when communication between the outer shell layer and the core is most efficient.

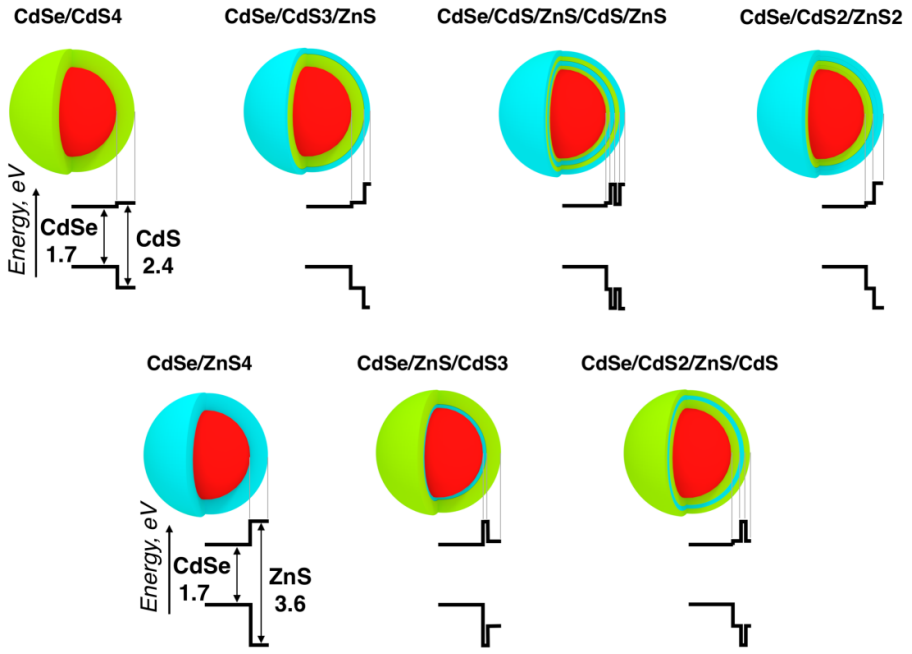

Figure 22 *– scheme of the investigated shell combinations with corresponding energy band diagrams of CdSe, CdS and ZnS. Numbers of layers are indicated after the composition with a final shell thickness of 4 MLs for all the samples. Positions of the energy levels are depicted based on corresponding bulk energy levels. Reprinted with permission from ref [*102*]. Copyright 2017 American Chemical Society.*

Thus, on the example of the formation of CdSe/CdS/ZnS/CdS/ZnS alternated shell structure starting from 3.3 nm CdSe cores, we demonstrate a fine control over the emission wavelength from green (λ_{max} = 567) to orange-red (λ_{max} = 608) during the growth of either CdS or ZnS shell layers (Figure 23b). Figure 23d presents a comparison between the PL spectra acquired before and after the c-ALD. The spectral shape, symmetrical profile and the full-width at half-maximum of the PL spectra can be considered as a measure of the NC size distribution and an overall quality of the particles. One can clearly see that the FWHM value was not altered after the 4ML shell growth, as compared to that of the initial core sample (the two x-axes have been shifted for superposition of the peaks). This observation suggests the preservation of the standard size deviation of the heterostructured NCs under the employed synthesis conditions, a result which is almost unattainable by means of other shell growth techniques.[103] The data presented in Table 2 reveals that the growth process is quite homogeneous, although for some shell compositions we can notice slight broadening of the PL spectra during c-ALD. We note that stability in polar solvents has always been a major issue for NC storage. We noticed a good stability of our purified NCs in MFA (ε_r = 182) only within weeks. NCs dissolved in other polar solvents, e.g. formamide (ε_r = 110), precipitated after a few hours. The surface functionalization of inorganic-capped NCs with amines enables to significantly enhance their colloidal stability as will be used for Au/CdS NCs (see next section).[104]

Table 2 *– evolution of the crystal size dispersion expressed as FWHM of the PL spectra (in eV) for different shell compositions. Reprinted with permission from ref [*102*]. Copyright 2017 American Chemical Society.*

#ML	/CdS 4	/CdS/ZnS/CdS/ZnS	/ZnS4	/CdS3/ZnS	/ZnS/CdS3	/CdS2/ZnS/CdS	/CdS2/ZnS 2
0	0.14	0.14	0.10	0.10	0.10	0.10	0.10
0.5	0.14	0.14	0.15	–	–	0.15	0.13
1	0.11	0.11	–	0.13	0.20	–	0.18
1.5	0.11	0.11	0.16	0.11	0.13	0.10	0.17
2	0.10	0.12	0.12	0.10	0.14	0.10	0.15
2.5	0.10	0.10	–	0.12	0.14	–	0.16
3	0.10	0.12	0.14	0.11	0.16	0.10	0.16
3.5	0.10	0.12	0.11	0.14	0.15	0.11	0.17
4	0.12	0.14	0.13	0.15	0.13	0.13	0.16

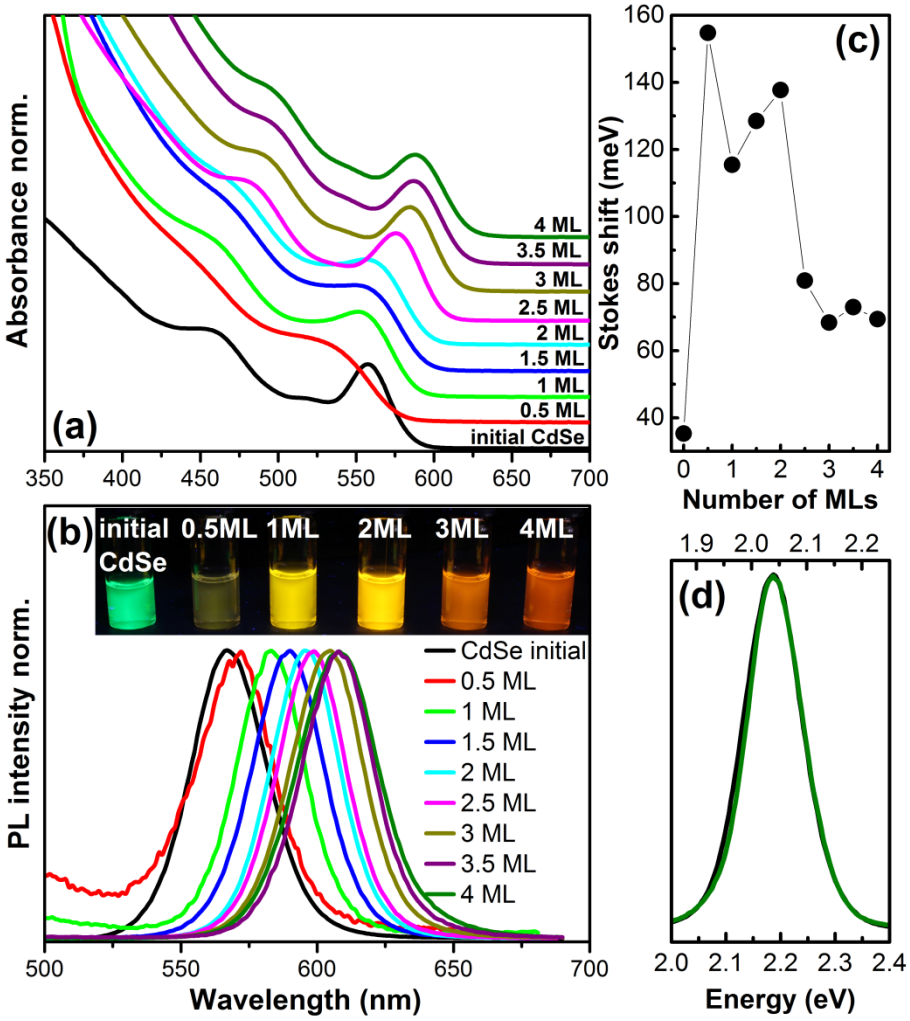

Figure 23 *– evolution of the absorption (a) and the PL (b) spectra as well as values of the Stokes shift (c) of CdSe NCs during their alternate shelling with CdS and ZnS forming the CdSe/CdS/ZnS/CdS/ZnS structure. Inset in (b) shows PL color evolution (samples under UV light) during the shelling. (d) PL spectra of the initial CdSe and the final multishell NC structure (plotted on energy scale and superposed to match the peak maxima in the same point) clearly demonstrating that the FWHM was not broadened (0.125 eV for the initial CdSe NCs vs 0.118 eV for the final NC structure). Reprinted with permission from ref [*102*]. Copyright 2017 American Chemical Society.*

In addition to the above discussed fine tuning of the absorption and emission spectra, shelling *via* c-ALD also provides a means to control the Stokes shift of the quantum dots. In the case of the CdSe/CdS/ZnS/CdS/ZnS structure we see the largest change in the Stokes shift (from 35 meV to 155 meV) upon depositing the first sulphur layer mostly due to partial NC etching and high concentration of surface defects (Figure 23c). The Stokes

shift remains quite large for the first two MLs and then decreases by adding the third and the fourth MLs down to 69 meV, which is still twice larger than the initial value. As in the case of standard shelling procedures, c-ALD results in the overall increase of the PL intensity of the quantum dots. The value of the PL intensity remained almost unaltered during the first ML (ZnS) deposition, thereafter it raised upon adding next three CdS layers and its intensity increased six-fold of the starting value for the parent CdSe NCs going through the maximal enhancement in CdSe/ZnS/CdS2 NC heterostructure (ten-fold increase). From the graph we clearly see that PL drops after each S^{2-} layer deposition and goes up upon covering with Cd^{2+}. For example, the PLQY of CdSe/CdS3/ZnS NCs was estimated as 42 %, which was much higher compared to that of the initial CdSe NC core (17 %). Optical characterisation for other core-shell systems developed by c-ALD is reported in Appendix B.

Figure 24 shows representative TEM images of the initial 3.8 nm CdSe core NCs and 4.5 nm CdSe/CdS4 core/shell NCs revealing their narrow size distribution. This imaging is a good indication of the quality of the shell growth process, which succeeded to preserve NC size distribution, one of the major limitations in obtaining high quality heterostructures by means of solution-based techniques.

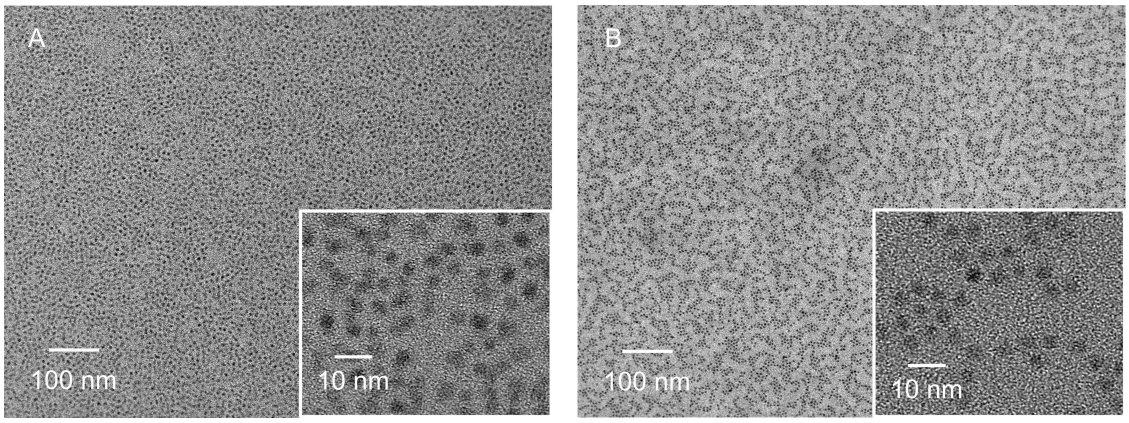

Figure 24 *– TEM images taken at different magnifications of the initial 3.8 nm core CdSe NCs (A) and the resulting CdSe/ZnS/CdS3 core/shell NCs (B). Reprinted with permission from ref [*102*]. Copyright 2017 American Chemical Society.*

The powder XRD patterns of the intial CdSe and CdSe/CdS3/ZnS NCs are presented

in Figure 25. The growth of the CdS shell with added 1 ML of ZnS resulted in narrowing of all reflections and their shift to larger 2θ values due to smaller CdS (ZnS) lattice constant compared to that of CdSe core NCs. The narrowing of the reflections can be explained by a good epitaxial contact between the core and shell materials as well as increasing grain size after shelling.

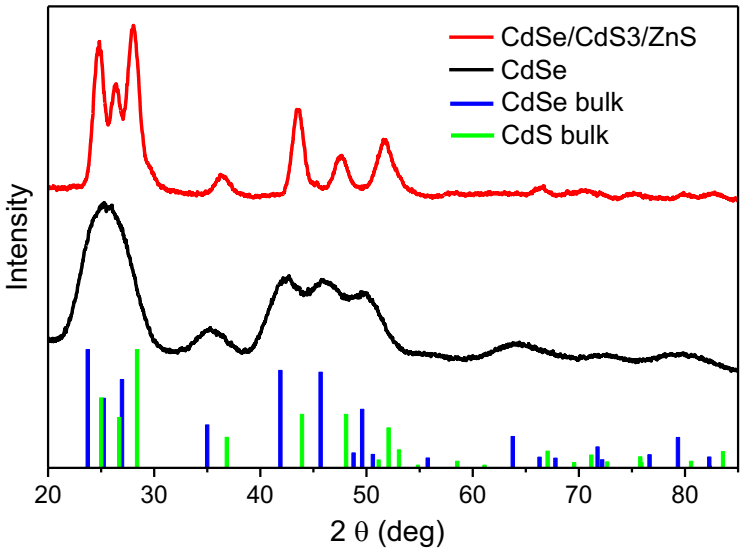

Figure 25 *– powder XRD patterns measured for CdSe core and CdSe/CdS3/ZnS heterostructure NCs. The stick patterns show the standard peak positions of the bulk wurtzite CdSe (blue) (COD#9011664) and CdS (green) (COD#9008862). Note that thin ZnS shell layer (1ML) does not change the position of the reflections compared to thicker CdS (3ML). Reprinted with permission from ref [*102*]. Copyright 2017 American Chemical Society.*

The combination of two or more semiconductor materials in one multicomponent structure allows us to modulate and control NC functional properties by means of wave-function engineering.[105] To evaluate the degree of wave function delocalization, we used the evolution of the $1S_e$–$1S_h$ exciton transition energy during the shelling process.[105–107] From Figure 26a one can distinguish a greater volume extent of electron wave function for CdSe/CdS4 compared to that of CdSe/CdS/ZnS/CdS/ZnS NCs. The former structure entails the electron delocalization across the entire core-shell particle owing to a low energy barrier between conduction band edges of CdSe and CdS (see Figure 22), while holes are mainly localized within the CdSe core (quasi-Type-II band alignment). The introduction of a thin ZnS layer (1ML) between two CdS layers partly decouples these two regions leading to a reduced probability of the full delocalization of the electron wave function.

Interestingly, the deposition of the same thin 1 ML ZnS (~0.31 nm) shell directly on the CdSe core (in contrast to the above-mentioned ZnS layer that was added on CdS layer) provides a stronger localization of the electrons in the core (Figures 22, 26b and 27). This weak dependence of charge carrier localization on both core size and the thickness of thin shell layers (1–2 ML) is clearly observed for the other four samples in CdSe/CdS/ZnS system. This is in contrast to the previous results published by the Klimov group for ZnSe/CdSe heterostructures.[108,109] The degree of charge carrier localization was stated to change with the size of each domain, i.e. with core radius and shell thickness, resulting in a modification of the strength and nature of carrier-carrier interactions. The latter led to the transition from standard Type-I to Type-II and inverted Type-I heterostructures in ZnSe/CdSe quantum dots. These discrepancies with the data observed in the current work can be attributed to the larger energy offsets between the core CdSe and the shell ZnS materials ($U_o^e = 1.27$ eV and $U_o^h = 0.60$ eV),[24,110] as compared to ZnSe and CdSe ($U_o^e = 0.86$ eV and $U_o^h = 0.14$ eV)[108] (Figure 22). This results in the strong effect on the localization regime of the carriers in the heterostructures. On the other hand, we assume that the larger crystal lattice mismatch between CdSe and ZnS phases can result in the formation of dislocations, additional defects and interfacial strains, which directly influence the band offset and thus exciton confinement, which makes additional contribution to exciton localization.[111] Moreover, the presence of such defects is likely responsible for a remarkable blue shift relative to the initial CdSe NCs (Figures 26b).

The subsequent CdS shell growth extends carrier delocalization as evidenced in gradual red-shift in the absorption spectra (Figure 27b). As expected, the relaxation of quantum confinement is more pronounced in smaller CdSe NCs as one can compare the electron delocalization from CdSe core (3.3 nm *vs* 3.8 nm) into the CdS shell with the same thickness (Figures 27a, b). Increasing ZnS content in the shell leads to a larger energy of the transition (lower degree of delocalization experienced by the excited charge carriers), as depicted in Figure 28. The samples are listed in order of increasing the total number of ZnS monolayers within the shell, starting from the pure CdS shell (0 MLs) to the pure ZnS one (4 MLs). Since the incorporation of the ZnS layers causes an increase of electron localization in the conduction band, higher values of the transition energy are associated with a larger content of ZnS in the shell and depend also on the position (distance from the core) of the ZnS layers within the shell structure.

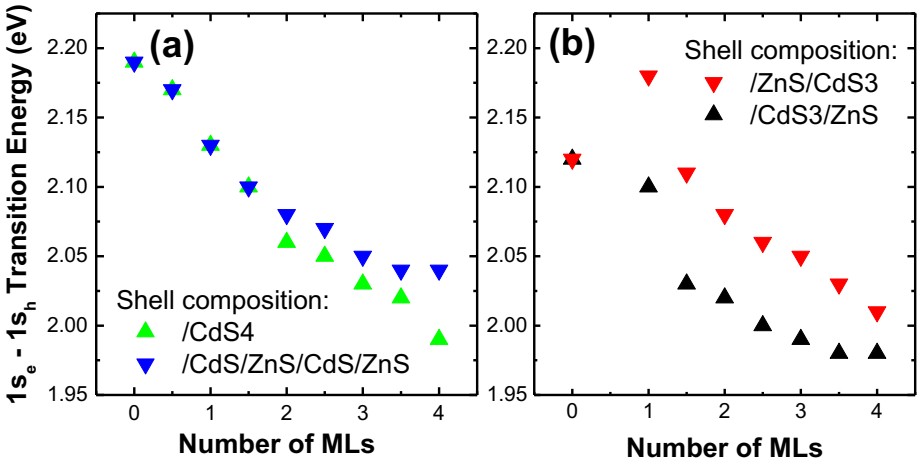

Figure 26 *– evolution of the $1S_e$–$1S_h$ transition energy for different shell configurations: the presence of ZnS within the shell causes a smaller redshift (a); sequence of the shelling materials influences the transition energy (b). Reprinted with permission from ref [102]. Copyright 2017 American Chemical Society.*

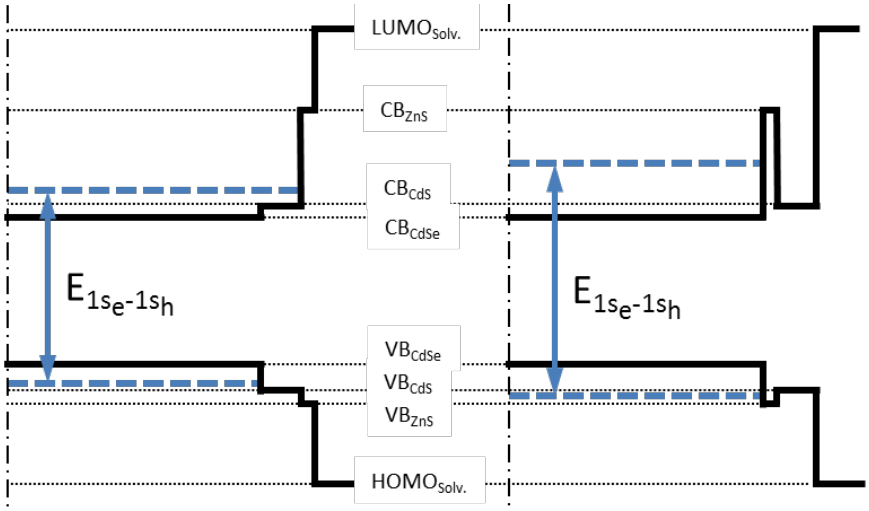

Figure 27 *– evolution of the $1S_e$–$1S_h$ transition for different shell configurations: the presence of ZnS after (left) or before (right) the sequence of three CdS MLs dramatically changes the configuration of the confinement potential. In the latter case, both the hole and especially the electron are more confined, leading to a wider $E_{1Se-1Sh}$ transition, i.e. to a blue shift. This effect would be valid even with an attenuated delocalization of the hole wave function into the CdS shell. Reprinted with permission from ref [102]. Copyright 2017 American Chemical Society.*

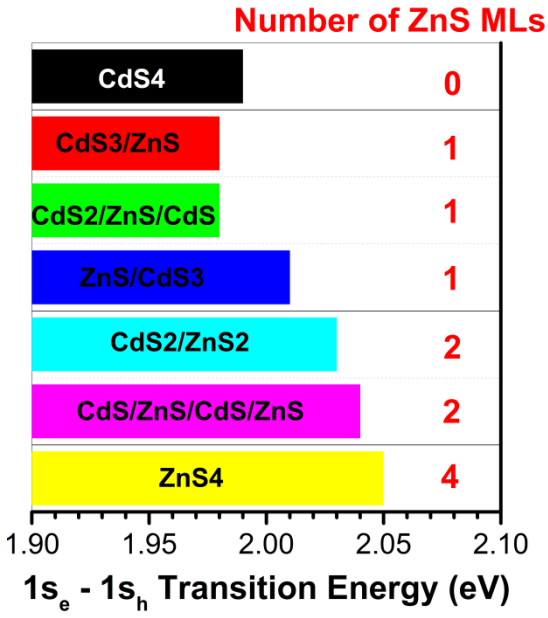

Figure 28 *– diagram representing the value of the $1S_e$–$1S_h$ transition (in eV) for seven different shell combinations: increasing the content of ZnS in the shell leads to a smaller red-shift. Reprinted with permission from ref [*102*]. Copyright 2017 American Chemical Society.*

Our results demonstrate that it is possible to grow ZnS shells on CdSe cores *via* c-ALD in a controlled manner, and even to stack multiple instances of different materials without losing coherence and preserving the monodispersity of the starting sample (Table 2). On the other hand, since the shell growth takes place at room temperature, this hampers the achievement of high PL QY in these heterostructures. Nevertheless, the measured PL QY of the core-shell NCs reached as high as 50%. The technique has been evaluated for materials such as cadmium sulphide and zinc sulphide, but its potential extension and versatility to other II-VI compounds is expected. In particular for the development of other metal sulphide and metal selenide compounds, since the metal acetate precursors are a common chemical reagent in the colloidal synthesis of quantum dots and potassium (ammonium) sulphide/selenide powders are soluble in MFA.

Metal-semiconductor systems by c-ALD

The colloidal synthesis discussed above enables to prepare semiconductor core-shell nanoscale multicomponent structures that combine materials with similar functionalities, .

Additionally, the opportunity to integrate components with intrinsically different characteristics (metal-semiconductor, magnet-semiconductor, *etc.*) in one nanoscale unit can open a powerful route to functional materials with novel properties. Previously, Zhang *et al.*[112] demonstrated the fabrication of a wide range of nanoscale heterostructures consisting of a metal core and monocrystalline semiconductor shell with a substantial lattice mismatch between them. However, the method entails a number of tedious synthetic steps strongly controlled by a Lewis acid-base reaction mechanism. On the other hand, we see no obstacles for using c-ALD as an alternative approach to grow a semiconductor shell on a metallic core. In a similar manner as the one presented for semiconductor-semiconductor systems, using self-limiting half-reactions of S^{2-} and Cd^{2+} on the surface of Au NCs, we created the shell layer with varied CdS thickness up to 7 ML around the quasi-spherical metal cores. However, in contrast to CdSe-based core/shell NCs, the all-inorganic Au/CdS*n* NCs (*n* is the number of CdS shell MLs) were found to precipitate within a few days regardless of the shell thickness. To improve the colloidal stability of the core/shell NCs, we adapted the technique recently developed by Eychmüller group.[104] It is based on the ability of amine-functionalized ligands to modify the labile diffusion region of the inorganic-capped NCs. In particular, the surface functionalization of the NCs with oleylamine enables to transfer the inorganic-capped NCs from polar (MFA) to non-polar (toluene) phase.

Figure 29 shows TEM images of starting 4 nm Au cores and the hybrid-capped Au/CdS7 NCs, confirming the formation of a uniform semiconductor layer on the surface of Au *via* c-ALD deposition. During the CdS shell growth, the average particle diameter increases from 4 nm to ~8.5 nm, which corresponds to a shell thickness of approx. 2.3 nm, perfectly matching the expected 7 ML thickness of the CdS shell layer. Interestingly, the narrow-size distribution of centrosymmetric Au/CdS7 NCs allowed their self-assembly into ordered structures.

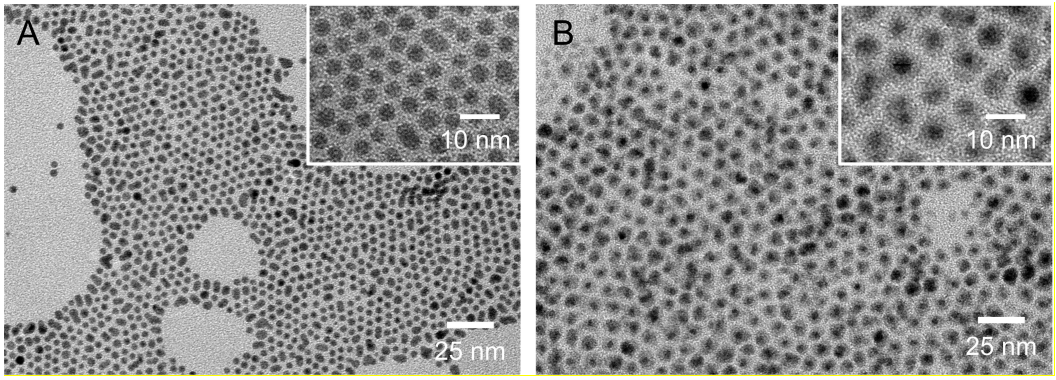

Figure 29 – *TEM images of the Au cores and the Au/CdS7 core/shell NCs. Reprinted with permission from ref [*102*]. Copyright 2017 American Chemical Society.*

CdS shell growth on gold cores has been monitored by absorption spectroscopy during c-ALD. The localized surface plasmon resonance (LSPR) peak gradually broadened and red-shifted with increasing CdS shell thickness (Figure 30a). Particularly, LSPR maximum shifted from 512 nm in bare Au NCs to 618 nm in Au/CdS7 core/shell NCs. Such behavior can be explained by the increase of the effective dielectric constant around plasmonic NCs with increasing shell thickness.[113] The enhanced plasmon-exciton interaction can lead to the spectral broadening of the LSPR. The increased absorption cross-section at energies higher than the CdS band gap (~510 nm) is consistent with the formation of a CdS shell, as one can clearly see already for Au/CdS3 NCs. The presence of the LSPR peak after multiple layers grown, in accordance with Lambright *et al.*,[114] is a clear indication that gold cores have preserved their integrity during the process, irrespective to the amount of the shell formed. No light is emitted by gold-cadmium sulphide core-shell structures: as the Au Fermi level lays below the CdS conduction band, that promotes the charge transfer toward the metal core causing the quenching of the emission of this structure[115].

The XRD patterns revealed the presence of characteristic reflexes of fcc Au and hexagonal CdS phases (Figure 30b). The larger fraction of CdS in Au/CdS7 than in Au/CdS3 NCs is reflected in the enhanced intensity of (100) and (101) as well as (112) peaks at $2\theta = 24.9°$, $2\theta = 28.2°$ and $2\theta = 51.9°$, respectively. This opportunity of the formation of the highly crystalline shell layers around the core NCs with large lattice mismatch at room temperature opens up new perspectives for the c-ALD approach to synthesize diverse heterostructures with tunable compositional complexity and properties.

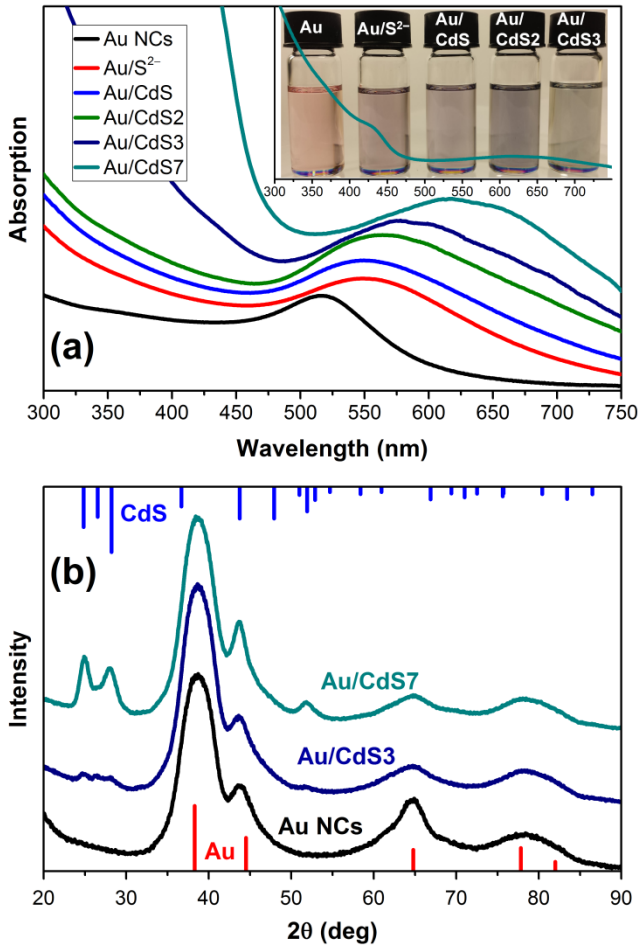

Figure 30 *– (a) absorbance spectra of the initial Au core (with diameter of ~4 nm) and core/shell Au/CdS NCs with varied shell thickness functionalized with oleylamine and dissolved in toluene (a). The inset shows a full spectrum of the Au/CdS7 NCs demonstrating a clear absorption of CdS shell (a shoulder between 400 and 450 nm) and a photo of the NC dispersions. (b) Powder XRD patterns of the Au core, Au/CdS3 and Au/CdS7 core/shell NCs exhibiting all reflections expected from the fcc Au and wurtzite CdS crystal structures. The stick patterns show the standard peak positions of the bulk Au (bottom red sticks, COD#9012953) and CdS (top blue sticks, (COD#9008862). Reprinted with permission from ref [*102*]. Copyright 2017 American Chemical Society.*

Phase-Transferred NCs

The first set of phase-transfer was conducted using 3-mercaptopropionic acid (MPA). An example of the optical spectra is reported in Figure 31. MPA is an organic molecule with a –SH functional group, which bound to Cd atoms after the loss of the hydrogen.

Interaction between cadmium and sulphur is strong enough, and MPA can substitute all oleic acid molecules on the surface of NCs[90,91,116]. It is a well-studied system, in many cases the direct synthesis on crystals (especially CdTe) in water by means of thiol stabilisation has been proposed[117,118], but even with the benefit of the ligand molecular length reduction, we were not able to preserve the emission intensity after the transfer. After several attempts, we decided to switch ligands, and exploit the protocol developed for c-ALD to transfer core-shell NCs in polar solvent.

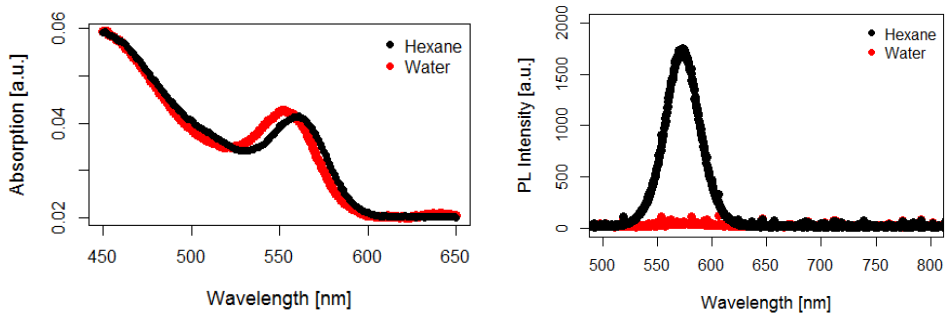

Figure 31 *– absorption and PL intensity spectra for core-shell QDs in hexane and after the transfer to water.*

Half-monolayer transfer by sodium sulphide

Sodium sulphide is a triatomic molecule composed of one sulphur atom and two atoms of sodium. When in contact with NCs, nucleophilic S^{2-} ions react with electron-deficient Cd^{2+} surface sites, removing oleic acid and transferring core-shell crystals from hexane to n-methylformamide[78]. Figure 32 shows the change in absorption and photoluminescence during the transfer, and the stable solutions from bare core in non-polar solvent to core-shell in polar media. Sodium atoms act as counterions in solution, stabilizing electrostatically the crystals. In this way, the complete stripping of long chain organic molecules is performed, and quantum dots can interact reciprocally transferring charge carriers. Contrary to what happened with MPA, now PL intensity actually increases after the transfer, whit a little redshift due to the further delocalisation of the electron inside the structure, caused by the growth of the S^{2-} layer on the NCs surface.

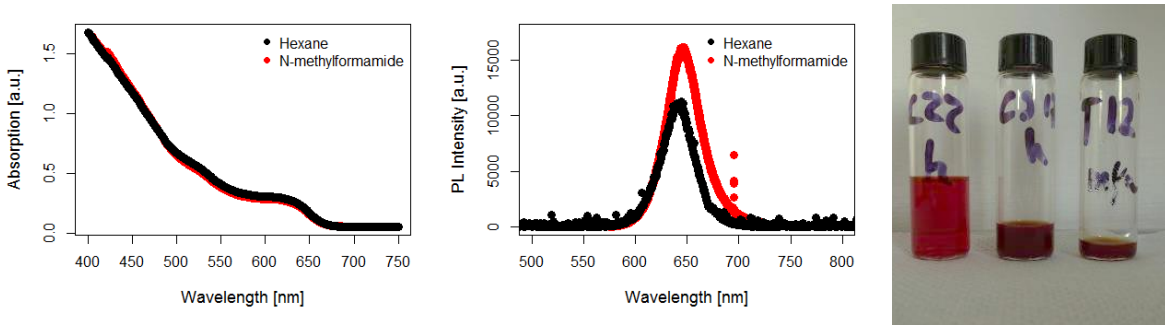

Figure 32 *– optical spectra before and after phase-transfer by sodium sulfide. The picture shows samples of NCs stable solutions in different solvents (from left to right: CdSe core in hexane, CdSe/CdS core-shell in hexane, CdSe/CdS core-shell in MFA).*

Thin Films

NCs in MFA have been deposited on microscope glass substrates for further processing. The operation of drop-casting has been performed sequentially on a large number of cleaned substrates, so that all samples for thermal treatment have been prepared in the same conditions. Few droplets (usually 2 or 3) of a 4.9 μM solution are placed on the substrates up to fully cover their surface. The dark brown liquid film samples are placed in the vacuum chamber and left two days to evaporate the solvent completely.

As-deposited films

Once films are completely dried, they are characterised optically by absorption and emission. Figure 33 shows the spectra collected for one of the samples prepared. This represents the reference baseline for the successive treatments of the films. Figure 33 also presents the XRD analysis, where due to the reduced thickness of the film, it is impossible to observe sharp peaks. The lack of 3 well-defined peaks in the range 24-28 degrees suggest a cubic structure for the samples.

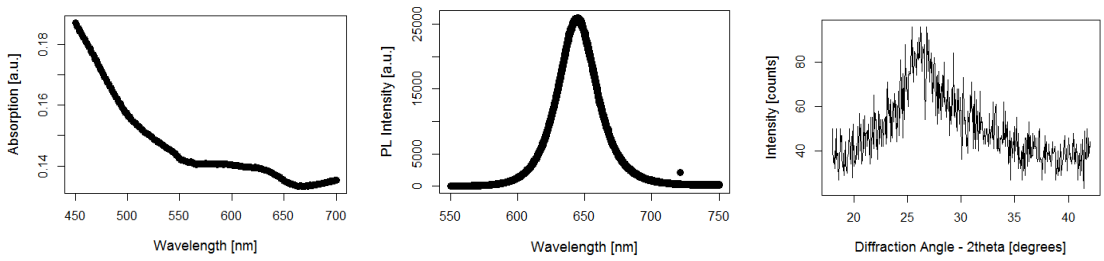

Figure 33 *– absorption and emission spectra for one characteristic sample and XRD.*

Sintered films

Samples inserted in glass tubes with controlled nitrogen atmosphere inside the tubes have been sintered at various temperatures, from 300°C up to 550°C. Temperature higher that 600°C would soften the glass walls, causing potential leakage of inert gas. Every series presented 7 different samples, each one with a different treatment duration: 2, 4, 8, 16, 32, 64 and 128 minutes. After the treatment, samples inside the tubes have been cooled down in air, then the glass was broken and the films characterized optically. Figure 35 presents an overview on the evolution of the emission wavelength for the main peak. Samples have been excited by a 514 nm laser source on an area of 400x650 μm^2 centred in the middle of the film, collecting photoluminescence from an average of 80 spots per sample. After removing a quadratic background, each spectrum has been fitted by a Gaussian curve like in Figure 34. The map colour in Figure 35 indicates the fitted peak centre, and provides a general picture about the uniformity of the film in terms of optical emission. As one can observe, there is a substantial PL redshift during the treatment, indicated by the mean value and standard deviation on top of every map. The redshift is, furthermore, more pronounced at higher temperature, supporting the thermal activation feature of the sintering process. Beside this, there is a degradation of the film uniformity, expressed by the standard deviation, and easily detected by looking at the colour distribution in single maps. Redshift of photoluminescence is a forecasted effect during sintering, since the electrons within the core-shell perceive an increased delocalisation of their wave function (weakening of quantum confinement) due to the melting and rearrangement of CdS shell material.

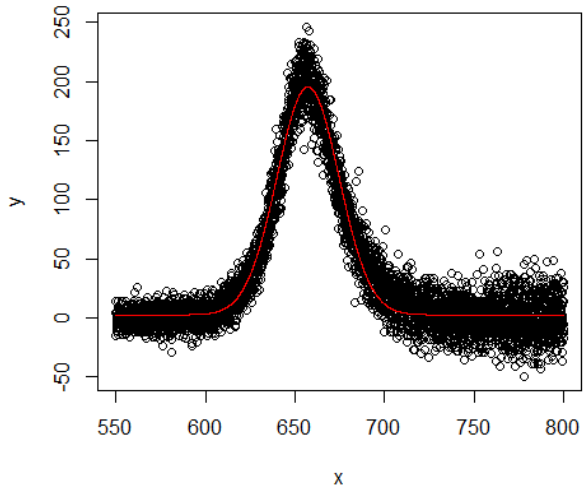

Figure 34 *– Gaussian fitting of the PL spectrum for one exemplificative sample. Quadratic background has been removed before analysis.*

Statistics from emission maps can be presented in form of plot like Figure 36, where the data is presented in a more concise and less structured way. We can observe how the wavelength shifts from 644 nm toward larger values, depending on process temperature and time. Small shifts are associated to lower temperature, as for 300 and 350°C the maximum wavelength is about 665 nm, while at 500°C the structure presents an emission peak located at 700 nm. In the plot, mean values obtained from maps are reported, and it is important to keep in mind how standard deviation, indicating the homogeneity of the sintering process throughout the film surface, increases with time and temperature (error bars not shown for image clarity). From this dataset, we didn't get any clear evidence of interdiffusion between core and shell materials, opposite to what reported by Cozzarini[47] (see Appendix B).

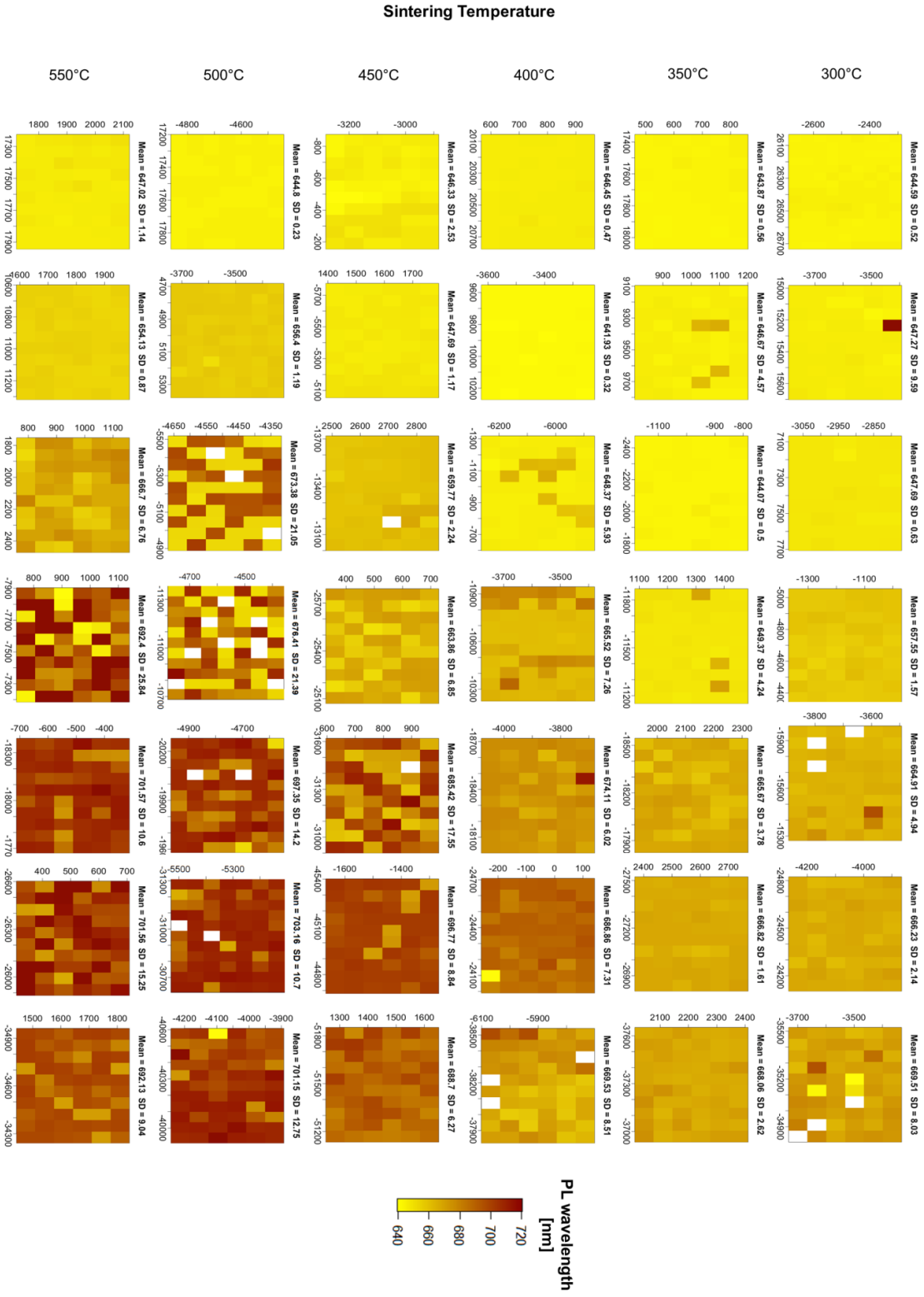

Figure 35 *– emission maps showing evolution of PL wavelength during sintering. On top of each map mean emission wavelength and standard deviation are reported. White spots inside the maps indicate uncertainity on the peak centre value.*

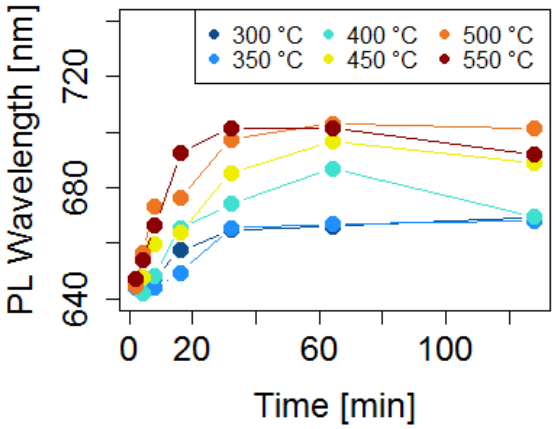

Figure 36 *– PL wavelength shift during sintering at different temperatures. Errors (not shown for clarity) linked to mean values are represented by standard deviation, as reported in Figure 35, with a maximum error of ±3.5%.*

Below Band-gap stimulated emission

Based on the theoretical electronic structure developed, a precise energy excitation below the band gap should be able to promote electron from the intermediate state in the CdSe cores to the conduction band, since within the forbidden gap there should be an electron filled level generated by the presence of the CdSe quantum dots. Based on the optical transitions of the system in solution, we expect the intermediate states to be located less than 2 eV below the conduction band-edge. We excited the samples with a 633 nm laser (1.96 eV) and collected the emission in the range 510-530 nm. A low intensity peak was detected in all samples at 520 nm, a figure extremely close to the bulk CdS band-gap (2.4 eV). The peak has been fitted with a Gaussian curve, Figure 37, to obtain the peak centre and its height; intensity has been monitored during the thermal treatment, observing a slightly increment with sintering time.

The large offset between excitation and emission (more than 100 nm) of the upconversion peak indicates that it is not related to the standard anti-Stokes photoluminescence of colloidal nanostructures[119,120]. A second option was based on multi-photons absorption processes (MPA): in fact, when for example two photons are absorbed simultaneously, upon relaxation one higher energy photon is emitted. In this scenario, anyway, no real intermediate states are requested, and the dependency of the emission

intensity with the power source in non-linear. We performed an experiment, varying the laser power and observing how the peak height is affected. Results are reported in Figure 37. The linear trend clearly indicates how the process behind the upconversion peak is based on one single photon absorption. Anti-Stokes luminescence due to MPA present a relationship between intensity and incident input light usually exponential, as reported for CdS thermally treated film[121]. In our case, anyway, the large offset could suggest the same process, but, as shown in Figure 37, our linear dependency let us discard this option. CdSe-CdS films have been compared to pure CdS samples sintered in the same conditions. The aim was the identification of a different mechanisms related to the appearance of the band-edge emission: in fact, while a linear trend indicates, as already mentioned, the absorption of single photons for each transition, a non-linear behaviour is associated to multiple photon absorption, Figure 38. The experimental data at hand is not sufficient to obtain conclusion on the precise number of particles associated to the transition, but a log-log plot suggests a two-photon absorption process in our sintered CdS films. In any case, it is clear that the two systems, sintered CdSe-CdS and sintered CdS films, present a totally different response mechanism to below band-gap excitation: while the latter requires simultaneous presence of multiple photons to promote electrons to the conduction band, for the intermediate band samples one is enough to observe the transition. This feature is strongly supportive of the assumption that our samples actually present an electron-filled intermediate band structure.

Below band-gap broadband excitation experiments have been performed on sintered films, but unfortunately the photon flux was not high enough to promote a sufficient number of electron in the conduction band and obtain a detectable emission. White light was used as excitation source, and longpass filter with cut-off at 570 nm has been installed so that only radiation with wavelength higher than 570 nm could reach the sample. As already mentioned, the power density of the light was not high enough to appreciate any emission from the film. Specific instrumentation is required to perform this type of measurements and demonstrate unequivocally the effectiveness of upconversion process.

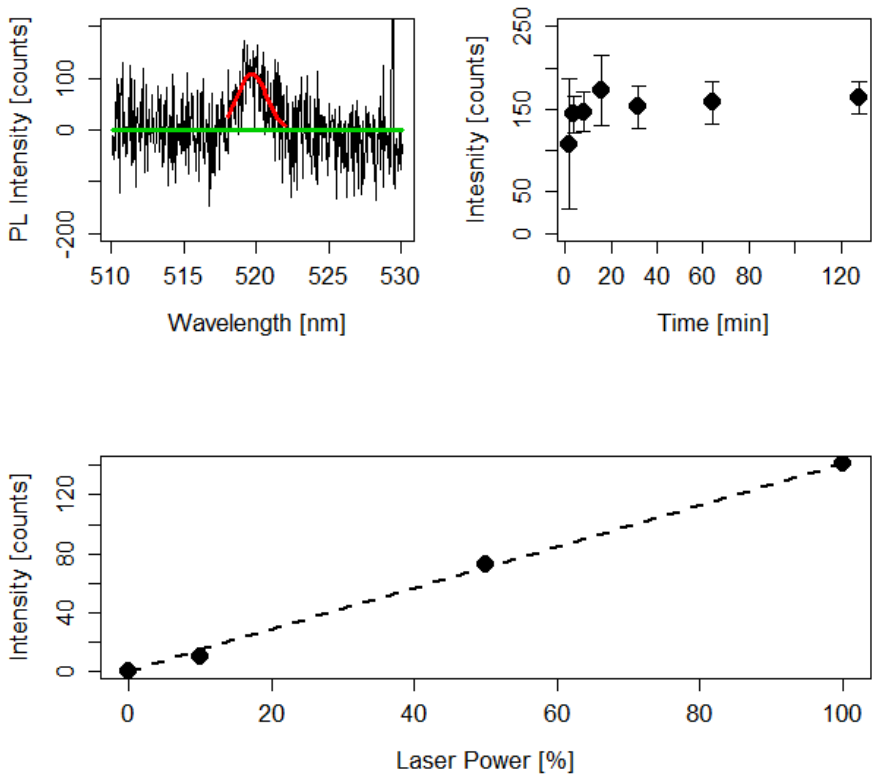

Figure 37 *– upconversion peak with gaussian fitting: green line represents the quadratic baseline, while the red one in the fit of the peak at 520 nm; evolution of the fitted peak intensity with sintering time; linear dependence of the intensity with excitation power: dashed line is a linear fitting, with equation y=1.416x and* R^2*=0.997.*

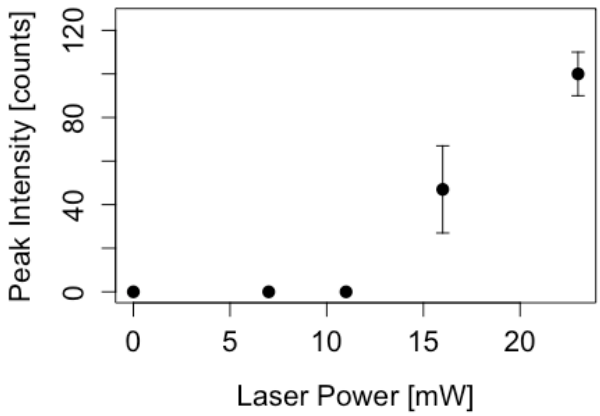

Figure 38 *– band-edge emission intensity at 520 nm of sintered CdS film as a function of excitation power. Up to 15 mW no peak has been detected, indicating a strong nonlinear behaviour.*

Further considerations

In this section, some peripheral aspects of the project will be discussed. They are not strictly linked to the scientific and technological part of the work, but they represent essential elements to evaluate and understand a project in its integrity and complexity. Here we will briefly discuss economic, social and environmental aspect related to the development of nanostructures as the ones presented in this work. Two main examples for this type of analysis are the Life Cycle Assessment and Ecological Footprint, which are mainly focused on environmental aspects. One innovative way to address directly the sustainability of a process and perform strategic selection based on different potential scenarios is to develop a 3-indicator analysis, where each index takes in consideration the amount of material needed, its hazard for humans and environment, its cost and different process strategies. At the end of the analysis, multiple options are compared and the optimal ones are easily identified. Such tools, as for example the Process Sustainable Prediction (PSP) Framework, are exploited for the responsible and sustainable management of processes, where combinations of economic, social and environmental domains are taken in consideration. For example, the United Nations developed several sustainable measurement tools to assess sustainable development, and in the last decade a crowded toolbox of quantitative methods has arisen, indicating a growing interest in the sustainable aspects of processes in general, and in the last years to nanomaterial too.

Cost of nanofabrication

It is not easy to address the cost of nanocrystal fabrication. It is, obviously, a key parameter to compare such technology with others, recognizing possible advantages and future market evolution. At the present state, the cost of nanofabrication is largely determined by the batch techniques and small volumes produced, with long and expensive processing besides of high-cost raw materials, due to the limited amount involved in the process and the lack of a large-scale supply stocks. The scale-up of any fabrication pattern

would produce a corresponding decrement of the processing and raw material costs; in this sense, for example, switching from a batch NCs synthesis to continuous-flow ones would represent an extreme advantage, and some notable examples have already been developed[122]. Any possible prediction of the magnitude of this decrement in the future industrial-phase is almost impossible to perform at the moment, since market dynamics are complex and ever-changing, but a comparison with similar advanced technologies could provide sufficient understanding and forecast power to present rough estimations. In this sense, looking for example to the cost history of silicon photovoltaic cells could provide some interesting insight: at the beginning of its technological deployment, one cell had a cost higher than 70$ per Watt. It was the 1977; since the date, an incredible decrement occurred, reaching a cost of 0.30$/Watt in 2015[§]. After just 10 years (1987), the cost dropped by 90%, and this trend is observed for other technological systems. It is reasonable to expect a similar evolution for quantum dots devices, once a market and determined applications are identified.

In our specific case, raw material cost is almost completely resolved by the selenium powder, accounting for almost 90% of the final total cost. To synthesize CdSe quantum dots in organic medium with the standard recipe reported in this work, usually 43$ have to be spent. This figure indicates how the batch production is extremely expensive, since only few milligrams of quantum dots are obtained, depending on the yield of the reaction. Indeed, at the moment, it is possible to purchase a stock solution of monodisperse quantum dots nanocrystals paying roughly 100$/10mg product, a price slightly cheaper compared to our production cost. It also suggests that a large scale diffusion is almost impossible, right now, with such large figure. Spending one hundred dollars for just few milligrams of product limits greatly the potential applications of NCs, and until new, higher-efficiency syntheses and processing techniques will be introduced, the NCs market would represent only a niche, affordable in academics or advanced technology centres for research purposes but not on a massive distribution level.

§ As found in Bloomberg new Energy Finance and pv.energytrend.com

Safety at the nanoscale

As stated at the beginning of this thesis, materials at the nanoscale not only modify their functional properties, but also the way they interact with human body and the environment. Such materials can originate from two different sources: natural and anthropogenic. In the first category we can find ultra-fine particles (size < 100 nm) generated by forest fire, volcanoes, viruses etc., while nanoparticles from power plant, jet engines, polymer fumes and engineered nanocrystals represent unintentional- and intentional-generated examples of the second category. Despite the difference of their origin, they share common features in terms of biological and environmental hazards and same toxicological principles are applied.

At the nanoscale, the same amount of mass concentration might produce an extraordinary high concentration of NCs, and it would be of toxicological significance when these particles interact with cells and subcellular components. Furthermore, their increased surface area per unit mass is toxicologically important if the other material characteristics, like surface composition and bulk chemistry, are the same. After all, the highly reactive surface area confers novel properties to these systems compared to their bulky counterparts, for example in terms of catalysis, and the same principle is valid if we consider adverse reaction with biological bodies. Nanocrystals can be intentionally administered for medical purposes, or after exposure during manufacturing or processing in industrial applications. The same positive and desirable properties which make NCs attractive for the development of nanomedicine and biomedical products or other industrial processes might prove deleterious when NCs interact with biological tissues and organs in an uncontrolled manner. Inhalation is the major route of exposure, yet ingestion and dermal exposure need to be considered during manufacturing and operational activity. Several studies have reported about the potential negative effects of exposure to NCs in terms of adverse health reactions[123–125]. The topics of safety and health related to operation at the nanoscale were also introduced in the independent report[**] made by the Royal Society and the Royal Academy of Engineering in 2003, where a raw regulation was proposed for the first time. Nowadays, safety data sheets are available with information about the storage, operations and toxicological values for every chemical substance sold in

[**] the complete report is available at the website: http://www.nanotec.org.uk/finalReport.htm

the regulated national and international markets. Good practice requires that each time a new compound is used, its safety data sheet has to be red in order to be aware of the treats and optimum handling of the substance: it is highly recommended to follow this simple rule.

The concern about the toxicology of nanocrystals are for sure one major limitation (alongside the economics explained in the previous section) for their diffusion and large-scale deployment, and represent a further constraint technicians have to keep in mind when they design nanostructured devices.

Conclusion

The project goal was the development of hybrid nanostructured assemblies based on II-IV semiconductor systems. We observed as a simple and cheap processing to obtained photoactive film is viable, with an accurate control of nanocrystal size thanks to the proposed solution-based techniques. We studied the kinetic of hot-injection synthesis, indicating how different parameters influences the yield of the process. In this sense, working at optimum condition to guarantee the maximum yield would be a key requirement for large-scale industrial production of nanocrystals. Theoretical models representing the nucleation and growth processes of NCs have been developed, and the proposed thermodynamic model fits particularly well both our experimental values and literature data. Complex multi-shell nanostructures have been synthesized with a novel and effective method based on colloidal Atomic Layer Deposition. We proved the effectiveness of the technique for multiple shell systems and metal-semiconductor combinations, working at low temperature and atmospheric pressure. We also investigated the opto-electronic properties of sintered film during thermal treatment, reporting a thermally activated redshift of PL peak due to reorganisation of the matter at the nanoscale. The developed heterostructure presented an interesting emission feature in the bandgap energy range when stimulated with below bandgap radiation. Unfortunately, the final evidence such phenomenon is due to intermediate band material-light interaction has not been obtained, yet.

Future perspectives

So much progress has been performed during these three years, but project is far to be completed: more characterisation is needed on sintered films to demonstrated the anti-Stokes PL via intermediate states transitions. Lifetimes measurements can be a valuable indication about the recombination path charge carriers possess; such information could provide insights about the recombination state (trap) locations. Such measurements have

not been performed yet for two main reasons: first of all we do not possess the required instrumentation in our facilities. Secondly, samples as synthesized with the protocol reported in this thesis are not free of defects, mainly introduced during the film deposition phase. This condition would sensibly limit the information obtained by lifetime measurements, but it keeps being one characterisation to perform.

Designing a new set of film deposition and treatment, it would be interesting to study how different combinations of core-shells, in terms of size, could affect mainly the anti-Stokes photoluminescence, up to the point where intermediate states (if present) would be located far away from the conduction band and no more sub-bandgap excitation, with consequent electron promotion, might occur.

In the end, the realisation of a complete device is still a main goal of the project. Further aspects have to be addressed before its development, anyway, and it will require expertise not already present in our research group. In particular, photolithography and other chemical and physical techniques of nanofabrication are required for the development and control of the functional layers (electrodes, active layer and so on). The simpler device architecture available is represented by a Schottky junction, composed of a metal-semiconductor junction, where the photogenerated current can be easily measured.

References

(1) Buffat, P.; Borel, J.-P. Size Effect on the Melting Temperature of Gold Particles. *Phys. Rev. A* **1976**, *13* (6), 2287–2298.

(2) Murray, C. B.; Kagan, C. R.; Bawendi, M. G. Synthesis and Characterization of Monodisperse Nanocrystals and Close-Packed Nanocrystal Assemblies. *Annu. Rev. Mater. Sci.* **2000**, *30* (1), 545–610.

(3) Moskovits, M. Surface-Enhanced Spectroscopy. *Rev. Mod. Phys.* **1985**, *57* (3), 783–826.

(4) Stoller, M. D.; Park, S.; Zhu, Y.; An, J.; Ruoff, R. S. Graphene-Based Ultracapacitors. *Nano Lett.* **2008**, *8* (10), 3498–3502.

(5) Chen, L.; Shaw, L. L. Recent Advances in Lithium–sulfur Batteries. *J. Power Sources* **2014**, *267*, 770–783.

(6) Farokhzad, O. C.; Langer, R. Impact of Nanotechnology on Drug Delivery. *ACS Nano* **2009**, *3* (1), 16–20.

(7) Veiseh, O.; Gunn, J. W.; Zhang, M. Design and Fabrication of Magnetic Nanoparticles for Targeted Drug Delivery and Imaging. *Adv. Drug Deliv. Rev.* **2010**, *62* (3), 284–304.

(8) Hua, M.; Zhang, S.; Pan, B.; Zhang, W.; Lv, L.; Zhang, Q. Heavy Metal Removal from Water/wastewater by Nanosized Metal Oxides: A Review. *J. Hazard. Mater.* **2012**, *211–212*, 317–331.

(9) Talapin, D. V.; Lee, J.-S.; Kovalenko, M. V.; Shevchenko, E. V. Prospects of Colloidal Nanocrystals for Electronic and Optoelectronic Applications. *Chem. Rev.* **2010**, *110* (1), 389–458.

(10) Ge, J.; Hu, Y.; Biasini, M.; Beyermann, W. P.; Yin, Y. Superparamagnetic Magnetite Colloidal Nanocrystal Clusters. *Angew. Chemie Int. Ed.* **2007**, *46* (23), 4342–4345.

(11) Park, J.; An, K.; Hwang, Y.; Park, J.-G.; Noh, H.-J.; Kim, J.-Y.; Park, J.-H.; Hwang, N.-M.; Hyeon, T. Ultra-Large-Scale Syntheses of Monodisperse Nanocrystals. *Nat. Mater.* **2004**, *3* (12), 891–895.

(12) Saldanha, P. L.; Lesnyak, V.; Manna, L. Large Scale Syntheses of Colloidal Nanomaterials. *Nano Today* **2017**, *12*, 46–63.

(13) *Nanoparticles*; de Mello Donegá, C., Ed.; Springer Berlin Heidelberg: Berlin, Heidelberg, 2014.

(14) Efros, A. L.; Rosen, M. The Electronic Structure of Semiconductor Nanocrystals. *Annu. Rev. Mater. Sci.* **2000**, *30* (1), 475–521.

(15) Gaponenko, S. V. (Sergey V. . *Introduction to Nanophotonics*; Cambridge University Press, 2010.

(16) Koole, R.; Groeneveld, E.; Vanmaekelbergh, D.; Meijerink, A.; de Mello Donegá, C. Size Effects on Semiconductor Nanoparticles. In *Nanoparticles*; de Mello Donegá, C., Ed.; Springer Berlin Heidelberg: Berlin, Heidelberg, 2014; pp 13–51.

(17) Wheeler, D. A.; Zhang, J. Z. Exciton Dynamics in Semiconductor Nanocrystals. *Adv. Mater.* **2013**, *25* (21), 2878–2896.

(18) Boles, M. A.; Ling, D.; Hyeon, T.; Talapin, D. V. The Surface Science of Nanocrystals. *Nat. Mater.* **2016**, *15* (2), 141–153.

(19) Carbone, L.; Nobile, C.; De Giorgi, M.; Sala, F. Della; Morello, G.; Pompa, P.; Hytch, M.; Snoeck, E.; Fiore, A.; Franchini, I. R.; Nadasan, M.; Silvestre, A. F.; Chiodo, L.; Kudera, S.; Cingolani, R.; Krahne, R.; Manna, L. Synthesis and Micrometer-Scale Assembly of Colloidal CdSe/CdS Nanorods Prepared by a Seeded Growth Approach. *Nano Lett.* **2007**, *7* (10), 2942–2950.

(20) Rice, K. P.; Saunders, A. E.; Stoykovich, M. P. Seed-Mediated Growth of Shape-Controlled Wurtzite CdSe Nanocrystals: Platelets, Cubes, and Rods. *J. Am. Chem. Soc.* **2013**, *135* (17), 6669–6676.

(21) Fiore, A.; Mastria, R.; Lupo, M. G.; Lanzani, G.; Giannini, C.; Carlino, E.; Morello, G.; De Giorgi, M.; Li, Y.; Cingolani, R.; Manna, L. Tetrapod-Shaped Colloidal Nanocrystals of II−VI Semiconductors Prepared by Seeded Growth. *J. Am. Chem. Soc.* **2009**, *131* (6), 2274–2282.

(22) Kim, M. R.; Miszta, K.; Povia, M.; Brescia, R.; Christodoulou, S.; Prato, M.; Marras, S.; Manna, L. Influence of Chloride Ions on the Synthesis of Colloidal Branched CdSe/CdS Nanocrystals by Seeded Growth. *ACS Nano* **2012**, *6* (12), 11088–11096.

(23) Pu, C.; Peng, X. To Battle Surface Traps on CdSe/CdS Core/Shell Nanocrystals: Shell Isolation versus Surface Treatment. *J. Am. Chem. Soc.* **2016**, *138* (26), 8134–8142.

(24) Reiss, P.; Protière, M.; Li, L. Core/Shell Semiconductor Nanocrystals. *Small* **2009**, *5* (2), 154–168.

(25) Costi, R.; Saunders, A. E.; Banin, U. Colloidal Hybrid Nanostructures: A New Type of Functional Materials. *Angew. Chemie Int. Ed.* **2010**, *49* (29), 4878–4897.

(26) Li, M.; Yu, X.-F.; Liang, S.; Peng, X.-N.; Yang, Z.-J.; Wang, Y.-L.; Wang, Q.-Q. Synthesis of Au-CdS Core-Shell Hetero-Nanorods with Efficient Exciton-Plasmon Interactions. *Adv. Funct. Mater.* **2011**, *21* (10), 1788–1794.

(27) Luque, A.; Martí, A.; Antolín, E.; Tablero, C. Intermediate Bands versus Levels in Non-Radiative Recombination. *Phys. B Condens. Matter* **2006**, *382* (1–2), 320–327.

(28) Luque, A.; Martí, A. Increasing the Efficiency of Ideal Solar Cells by Photon Induced Transitions at Intermediate Levels. *Phys. Rev. Lett.* **1997**, *78* (26), 5014–5017.

(29) Shockley, W.; Queisser, H. J. Detailed Balance Limit of Efficiency of *P-n* Junction Solar Cells. *J. Appl. Phys.* **1961**, *32* (3), 510–519.

(30) Hubbard, S. M.; Cress, C. D.; Bailey, C. G.; Raffaelle, R. P.; Bailey, S. G.; Wilt, D. M. Effect of Strain Compensation on Quantum Dot Enhanced GaAs Solar Cells. *Appl. Phys. Lett.* **2008**, *92* (12), 123512.

(31) Popescu, V.; Bester, G.; Hanna, M. C.; Norman, A. G.; Zunger, A. Theoretical and Experimental Examination of the Intermediate-Band Concept for Strain-Balanced (In,Ga)As/Ga(As,P) Quantum Dot Solar Cells. *Phys. Rev. B* **2008**, *78* (20), 205321.

(32) Martí, A.; Luque, A. Intermediate Band Solar Cells. *Adv. Sci. Technol.* **2010**, *74* (3), 143–150.

(33) Stranski, I. N.; Krastanow, L. Berichtigung Zur Arbeit. *Monatshefte für Chemie* **1939**, *72* (1), 76–76.

(34) Antolín, E.; Martí, A.; Stanley, C. R.; Farmer, C. D.; Canovas, E.; Lopez, N.; Linares, P. G.; Luque, A. Low Temperature Characterization of the Photocurrent Produced by Two-Photon Transitions in a Quantum Dot Intermediate Band Solar Cell. *Thin Solid Films* **2008**, *516* (20), 6919–6923.

(35) Cuadra, L.; Martí, a.; Luque, a. Present Status of Intermediate Band Solar Cell Research. *Thin Solid Films* **2004**, *451–452*, 593–599.

(36) Okada, Y.; Ekins-Daukes, N. J.; Kita, T.; Tamaki, R.; Yoshida, M.; Pusch, A.; Hess, O.; Phillips, C. C.; Farrell, D. J.; Yoshida, K.; Ahsan, N.; Shoji, Y.; Sogabe, T.; Guillemoles, J.-F.

Intermediate Band Solar Cells: Recent Progress and Future Directions. *Appl. Phys. Rev.* **2015**, *2* (2), 21302.

(37) Martí, a.; Antolín, E.; Cánovas, E.; López, N.; Linares, P. G.; Luque, a.; Stanley, C. R.; Farmer, C. D. Elements of the Design and Analysis of Quantum-Dot Intermediate Band Solar Cells. *Thin Solid Films* **2008**, *516* (20), 6716–6722.

(38) Antolín, E.; Martí, A.; Farmer, C. D.; Linares, P. G.; Hernández, E.; Sánchez, A. M.; Ben, T.; Molina, S. I.; Stanley, C. R.; Luque, A. Reducing Carrier Escape in the InAs/GaAs Quantum Dot Intermediate Band Solar Cell. *J. Appl. Phys.* **2010**, *108* (6), 64513.

(39) Goldschmidt, J. C.; Fischer, S. Upconversion for Photovoltaics - a Review of Materials, Devices and Concepts for Performance Enhancement. *Adv. Opt. Mater.* **2015**, *3* (4), 510–535.

(40) Zhou, J.; Liu, Q.; Feng, W.; Sun, Y.; Li, F. Upconversion Luminescent Materials: Advances and Applications. *Chem. Rev.* **2015**, *115* (1), 395–465.

(41) Green, M. A. *Third Generation Photovoltaics : Advanced Solar Energy Conversion*; Springer, 2006.

(42) Conibeer, G. Third-Generation Photovoltaics. *Mater. Today* **2007**, *10* (11), 42–50.

(43) Sellers, D. G.; Zhang, J.; Chen, E. Y.; Zhong, Y.; Doty, M. F.; Zide, J. M. O. Novel Nanostructures for Efficient Photon Upconversion and High-Efficiency Photovoltaics. *Sol. Energy Mater. Sol. Cells* **2016**, *155*, 446–453.

(44) Martı, a; Cuadra, L.; Luque, a. Design Constraints of the Quantum-Dot Intermediate Band Solar Cell. *Phys. E Low-dimensional Syst. …* **2002**, *14*, 150–157.

(45) Marti, A.; Cuadra, L.; Luque, A. Quantum Dot Intermediate Band Solar Cell. In *Conference Record of the Twenty-Eighth IEEE Photovoltaic Specialists Conference - 2000 (Cat. No.00CH37036)*; IEEE; pp 940–943.

(46) Marti, A.; Cuadra, L.; Luque, A. Partial Filling of a Quantum Dot Intermediate Band for Solar Cells. *IEEE Trans. Electron Devices* **2001**, *48* (10), 2394–2399.

(47) Cozzarini, L. Nanomaterials Based on II-VI Semiconductors, 2011.

(48) Finney, E. E.; Finke, R. G. Nanocluster Nucleation and Growth Kinetic and Mechanistic Studies: A Review Emphasizing Transition-Metal Nanoclusters. *J. Colloid Interface Sci.* **2008**, *317* (2), 351–374.

(49) Bullen, C.; Mulvaney, P. Nucleation and Growth Kinetics of CdSe Nanocrystals in

Octadecene. *Nano Lett.* **2004**, *4* (12), 2303–2307.

(50) Thanh, N. T. K.; Maclean, N.; Mahiddine, S. Mechanisms of Nucleation and Growth of Nanoparticles in Solution. *Chem. Rev.* **2014**, *114* (15), 7610–7630.

(51) Dushkin, C. D.; Saita, S.; Yoshie, K.; Yamaguchi, Y. Kinetics of Growth of Semiconductor Nanocrystals in a Hot Amphiphile Matrix. *Adv. Colloid Interface Sci.* **2000**, *88* (1–2), 37–78.

(52) Murray, C. B.; Norris, D.; Bawendi, M. G. Synthesis and Characterization of Nearly Monodisperse CdE (E= S, Se, Te) Semiconductor Nanocrystallites. *J. Am. Chem. Soc.* **1993**, *115* (4), 8706–8715.

(53) Park, J.; Joo, J.; Kwon, S. G.; Jang, Y.; Hyeon, T. Synthesis of Monodisperse Spherical Nanocrystals. *Angew. Chem. Int. Ed. Engl.* **2007**, *46* (25), 4630–4660.

(54) Abe, S.; Čapek, R. K.; De Geyter, B.; Hens, Z. Tuning the Postfocused Size of Colloidal Nanocrystals by the Reaction Rate: From Theory to Application. *ACS Nano* **2012**, *6* (1), 42–53.

(55) Abe, S.; Capek, R. K.; De Geyter, B.; Hens, Z. Reaction Chemistry/nanocrystal Property Relations in the Hot Injection Synthesis, the Role of the Solute Solubility. *ACS Nano* **2013**, *7* (2), 943–949.

(56) Wang, F.; Richards, V. N.; Shields, S. P.; Buhro, W. E. Kinetics and Mechanisms of Aggregative Nanocrystal Growth. *Chem. Mater.* **2014**, *26* (1), 5–21.

(57) Auer, S.; Frenkel, D. Numerical Prediction of Absolute Crystallization Rates in Hard-Sphere Colloids. *J. Chem. Phys.* **2004**, *120* (6), 3015–3029.

(58) Talapin, D. V.; Nelson, J. H.; Shevchenko, E. V.; Aloni, S.; Sadtler, B.; Alivisatos, A. P. Seeded Growth of Highly Luminescent CdSe/CdS Nanoheterostructures with Rod and Tetrapod Morphologies. *Nano Lett.* **2007**, *7* (10), 2951–2959.

(59) Deka, S.; Miszta, K.; Dorfs, D.; Genovese, A.; Bertoni, G.; Manna, L. Octapod-Shaped Colloidal Nanocrystals of Cadmium Chalcogenides via “One-Pot” Cation Exchange and Seeded Growth. *Nano Lett.* **2010**, *10* (9), 3770–3776.

(60) Carbone, L.; Cozzoli, P. D. Colloidal Heterostructured Nanocrystals: Synthesis and Growth Mechanisms. *Nano Today* **2010**, *5* (5), 449–493.

(61) Nag, A.; Kundu, J.; Hazarika, A. Seeded-Growth, Nanocrystal-Fusion, Ion-Exchange and Inorganic-Ligand Mediated Formation of Semiconductor-Based Colloidal Heterostructured

Nanocrystals. *CrystEngComm* **2014**, *16* (40), 9391–9407.

(62) Mer, V. K. La. Nucleation in Phase Transitions. *Ind. Eng. Chem.* **1952**, *44* (6), 1270–1277.

(63) Kwon, S. G.; Hyeon, T. Formation Mechanisms of Uniform Nanocrystals via Hot-Injection and Heat-up Methods. *Small* **2011**, *7* (19), 2685–2702.

(64) van Embden, J.; Sader, J. E.; Davidson, M.; Mulvaney, P. Evolution of Colloidal Nanocrystals: Theory and Modeling of Their Nucleation and Growth. *J. Phys. Chem. C* **2009**, *113* (37), 16342–16355.

(65) De Yoreo, J.; Whitelam, S. Nucleation in Atomic, Molecular, and Colloidal Systems. *MRS Bull.* **2016**, *41* (5), 357–360.

(66) Sear, R. What Do Crystals Nucleate on? What Is the Microscopic Mechanism? How Can We Model Nucleation? *MRS Bull.* **2016**, *41* (5), 363–368.

(67) Wasai, K.; Kaptay, G.; Mukai, K.; Shinozaki, N. Modified Classical Homogeneous Nucleation Theory and a New Minimum in Free Energy Change. *Fluid Phase Equilib.* **2007**, *254* (1–2), 67–74.

(68) Wasai, K.; Kaptay, G.; Mukai, K.; Shinozaki, N. Modified Classical Homogeneous Nucleation Theory and a New Minimum in Free Energy Change. *Fluid Phase Equilib.* **2007**, *255* (1), 55–61.

(69) Kovalenko, M. V.; Manna, L.; Cabot, A.; Hens, Z.; Talapin, D. V.; Kagan, C. R.; Klimov, V. I.; Rogach, A. L.; Reiss, P.; Milliron, D. J.; Guyot-Sionnnest, P.; Konstantatos, G.; Parak, W. J.; Hyeon, T.; Korgel, B. A.; Murray, C. B.; Heiss, W. Prospects of Nanoscience with Nanocrystals. *ACS Nano* **2015**, 150122081035000.

(70) Coe, S.; Woo, W.-K.; Bawendi, M.; Bulović, V. Electroluminescence from Single Monolayers of Nanocrystals in Molecular Organic Devices. *Nature* **2002**, *420* (6917), 800–803.

(71) B. O. Dabbousi, †; J. Rodriguez-Viejo, ‡; F. V. Mikulec, †; J. R. Heine, §; H. Mattoussi, §; R. Ober, ⊥; K. F. Jensen, ‡,§ and; M. G. Bawendi*, †. (CdSe)ZnS Core−Shell Quantum Dots: Synthesis and Characterization of a Size Series of Highly Luminescent Nanocrystallites. **1997**.

(72) Hines, M. A.; Guyot-Sionnest, P. Synthesis and Characterization of Strongly Luminescing ZnS-Capped CdSe Nanocrystals. *J. Phys. Chem.* **1996**, *100* (2), 468–471.

(73) Nicolau, Y. F. Solution Deposition of Thin Solid Compound Films by a Successive Ionic-Layer

Adsorption and Reaction Process. *Appl. Surf. Sci.* **1985**, *22–23*, 1061–1074.

(74) J. Jack Li, †; Y. Andrew Wang, ‡,§; Wenzhuo Guo, †; Joel C. Keay, ‡,∥; Tetsuya D. Mishima, ‡,∥; Matthew B. Johnson, ‡,∥ and; Xiaogang Peng*, †,‡. Large-Scale Synthesis of Nearly Monodisperse CdSe/CdS Core/Shell Nanocrystals Using Air-Stable Reagents via Successive Ion Layer Adsorption and Reaction. **2003**.

(75) Renguo Xie; Ute Kolb; Jixue Li; Thomas Basché, and; Alf Mews*, †. Synthesis and Characterization of Highly Luminescent CdSe−Core CdS/Zn0.5Cd0.5S/ZnS Multishell Nanocrystals. **2005**.

(76) Chen, D.; Zhao, F.; Qi, H.; Rutherford, M.; Peng, X. Bright and Stable Purple/Blue Emitting CdS/ZnS Core/Shell Nanocrystals Grown by Thermal Cycling Using a Single-Source Precursor. *Chem. Mater.* **2010**, *22* (4), 1437–1444.

(77) Cirillo, M.; Aubert, T.; Gomes, R.; Van Deun, R.; Emplit, P.; Biermann, A.; Lange, H.; Thomsen, C.; Brainis, E.; Hens, Z. "Flash" Synthesis of CdSe/CdS Core–Shell Quantum Dots. *Chem. Mater.* **2014**, *26* (2), 1154–1160.

(78) Ithurria, S.; Talapin, D. V. Colloidal Atomic Layer Deposition (c-ALD) Using Self-Limiting Reactions at Nanocrystal Surface Coupled to Phase Transfer between Polar and Nonpolar Media. *J. Am. Chem. Soc.* **2012**, *134* (45), 18585–18590.

(79) Delikanli, S.; Akgul, M. Z.; Murphy, J. R.; Barman, B.; Tsai, Y.; Scrace, T.; Zhang, P.; Bozok, B.; Hernández-Martínez, P. L.; Christodoulides, J.; Cartwright, A. N.; Petrou, A.; Demir, H. V. Mn^{2+}-Doped CdSe/CdS Core/Multishell Colloidal Quantum Wells Enabling Tunable Carrier–Dopant Exchange Interactions. *ACS Nano* **2015**, *9* (12), 12473–12479.

(80) Oh, S. J.; Berry, N. E.; Choi, J.-H.; Gaulding, E. A.; Lin, H.; Paik, T.; Diroll, B. T.; Muramoto, S.; Murray, C. B.; Kagan, C. R. Designing High-Performance PbS and PbSe Nanocrystal Electronic Devices through Stepwise, Post-Synthesis, Colloidal Atomic Layer Deposition. *Nano Lett.* **2014**, *14* (3), 1559–1566.

(81) and, L. Q.; Peng*, X. Control of Photoluminescence Properties of CdSe Nanocrystals in Growth. **2002**.

(82) Celso de Mello Donegá, *; Stephen G. Hickey; Sander F. Wuister; Daniel Vanmaekelbergh, and; Meijerink, A. Single-Step Synthesis to Control the Photoluminescence Quantum Yield and Size Dispersion of CdSe Nanocrystals. **2002**.

(83) Razgoniaeva, N.; Carrillo, L.; Burchfield, D.; Moroz, P.; Adhikari, P.; Yadav, P.; Khon, D.;

Zamkov, M. Colloidal Synthesis of Monodisperse Semiconductor Nanocrystals through Saturated Ionic Layer Adsorption. *Chem. Mater.* **2016**, *28* (8), acs.chemmater.6b00772.

(84) Sagar, L. K.; Walravens, W.; Zhao, Q.; Vantomme, A.; Geiregat, P.; Hens, Z. PbS/CdS Core/Shell Quantum Dots by Additive, Layer-by-Layer Shell Growth. *Chem. Mater.* **2016**, *28* (19), 6953–6959.

(85) Beaulac, R.; Archer, P. I.; Ochsenbein, S. T.; Gamelin, D. R. Mn^{2+}-Doped CdSe Quantum Dots: New Inorganic Materials for Spin-Electronics and Spin-Photonics. *Adv. Funct. Mater.* **2008**, *18* (24), 3873–3891.

(86) Mocatta, D.; Cohen, G.; Schattner, J.; Millo, O.; Rabani, E.; Banin, U. Heavily Doped Semiconductor Nanocrystal Quantum Dots. *Science (80-.).* **2011**, *332* (6025).

(87) Sahu, A.; Kang, M. S.; Kompch, A.; Notthoff, C.; Wills, A. W.; Deng, D.; Winterer, M.; Frisbie, C. D.; Norris, D. J. Electronic Impurity Doping in CdSe Nanocrystals. *Nano Lett.* **2012**, *12* (5), 2587–2594.

(88) Kovalenko, M. V.; Bodnarchuk, M. I.; Zaumseil, J.; Lee, J. S.; Talapin, D. V. Expanding the Chemical Versatility of Colloidal Nanocrystals Capped with Molecular Metal Chalcogenide Ligands. *J. Am. Chem. Soc.* **2010**, *132* (29), 10085–10092.

(89) Kovalenko, M. V; Scheele, M.; Talapin, D. V. Colloidal Nanocrystals with Molecular Metal Chalcogenide Surface Ligands. *Science* **2009**, *324* (5933), 1417–1420.

(90) Owen, J. S.; Park, J.; Trudeau, P.-E.; Alivisatos, A. P. Reaction Chemistry and Ligand Exchange at Cadmium−Selenide Nanocrystal Surfaces. *J. Am. Chem. Soc.* **2008**, *130* (37), 12279–12281.

(91) Wuister, S. F.; De Mello Donegá, C.; Meijerink, A. Influence of Thiol Capping on the Exciton Luminescence and Decay Kinetics of CdTe and CdSe Quantum Dots. *J. Phys. Chem. B* **2004**, *108* (45), 17393–17397.

(92) Jasieniak, J.; Smith, L.; Embden, J. Van; Mulvaney, P.; Califano, M. Re-Examination of the Size Dependent Absorption Properties of CdSe Quantum Dots. *J. Phys. Chem. C* **2009**, *113*, 19468–19474.

(93) Yu, W. W.; Qu, L.; Guo, W.; Peng, X. Experimental Determination of the Extinction Coefficient of CdTe , CdSe , and CdS Nanocrystals Experimental Determination of the Extinction Coefficient of CdTe , CdSe , and CdS Nanocrystals. *Chem. Mater.* **2003**, *125* (17), 2854–2860.

(94) Xiaogang Peng; J. Wickham, A.; Alivisatos*, A. P. Kinetics of II-VI and III-V Colloidal Semiconductor Nanocrystal Growth: "Focusing" of Size Distributions. American Chemical Society May 14, 1998.

(95) Wen, T.; Brush, L. N.; Krishnan, K. M. A Generalized Diffusion Model for Growth of Nanoparticles Synthesized by Colloidal Methods. *J. Colloid Interface Sci.* **2014**, *419*, 79–85.

(96) Avrami, M. Kinetics of Phase Change. I General Theory. *J. Chem. Phys.* **1939**, *7* (12), 1103.

(97) Avrami, M. Kinetics of Phase Change. II Transformation-Time Relations for Random Distribution of Nuclei. *J. Chem. Phys.* **1940**, *8* (2), 212.

(98) Kwon, S. G.; Hyeon, T. Colloidal Chemical Synthesis and Formation Kinetics of Uniformly Sized Nanocrystals of Metals, Oxides, and Chalcogenides. *Acc. Chem. Res.* **2008**, *41* (12), 1696–1709.

(99) Dickerson, B. D.; Irving, D. M.; Herz, E.; Claus, R. O.; Spillman, W. B.; Meissner, K. E. Synthesis Kinetics of CdSe Quantum Dots in Trioctylphosphine Oxide and in Stearic Acid. *Appl. Phys. Lett.* **2005**, *86* (17), 1–3.

(100) Moreels, I.; Fritzinger, B.; Martins, J. C.; Hens, Z. Surface Chemistry of Colloidal PbSe Nanocrystals. *J. Am. Chem. Soc.* **2008**, *130* (45), 15081–15086.

(101) van Embden, J.; Mulvaney, P. Nucleation and Growth of CdSe Nanocrystals in a Binary Ligand System. *Langmuir* **2005**, *21* (22), 10226–10233.

(102) Slejko, E. A.; Sayevich, V.; Cai, B.; Gaponik, N.; Lughi, V.; Lesnyak, V.; Eychmüller, A. Precise Engineering of Nanocrystal Shells via Colloidal Atomic Layer Deposition. *Chem. Mater.* **2017**, *29* (19), acs.chemmater.7b01873.

(103) Boldt, K. Graded Shells in Semiconductor Nanocrystals. *Zeitschrift für Phys. Chemie* **2016**, *0* (0), 77–92.

(104) Sayevich, V.; Guhrenz, C.; Dzhagan, V. M.; Sin, M.; Werheid, M.; Cai, B.; Borchardt, L.; Widmer, J.; Zahn, D. R. T.; Brunner, E.; Lesnyak, V.; Gaponik, N.; Eychmüller, A. Hybrid N -Butylamine-Based Ligands for Switching the Colloidal Solubility and Regimentation of Inorganic-Capped Nanocrystals. *ACS Nano* **2017**, *11* (2), 1559–1571.

(105) Mews, A.; Eychmüller, A. Quantum Wells within Quantum Dots, a CdS/HgS Nanoheterostructure with Global and Local Confinement. *Berichte der Bunsengesellschaft für Phys. Chemie* **1998**, *102* (10), 1343–1357.

(106) Eychmüller, A.; Mews, A.; Weller, H. A Quantum Dot Quantum Well: CdS/HgS/CdS. *Chem. Phys. Lett.* **1993**, *208* (1–2), 59–62.

(107) Pietryga, J. M.; Park, Y.-S.; Lim, J.; Fidler, A. F.; Bae, W. K.; Brovelli, S.; Klimov, V. I. Spectroscopic and Device Aspects of Nanocrystal Quantum Dots. *Chem. Rev.* **2016**, *116* (18), 10513–10622.

(108) Ivanov, S. A.; Nanda, J.; Piryatinski, A.; Achermann, M.; Balet, L. P.; Bezel, I. V; Anikeeva, P. O.; Tretiak, S.; Klimov, V. I. Light Amplification Using Inverted Core/Shell Nanocrystals: Towards Lasing in the Single-Exciton Regime. *J. Phys. Chem. B* **2004**, *108* (30), 10625–10630.

(109) Piryatinski, A.; Ivanov, S. A.; Tretiak, S.; Klimov, V. I. Effect of Quantum and Dielectric Confinement on the Exciton-Exciton Interaction Energy in Type II Core/shell Semiconductor Nanocrystals. *Nano Lett.* **2007**, *7* (1), 108–115.

(110) Wei, S.-H.; Zunger, A. Calculated Natural Band Offsets of All II–VI and III–V Semiconductors: Chemical Trends and the Role of Cation D Orbitals. *http://oasc12039.247realmedia.com/RealMedia/ads/click_lx.ads/www.aip.org/pt/adcenter/pdfcover_test/L-37/617560570/x01/AIP-PT/APL_ArticleDL_032917/FYI_HouseBanner_1640x440_v1.jpg/434f71374e315a556e61414141774c75?x* **1998**.

(111) Smith, A. M.; Mohs, A. M.; Nie, S. Tuning the Optical and Electronic Properties of Colloidal Nanocrystals by Lattice Strain. *Nat. Nanotechnol.* **2009**, *4* (1), 56–63.

(112) Zhang, J.; Tang, Y.; Lee, K.; Ouyang, M. Nonepitaxial Growth of Hybrid Core-Shell Nanostructures with Large Lattice Mismatches. *Science* **2010**, *327* (5973), 1634–1638.

(113) Lee, J.; Shevchenko, E. V; Talapin, D. V. Au−PbS Core−Shell Nanocrystals: Plasmonic Absorption Enhancement and Electrical Doping via Intra-Particle Charge Transfer. *J. Am. Chem. Soc.* **2008**, *130* (30), 9673–9675.

(114) Lambright, S.; Butaeva, E.; Razgoniaeva, N.; Hopkins, T.; Smith, B.; Perera, D.; Corbin, J.; Khon, E.; Thomas, R.; Moroz, P.; Mereshchenko, A.; Tarnovsky, A.; Zamkov, M. Enhanced Lifetime of Excitons in Nonepitaxial Au/CdS Core/shell Nanocrystals. *ACS Nano* **2014**, *8* (1), 352–361.

(115) Kahane, S. V.; Sudarsan, V.; Mahamuni, S. Anomalous Photoluminescence Enhancement due to Hot Electron Transfer in Core–shell Au–CdS Nanocrystals. *J. Lumin.* **2017**, *181*, 91–95.

(116) Kumar, A. P.; Huy, B. T.; Kumar, B. P.; Kim, J. H.; Dao, V.-D.; Choi, H.-S.; Lee, Y.-I. Novel Dithiols as Capping Ligands for CdSe Quantum Dots: Optical Properties and Solar Cell Applications. *J. Mater. Chem. C* **2015**, *3* (9), 1957–1964.

(117) Rogach, A. L.; Franzl, T.; Klar, T. A.; Feldmann, J.; Gaponik, N.; Lesnyak, V.; Shavel, A.; Eychmu, A.; Rakovich, Y. P.; Donegan, J. F.; Ludwig-maximilians-uni, V. Aqueous Synthesis of Thiol-Capped CdTe Nanocrystals : State-of-the-Art. **2007**, 14628–14637.

(118) Sander F. Wuister, *; Ingmar Swart; Floris van Driel; Stephen G. Hickey, and; Donegá, C. de M. Highly Luminescent Water-Soluble CdTe Quantum Dots. **2003**.

(119) Poles, E.; Selmarten, D. C.; Mićić, O. I.; Nozik, A. J. Anti-Stokes Photoluminescence in Colloidal Semiconductor Quantum Dots. **1999**, *75* (7), 971.

(120) Rakovich, Y. P.; Filonovich, S. A.; Gomes, M. J. M.; Donegan, J. F.; Talapin, D. V.; Rogach, A. L.; Eychmuller, A. Anti-Stokes Photoluminescence in II-VI Colloidal Nanocrystals. *Phys. status solidi* **2002**, *229* (1), 449–452.

(121) Sekhar, H.; Rao, D. N. Stokes and Anti-Stokes Luminescence in Heat-Treated CdS Nanopowders. *J. Phys. Chem. C* **2013**, *117* (5), 2300–2307.

(122) Ness, D.; Niehaus, J.; Tran, V.-H.; Weller, H. Sustainable Synthesis of Semiconductor Nanoparticles in a Continuous Flow Reactor. *MRS Proc.* **2012**, *1386*, mrsf11-1386-d07-02.

(123) Oberdörster, G.; Oberdörster, E.; Oberdörster, J. Nanotoxicology: An Emerging Discipline Evolving from Studies of Ultrafine Particles. *Environ. Health Perspect.* **2005**, *113* (7), 823–839.

(124) Nel, A.; Xia, T.; Mädler, L.; Li, N. Toxic Potential of Materials at the Nanolevel. *Science (80-.).* **2006**, *311*.

(125) Nel, A. E.; Mädler, L.; Velegol, D.; Xia, T.; Hoek, E. M. V.; Somasundaran, P.; Klaessig, F.; Castranova, V.; Thompson, M. Understanding Biophysicochemical Interactions at the Nano–bio Interface. *Nat. Mater.* **2009**, *8* (7), 543–557.

Acknowledgements

I would like to acknowledge all the people who participated to the development of this project during my PhD experience, proving themselves as an extremely valuable resource for me. One authentic thank you to all of them. I would like to make a brief shortlist of people whose contribution has revealed fundamental, in a way or another, for the completion of this degree.

First of all Vanni, my supervisor. He knows how this PhD has been an unconventional process, but I can guarantee it was one of the most meaningful experiences I have made during my life, surely the one I needed. He always had time to help and give counsel, feeding my curiosity inside and outside the nanotechnology field, I am quite sure there is a lot of people out there seeking a supervisor like him. I have been very lucky.

When I spent time abroad (in Germany and at Genova), things were not always so easy. In both cases, anyway, I was with people who could understand and support me. Especially my two supervisors at that times, Vladimir and Milena. Professional and sympathetic at the same time, hopefully I paid them back with the best work I was able to perform. It is worth mentioning, also, Vladimir S. and Andrea C., whose help for a very long list of things was crucial.

The girls and guys from the "Stanza Dottorandi" in our department, able to always create a comfortable and easy atmosphere in the office where we spent most of our time. Andrea M., aka "el furlan", which was my colleague from the beginning till the end, supporting each other either in the most critical moments or in the most ludicrous situations of our PhD life. Gianna Tavecchia, one of our last new-entries, but immediately recognized as pillar of the team. P. M., the true hero of this PhD thesis, and many others.

To my family, main supporter of my early career, tolerating my not-so-easy mindset and my irritable attitude when under pressure (quite always indeed). Looking backwards, I am quite sure I have won life's lottery.

Appendix A

The code developed for the modified thermodynamic model is here reported. It was written within the R® environment.

```
model<-function(Cnp=0.6E-6,Temp=483.15,C0=6.36E-3,Cs=0.2E-10,gamma=0.2) {
  # Cnp [mol/l], Temp [K], C0 [mol/l], Cs [mol/l], gamma [N/m]
  # script che calcola il raggio di equilibrio dei cristalli (fase solida) da fase liquida
  # il termine volumetrico di G viene ridotto dall'abbassamento della sovrasaturazione per la formazione
dei cristalli
  R<-8.31 # J/K/mol
  Vmol<-3.3E-5 # m3/mol
  Na<-6.022E23 # #/mol
  r<-seq(0,1E-7,1E-12)
  supE<-4*pi*r*r*gamma                    # energia superficiale
  S0<-C0/Cs     # sovrasaturazione iniziale
  dS<-(Cnp*Na*4*pi*r*r*r)/(3*Cs*Vmol)      # abbassamento della sovrasaturazione
  volE<-(4*pi*r*r*r*R*Temp)/(3*Vmol)*log(S0-dS)                  # energia volumetrica
  Gibbs<-supE-volE
  Gibbs<-Gibbs[!is.na(Gibbs)]     # rimuovo NA
  r<-head(r,length(Gibbs))     # impongo la stessa lunghezza di Gibbs a r (di fatto rimuovo i termini con
NA di prima)
  G1<-c()     # G1 e G2 sono le derivate della funzione. Le uso per trovare il flesso.
  G2<-c()
  for (i in c(1:(length(r)-1))) {
    G1[i]<-(Gibbs[i+1]-Gibbs[i])/(r[i+1]-r[i])
  }
  for (i in c(1:(length(G1)-1))) {
    G2[i]<-(G1[i+1]-G1[i])/(r[i+1]-r[i])
  }
  i<-length(G2)
  halt<-FALSE
  rfl<-0
  while (!halt & i>0) {
    if (G2[i]<0) {      # quando cambia concavità ho trovato il flesso
      halt<-TRUE
      rfl<-r[i]
    }
    i<-i-1
  }
  i<-length(Gibbs)
  halt<-FALSE
  min<-1E10
  req<-0
  Eeq<-0
  while (i>0 & !halt) {     # cerco il minimo della funzione. è più efficiente guardare G1?
    if (Gibbs[i]>min) {
      halt<-TRUE
      req<-r[i+1]
      Eeq<-Gibbs[i+1]
    }
    min<-Gibbs[i]
    i<-i-1
  }
  print(paste("r_thermodyn[m]=",req,"  E_thermodyn[J]=",Eeq))
  max<--1E10
  halt<-FALSE
  i<-1
  rcr<-0
  Ecr<-0
  while (i<length(Gibbs) & !halt) {     # cerco il massimo locale (raggio critico)
    if (Gibbs[i]<max) {
      halt<-TRUE
      rcr<-r[i-1]
```

```
      Ecr<-Gibbs[i-1]
    }
    max<-Gibbs[i]
    i<-i+1
  }
  print(paste("r_crit[m]=",rcr,"  E_crit[J]=",Ecr))
  ras<-(3*Vmol*C0/4/pi/Cnp/Na)^(1/3)
  ratio<-(ras-req)/ras
  print(paste("r_asymptote[m]=",ras,"Diff_ASY-EQU[%]=",ratio*100))
  print(paste("r_inflection[m]=",rfl))
  # setup dei parametri dei grafici
  yMin<-min(Gibbs, na.rm = TRUE)
  yMax<-max(Gibbs, na.rm = TRUE)
  if(rcr!=0 && req!=0) {
    #plot(r,Gibbs, xlim = c(0,2E-9), ylim = c(-1E-17,5E-18),xlab = "Mean Radius [nm]", ylab = "Chemical
Potential [J]", cex.lab=1)
    #abline(h=0, v=c(rcr), lty = c(1))     # aggiungo linee di riferimento a y=0, rcr, req

    plot(r,Gibbs, xlim = c(-1.3*rcr,1.2*req), ylim = c(yMin*1.1,yMax*1.5),xlab = "Mean Radius [nm]", ylab
= "Chemical Potential [J]", cex.lab=1, main="Modified Free Energy Curve")
    abline(h=0, v=c(req,rfl,rcr,ras), lty = c(1,1,5,1,5))     # aggiungo linee di riferimento a y=0, rcr,
req
    r1<-c(rcr,req)      # crea una nuova serie a cui attribuirò i labels con text()
    e1<-c(Ecr,Eeq)
    points(r1,e1)
    text(r1,e1,r1,pos = 1, cex = 0.75)
    View(data.frame(r,Gibbs))     # visualizzo la funzione Gibbs(r)
  }
  else {
    plot(r,Gibbs, ylim = c(yMin*1.1,yMax*1.5),xlab = "Mean Radius [nm]", ylab = "Chemical Potential [J]",
cex.lab=1, main="Modified Free Energy Curve")
  }
  # salvo i valori nel file log.txt
  write.table(matrix(c(date(),Cnp,Temp,C0,Cs,gamma,rcr,Ecr,req,Eeq,ras,rfl),  nrow  =  1),  row.names  =
FALSE, col.names = FALSE,file="log.txt",append = TRUE, eol="\n", sep="\t")
}
```

Appendix B

In this appendix, relevant data for the discussion is presented.

Colloidal Atomic Layer Deposition

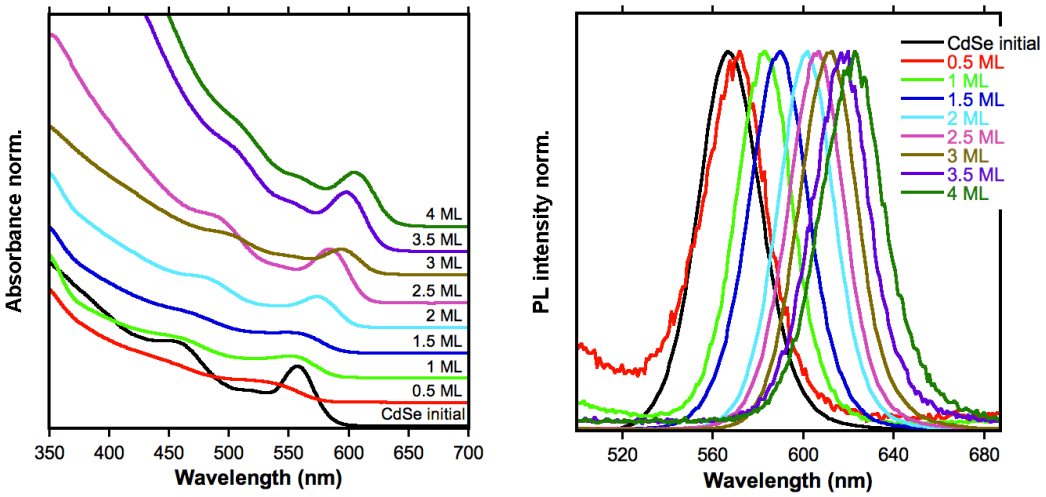

Evolution of absorption (left) and PL (right) spectra of CdSe NCs upon growing four CdS MLs resulting in CdSe/CdS4 NC heterostructure.

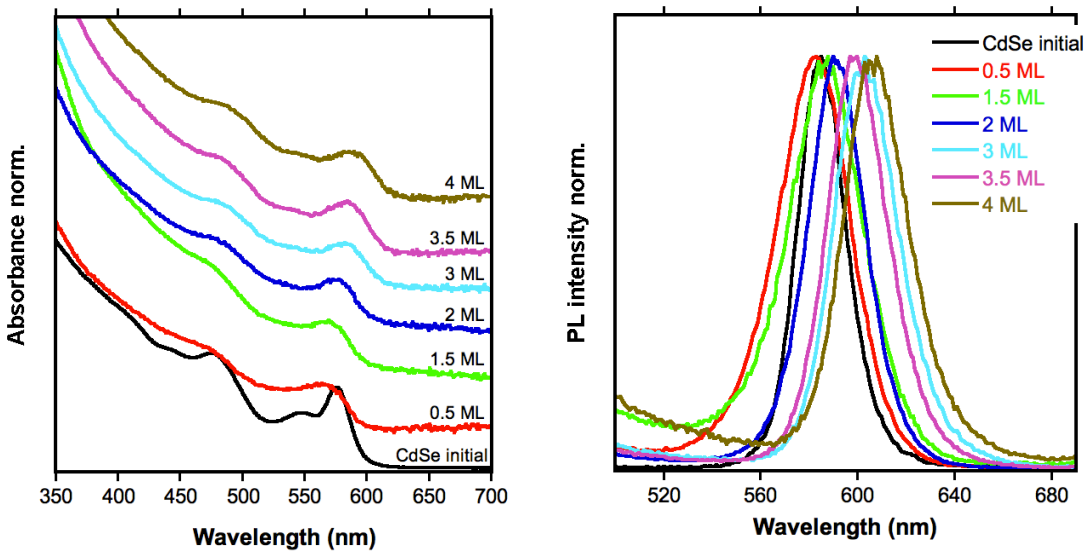

Evolution of absorption (left) and PL (right) spectra of CdSe NCs upon growing four ZnS MLs resulting in CdSe/ZnS4 NC heterostructure.

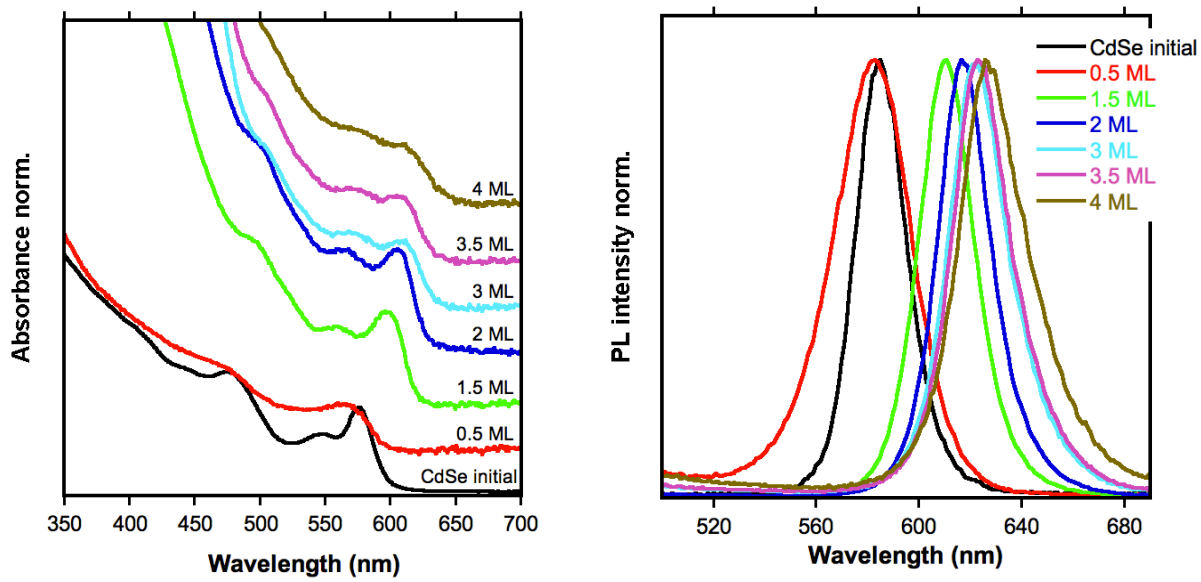

Evolution of absorption (left) and PL (right) spectra of CdSe NCs upon growing two CdS MLs, one ZnS ML and one CdS ML resulting in CdSe/CdS2/ZnS/CdS NC heterostructure.

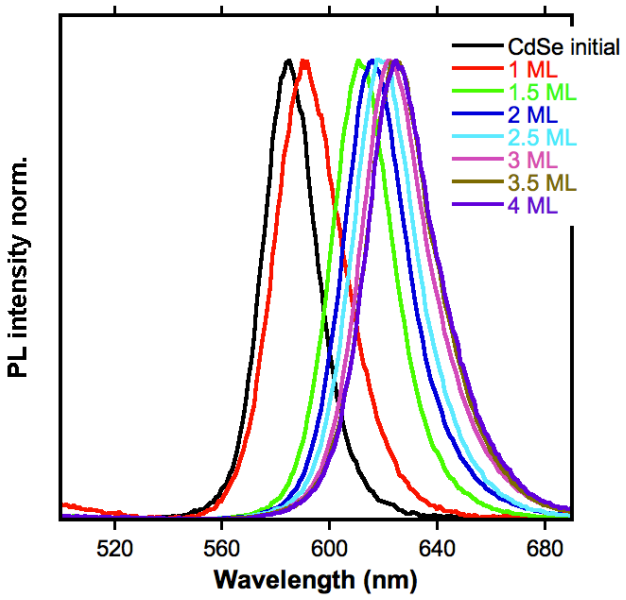

Evolution of PL spectra of CdSe NCs upon growing three CdS MLs and one ZnS ML resulting in CdSe/CdS3/ZnS NC heterostructure.

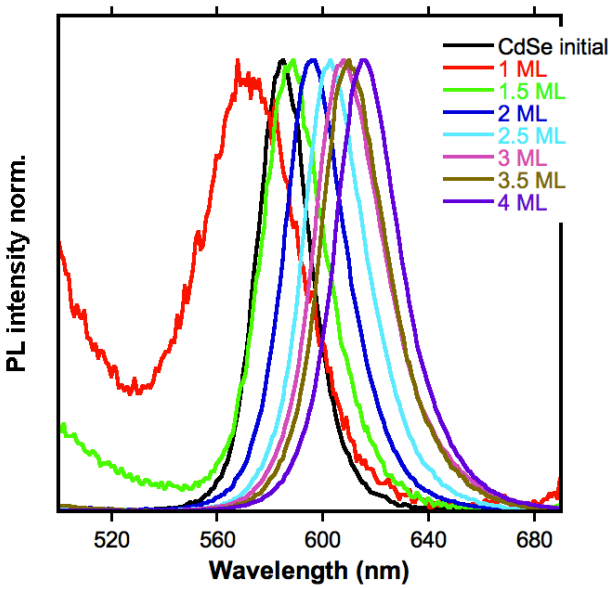

Evolution of PL spectra of CdSe NCs upon growing one ZnS ML and three CdS MLs resulting in CdSe/ZnS/CdS3 NC heterostructure.

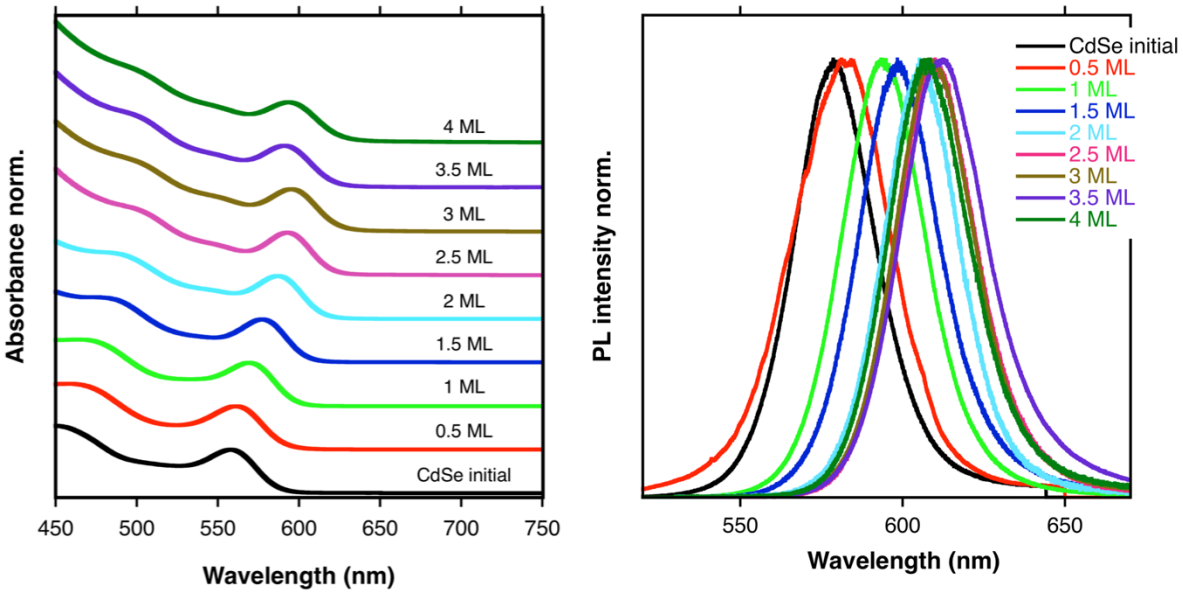

Evolution of absorption (left) and PL (right) spectra of CdSe NCs upon growing two CdS MLs and two ZnS ML resulting in CdSe/CdS2/ZnS2 NC heterostructure.

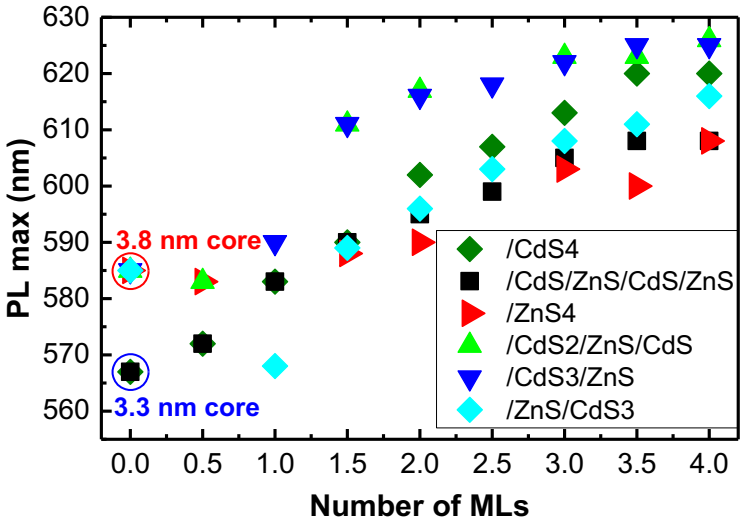

Positions of the PL maxima depending on the shell configuration for two CdSe NC core sizes, 3.3 nm and 3.8 nm.

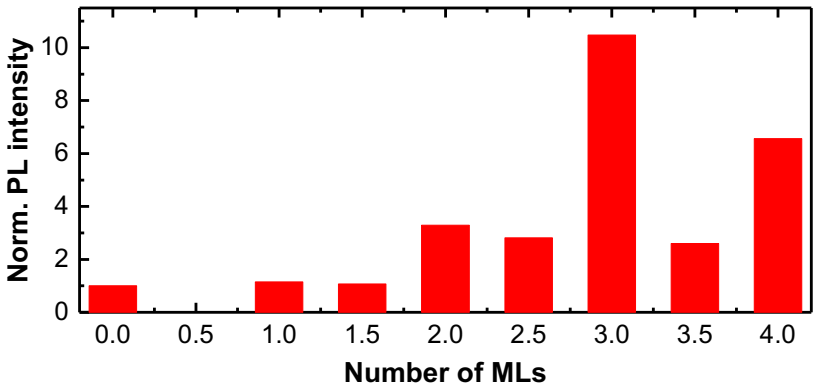

PL evolution of the sample CdSe/ZnS/CdS3 NCs as a function of the shell thickness: initial PL intensity value remained almost unaltered after ZnS layer deposition and then increased six-fold of the starting value (the numbers are normalized areas under PL curves plotted on energy scale).

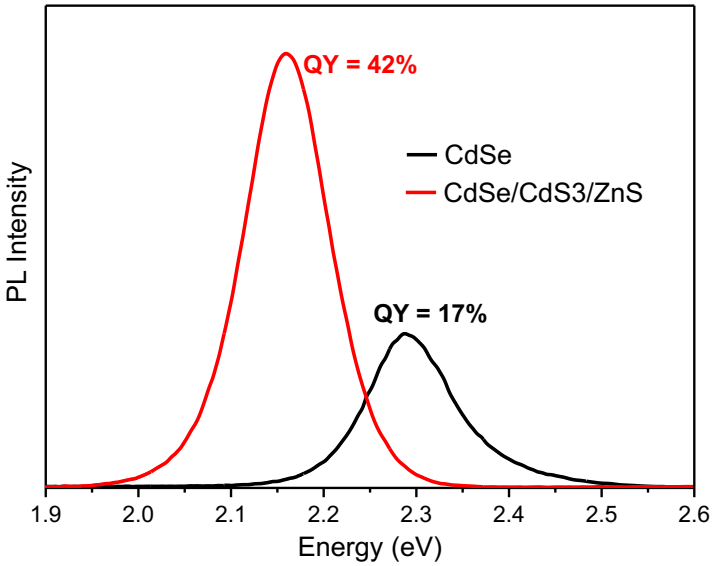

Steady-state PL emission spectra and PLQYs of initial CdSe core NCs (3.8 nm) and CdSe/CdS3/ZnS NCs, measured after storing the samples under air and ambient light for several days.

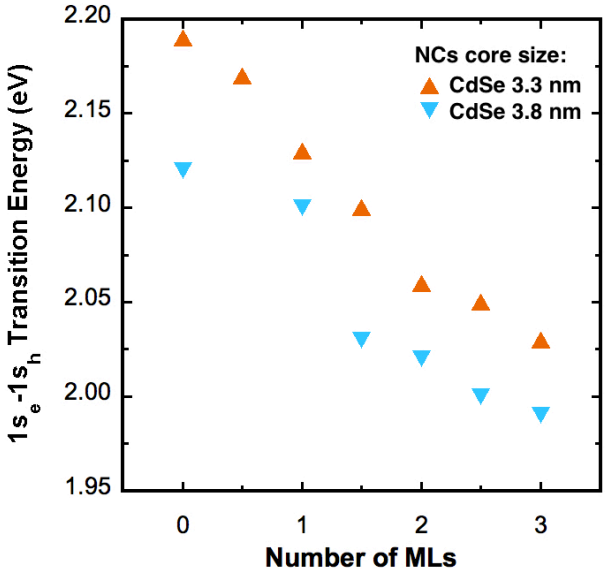

Evolution of the $1S_e$-$1S_h$ transition energy for 3.3 nm and 3.8 nm core CdSe NC size, with increasing CdS shell thickness. Growing a thicker shell reduces the transition energy. This behavior is more pronounced for the CdSe 3.3 nm core size, since the exciton confinement is more prominent compared to the 3.8 nm NC core.

Sintered Films

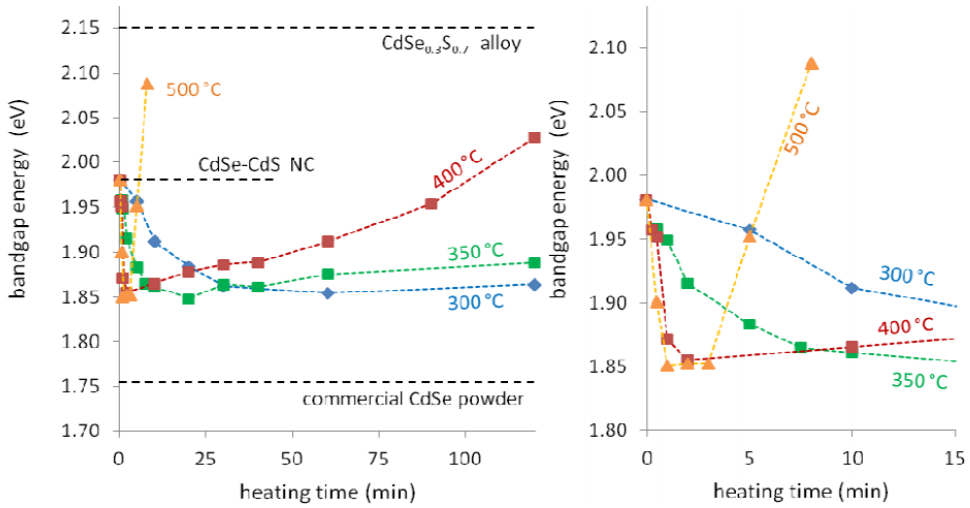

Evolution of the band gap energy (related to PL wavelength) as a function of thermal treatment time, as reported in Cozzarini [ref. 47]. Reprinted with permission. As one can observe, after a first reduction, all the observed samples present a marked increment of the apparent band-gap. Such behaviour was related to the interdiffusion of Se and S atoms, leading to the formation of the ternary structure $CdSe_{0.3}S_{0.7}$.

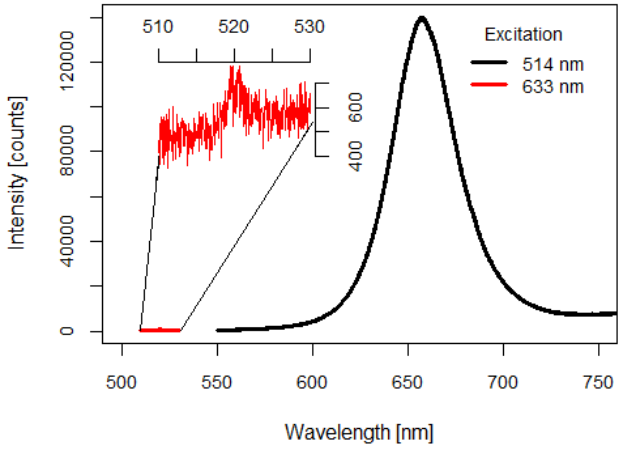

Comparison of the PL intensity for sintered films, with excitation at 514 nm (black curve) and 633 nm (red curve). As one can see, the intensity of the upconversion peak, i.e. the CdS peak, is 1000 times lower than the standard emission from core CdSe, indicating the low efficiency of the process. The laser power to stimulate the samples ware comparable even using two different emitting sources.